(ATINER)

Athens Journal of Technology & Engineering

(ATINER)

Volume 7, Issue 2, June 2020

Articles

ATHENS INSTITUTE FOR EDUCATION AND RESEARCH
A World Association of Academics and Researchers
8 Valaoritou Str., Kolonaki, 10671 Athens, Greece.
Tel.: 210-36.34.210 Fax: 210-36.34.209
Email: info@atiner.gr URL: www.atiner.gr
(ATINER) Established in 1995 (ATINER)

Mission

ATINER is an Athens-based World Association of Academics and Researchers based in Athens. ATINER is an independent and non-profit **Association** with a **Mission** to become a forum where Academics and Researchers from all over the world can meet in Athens, exchange ideas on their research and discuss future developments in their disciplines, **as well as engage with professionals from other fields**. Athens was chosen because of its long history of academic gatherings, which go back thousands of years to *Plato's Academy* and *Aristotle's Lyceum.* Both these historic places are within walking distance from ATINER's downtown offices. Since antiquity, Athens was an open city. In the words of Pericles, **Athens*"...is open to the world, we never expel a foreigner from learning or seeing".*** **(**"Pericles' Funeral Oration", in Thucydides, *The History of the Peloponnesian War).* It is ATINER's **mission** to revive the glory of Ancient Athens by inviting the World Academic Community to the city, to learn from each other in an environment of freedom and respect for other people's opinions and beliefs. After all, the free expression of one's opinion formed the basis for the development of democracy, and Athens was its cradle. As it turned out, the Golden Age of Athens was in fact, the Golden Age of the Western Civilization. *Education* and *(Re)searching* for the 'truth' are the pillars of any free (democratic) society. This is the reason why *Education* and *Research* are the two core words in ATINER's name.

The Athens Journal of Technology & Engineering
ISSN NUMBER: 2241-8237- DOI: 10.30958/ajte
Volume 7, Issue 2, June 2020
Download the entire issue (PDF)

Athens Journal of Technology & Engineering
Editorial and Reviewers' Board

President's Message

All ATINER's publications including its e-journals are open access without any costs (submission, processing, publishing, open access paid by authors, open access paid by readers etc.) and is independent of presentations at any of the many small events (conferences, symposiums, forums, colloquiums, courses, roundtable discussions) organized by ATINER throughout the year and entail significant costs of participating. The intellectual property rights of the submitting papers remain with the author. Before you submit, please make sure your paper meets the basic academic standards, which includes proper English. Some articles will be selected from the numerous papers that have been presented at the various annual international academic conferences organized by the different divisions and units of the Athens Institute for Education and Research. The plethora of papers presented every year will enable the editorial board of each journal to select the best, and in so doing produce a top-quality academic journal. In addition to papers presented, ATINER will encourage the independent submission of papers to be evaluated for publication.

The current issue is the second of the seventh volume of the *Athens Journal of Technology & Engineering (AJTE),* published by the Engineering & Architecture Division of ATINER.

Gregory T. Papanikos, President, ATINER.

Athens Institute for Education and Research

A World Association of Academics and Researchers

10th Annual International Conference on Civil Engineering
20-25 June 2020, Athens, Greece

The Civil Engineering Unit of ATINER is organizing its **10th Annual International Conference on Civil Engineering, 22-25 June 2020, Athens, Greece** sponsored by the Athens Journal of Technology & Engineering. The aim of the conference is to bring together academics and researchers of all areas of Civil Engineering other related areas. You may participate as stream leader, presenter of one paper, chair of a session or observer. Please submit a proposal using the form available (https://www.atiner.gr/2020/FORM-CIV.doc).

Academic Members Responsible for the Conference

- **Dr. Dimitrios Goulias**, Head, Civil Engineering Unit, ATINER and Associate Professor & Director of Undergraduate Studies Civil & Environmental Engineering Department, University of Maryland, USA.

Important Dates

- Abstract Submission: **11 May 2020**
- Acceptance of Abstract: 4 Weeks after Submission
- Submission of Paper: **25 May 2020**

Social and Educational Program

The Social Program Emphasizes the Educational Aspect of the Academic Meetings of Atiner.

- Greek Night Entertainment (This is the official dinner of the conference)
- Athens Sightseeing: Old and New-An Educational Urban Walk
- Social Dinner
- Mycenae Visit
- Exploration of the Aegean Islands
- Delphi Visit
- Ancient Corinth and Cape Sounion

Conference Fees

Conference fees vary from 400€ to 2000€
Details can be found at: https://www.atiner.gr/2019fees

Athens Institute for Education and Research

A World Association of Academics and Researchers

8th Annual International Conference on Industrial, Systems and Design Engineering, 22-25 June 2020, Athens, Greece

The Industrial Engineering Unit of ATINER will hold its **8th Annual International Conference on Industrial, Systems and Design Engineering, 22-25 June 2020, Athens, Greece** sponsored by the Athens Journal of Technology & Engineering.The aim of the conference is to bring together academics, researchers and professionals in areas of Industrial, Systems, Design Engineering and related subjects. You may participate as stream leader, presenter of one paper, chair of a session or observer. Please submit a proposal using the form available (https://www.atiner.gr/2020/FORM-IND.doc).

Important Dates

- Abstract Submission: **11 May 2020**
- Acceptance of Abstract: 4 Weeks after Submission
- Submission of Paper: **25 May 2020**

Academic Member Responsible for the Conference

- **Dr. Theodore Trafalis**, Director, Engineering & Architecture Division, ATINER, Professor of Industrial & Systems Engineering and Director, Optimization & Intelligent Systems Laboratory, The University of Oklahoma, USA.

Social and Educational Program

The Social Program Emphasizes the Educational Aspect of the Academic Meetings of Atiner.

- Greek Night Entertainment (This is the official dinner of the conference)
- Athens Sightseeing: Old and New-An Educational Urban Walk
- Social Dinner
- Mycenae Visit
- Exploration of the Aegean Islands
- Delphi Visit
- Ancient Corinth and Cape Sounion

More information can be found here: https://www.atiner.gr/social-program

Conference Fees

Conference fees vary from 400€ to 2000€

Details can be found at: https://www.atiner.gr/2019fees

Athens Journal of Technology & Engineering 2020, 7(2): 73-92
https://doi.org/10.30958/ajte.7-2-1

A Perspective Model for Borehole Thermal Resistance Prediction of a Vertical U-Tube in Geothermal Heat Source

By Ali H. Tarrad[*]

The present work describes a mathematical model to postulate a short cut method for the preliminary thermal design of a ground single U-tube heat exchanger. A one-dimensional steady state heat transfer mode was assumed to derive a correlation for the borehole thermal resistance to heat transfer process. The model has considered the transformation of the U-tube system into a concentric single equivalent straight tube. Its diameter was estimated from the mutual interaction between fixed volume and fixed surface area models for the treatment of U-tube and equivalent tube geometry configurations. Three Copper single U-tubes of outside diameters, 12.7 mm, 15.88 mm and 19.05 mm with tube spacing of 42 mm, 55.6 mm and 67 mm respectively were utilized to build the heat exchangers. These borehole geometry configurations were investigated as direct exchange condensers circulating R-410A at a grout thermal conductivity range of (0.73-1.9) W/m.K. The results showed that the filling thermal conductivity has a vital role in the borehole thermal performance and heat transfer rate to or from the ground source. The specific total thermal resistance of the investigated configurations was halved when the grout thermal conductivity was increased from 0.73 W/m.K to 1.9 W/m.K. The present correlation was compared with other published models in the open literature and showed an excellent agreement.

Keywords: *Borehole Thermal Resistance, Vertical U-tube Modeling, Correlation, Geothermal DX Condensers, R-410A*

Introduction

Geothermal energy source is conceived as a clean, cheap and sustainable form of other renewable energy sources. It has been implemented for a long time perhaps since the forties of the last century for heating and cooling purposes. The most important component of any geothermal heat pump system is represented by the ground heat exchanger (GHE) to reject or absorb energy from the ground. Hence, a tremendous work and effort have been spent to understand and optimize the (GHE) design and sizing to reveal the best performance in regards of amount of energy transferred and installation cost. The latter is affected by the criteria of meteorological properties, geometrical attributes of heat exchanger in the borehole, tubing characteristics and grout's thermal conductivity.

Modeling of such heat transfer problem is considered as a complex issue to be handled and represented mathematically. However, there is quite a good number

[*]Professor, University of Lorraine, France.

of research work has been accomplished in the field of modeling the (GHE) analytically, numerically and experimentally, Kavanaugh (1985), Zeng et al. (2003). The main design objectives were focused on the thermal resistance of the grout surrounding the U-tubing and heat transfer rate to or from the ground source. The analytical models for (GHE) utilize mainly a line heat source in Ingersoll et al. (1948) and Muttil and Chau (2006) and cylinder heat source theory in Ingersoll et al. (1954) and Carslaw and Jaeger (1959) to predict the heat transfer rate between the ground and the heat carrier fluid flowing in the (GHE).

Garbai and Méhes (2008) proposed a model to calculate the temperature change and the thermal resistance in vertical ground heat exchangers with single U-tube installation. They predicted the amount of extractable heat from the U-tube as a function of fluid mass flow rate passing through the ground tubing. Hafiz et al. (2017) have rated numerically an existing (60) kW heat pump system in Finland with a ground source of (250) m borehole heat exchanger depth. They estimated an optimal length for the heat capacity of the heat pump to enhance the performance of the system. A transient thermal performance of a vertical double U-tube borehole heat exchanger was numerically studied by Zhu et al. (2019). They examined a ground heat exchanger at water velocity range of 0.1 m/s and 0.5 m/s. They concluded that the charging temperature had a more vital influence than the flow velocity on soil temperature lifting. A value of 0.3 m/s for water velocity in a borehole depth of 55 m was recommended.

Sharqawy et al. (2009) developed a 2-dimensional numerical model for the steady-state heat conduction between the U-tube and borehole configuration. They suggested a correlation for the borehole thermal resistance in the form:

$$R_f = \frac{\left(-1.49\,\frac{S_p}{D_B} + 0.656\,\ln\left(\frac{D_B}{d_o}\right) + 0.436\right)}{2\,\pi\,k_g} \qquad (1)$$

They took into account the tube spacing inside the borehole in the correlation formulation, it was claimed that their correlation predicted the thermal resistance better than other available formulas.

The equivalent diameter technique has been implemented by a number of investigators to represent the U-tube heat exchanger for mathematical and geometrical treatment. The equivalent diameter of U-tube can be presented in the form of:

$$d_e = \beta d_o \qquad (2)$$

Where (β) is a constant greater than 1. Bose et al. (1985) presented the grout thermal resistance in the form:

$$R_{f=} \frac{ln\left(\frac{D_B}{\sqrt{n}\,d_o}\right)}{2\,\pi\,k_g} \qquad (3.a)$$

In which the equivalent diameter corresponds to:

$$d_e = \sqrt{n}\, d_o \quad (3.b)$$

Where (n) is equal to 2 for a single U-tube system. The U-tube pipes were modeled as a single pipe in the center of the bore with an equivalent radius accounted for the same cross sectional area of heat exchange. The heat conduction between the thin film, filling material and ground was calculated in the radial direction. Gu and O'Neal (1998) utilized a steady-state heat transfer simulation based on the cylindrical source model. They presented the equivalent diameter in a formula that coupled the tube diameter and the leg spacing in the form:

$$R_{f=} \frac{ln\left(\frac{D_B}{d_o}\sqrt{\frac{d_o}{S_p}}\right)}{2\,\pi\,k_g} \quad (4.a)$$

Rearranging this equation reveals that the equivalent diameter was expressed as:

$$d_e = \sqrt{S_p\, d_o} \quad (4.b)$$

They postulated a range of ($\sqrt{2} - 2\sqrt{2}$) for the coefficient (β) in eq. (2) depending on the U-tube legs spacing in the range of (1-4) times the outside tube diameter. Remund (1999) presented a correlation to predict the borehole thermal resistance for the three configurations of GHE pipes, close together, average and along outer wall of the borehole. The expression for the case of average tubes condition that investigated in this work was formulated as:

$$R_f = \frac{1}{17.44\,k_g\left(\frac{D_B}{d_o}\right)^{-0.6052}} \quad (5)$$

Claesson and Dunand (1983) has derived analytically the value of (β) for two buried horizontal pipes to be $\sqrt{2}$. Thus, this value shows an effective equivalent diameter corresponds to the summation of cross sectional area of both tubes. Mei and Baxter (1986) concluded that the value of the coefficient varies from well to another for their experiments. It has a scatter between 1.0 and 1.662 with a mean value of 1.28, this was smaller than the $\sqrt{2}$ calculated by Claesson and Dunand and 1.84 by Fischer and Stickford (1983). The significant impact of the value of (β) is directly related to the contact surface area of heat exchanger and effective volume of the backfill. Both of these factors are coupled to reflect the heat transfer rate for heating and cooling purposes at the ground heat exchanger (GHE). More recently, Tarrad (2019) has established a correlation to estimate the total borehole thermal resistance. He replaced the U-tube geometry with a concentric equivalent tube having the same resistance as that of the original U-tubing in the form:

$$d_e = \frac{D_B}{\left(x+\sqrt{x^2-1}\right)} \quad (6.a)$$

In this mathematical expression:

$$x = \frac{D_B{}^2 + d_o{}^2 - S_p{}^2}{2\, D_B\, d_o} \tag{6.b}$$

Hence, the thermal resistance of the grout was represented as:

$$R_f = \frac{\ln\left(\frac{D_B}{d_e}\right)}{2\,\pi\, k_g} \tag{7}$$

Present Model

Equivalent Diameter

The model is based on the idea of substitution of the U tubing by a single tube having a close operation conditions as possible to the original U-tube as shown in Figure 1.

Figure 1a. *Ground U-tubing* **Figure 1b.** *Single Tube Heat Exchanger*

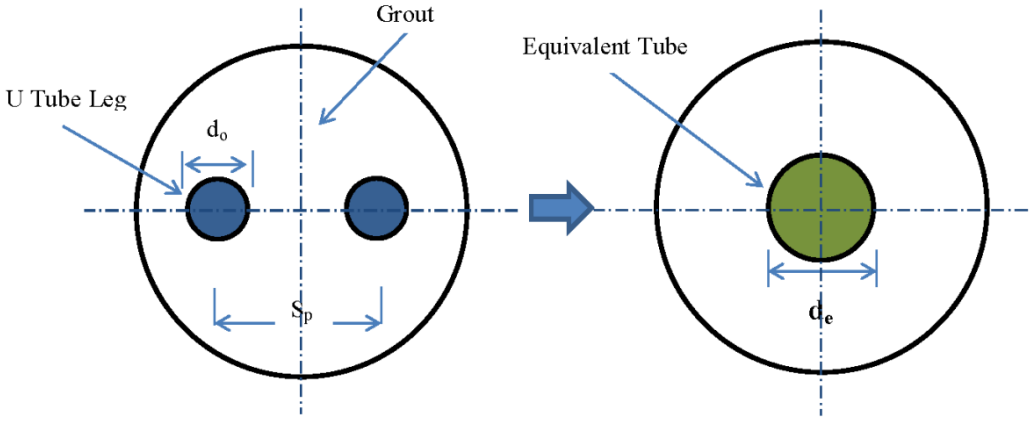

The equivalent diameter of the single tube is a complicated matter especially when dealing with physical presentation of contact surface area, volume of the filling, and conductance of different factors of heat transfer domains of the borehole geometry. This dialogue leads to the interpretation presented in this work; hence, the equivalent diameter of the U tubing is sought to provide a sort of compromise for both conditions.

The volume of the backfill in the borehole has its effect on the heat transfer rate during the transient unsteady state conditions. Gabrai and Méhes (2008) concluded that the operation of the ground U-tube heat exchanger approaches a steady state conditions after one year of its operation. If the U-tubing has similar diameters for both legs and assuming a constant volume of the grout for both geometries of U-tube and equivalent one; then:

$$\frac{\pi}{4}\left(D_B{}^2 - 2\,d_o{}^2\right) L = \frac{\pi}{4}\left(D_B{}^2 - d_e{}^2\right) L \tag{8.a}$$

This equation yields:

$$d_e = \sqrt{2}\, d_o \tag{8.b}$$

This result is similar to that of Bose et al. (1985) and Claesson and Dunand (1983) as illustrated in eq. (3).

The mathematical presentation should be as close as possible to the original geometrical configuration of the borehole. The surface area of the U-tube, tube wall and filling thermal resistances control the heat transfer process for fixed borehole diameter under steady state conditions. When the contact surface area is considered constant for both geometries, then we have the following relation:

$$2\,\pi\, d_o\, L = \pi\, d_e\, L \tag{9.a}$$

Hence

$$d_e = 2\, d_o \tag{9.b}$$

The value of (β) in eq. (2) becomes 2 and this is within the range of the coefficient postulated by Gu and O'Neal (1998) in eq. (4). Now let us consider the mean value of eqs. (8.b) and (9.b) which reveals the value of (d_e) of the equivalent diameter for the suggested geometry in the form:

$$d_e = \frac{\sqrt{2}\, d_o + 2\, d_o}{2} \approx \sqrt{3}\, d_o \tag{10}$$

Similarly, for the case when the U-tube composes of different legs sizes which are the usual geometry considered for condensers and evaporator. The vapor phase passes through a leg of bigger diameter than that of the liquid phase for hydrodynamic reasons. The following relation still holds in the form of:

$$d_e = \frac{\sqrt{d_1{}^2 + d_2{}^2} + (d_1 + d_2)}{2} \tag{11}$$

In eq. (11), the equivalent diameter of the U-tube shows the same expression as that of eq. (10) when the U-tube composes of the similar tube diameter for both legs. The heat transfer rate to or from the ground source through the heat exchanger may be mathematically presented as:

$$\dot{Q}_{U-tube} = U_{U-tube}\; A_{U-tube}\, \Delta T_m = \frac{P_{U-tube}\; \Delta T_m}{\sum R_{U-tube}} \tag{12.a}$$

$$\dot{Q}_e = U_e\; A_e\, \Delta T_m = \frac{P_{e.}\, \Delta T_m}{\sum R_{e.}} \tag{12.b}$$

Where

$$\sum R_{U-tube} = R_{conv} + R_{cond,p} + R_{grout} + R_{ground} \quad (13.a)$$

$$\sum R_{s} = R_{conv} + R_{cond,p} + R_{s,grout} + R_{ground} \quad (13.b)$$

The mean temperature difference (ΔT_m) is defined as:

$$\Delta T_m = T_{fluid,m} - T_{ground} \quad (13.c)$$

and

$$T_{fluid,m} = \frac{T_{fluid,in} + T_{fluid,out}}{2} \quad (13.d)$$

The present model expression will minimize the effect of transformation of the U-tube to a single equivalent one on the contact surface area for the (GHE). The mean value will be used for the present work as an equivalent diameter to predict the single tube transformed geometry shown in Figure 1b. Claesson and Dunand (1983) concluded that the value of the coefficient (β) must be (< 2). Whereas, Gu and O'Neal (1998) in their analytical work showed higher values as high as 2.8.

The present work stated different equivalent diameter expression than those of Bose et al. (1985) and Gu and O'Neal (1998). The latter predicts similar grout thermal resistance to that of Bose et al. (1985) when the tube spacing is selected as (2 d_o). Further the Gu and O'Neal predicts the same grout thermal resistance as that of the present work when the tube spacing is selected as (3 d_o). The tube spacing lies in the range of recommended bending radius $r_{bend} = (2 - 3)\, d_o$ for the purpose of fabrication of the copper tubes, Copper Development Association Inc. (2019). In other words, the effect of tube spacing on the equivalent diameter has been dropped out by selecting a proper geometrical configuration. This criterion for geometry layout is suitable for heat pumps that utilize the (DX) ground heat exchangers since it simplifies the fabrication of the U-tube. Further, for condensers or evaporators, which operate under isothermal process conditions, the mutual effect of heat conduction between the legs of U-tube through the shunt approaches zero. This criterion provides a flexibility to control the borehole geometrical configuration to minimize the influence of U-tube spacing on the grout thermal resistance.

The value of (β) in this work corresponds to 1.732 as shown in eq. (10). This value is consistent with the condition stated in eq. (2), in which (β) is greater than 1. It is satisfies the condition that revealed by Gu and O'Neal (1998), a value of (1.4-2.8) was assigned for (β). It is also fulfill the stated condition by Claesson and Dunand (1983) who have concluded that the value of the coefficient (β) must be (< 2). Further, the present value of the coefficient (β) is close to the experimental value of Mei and Baxter (1986); it has a scatter between 1.0 and 1.662.

Pipe Thermal Resistance

The thermal resistance of the pipe composes of convection inside the tube produced by the refrigerant flowing inside the ground heat exchanger and U-tubing wall resistance due to conduction. The pipe thermal resistance of the U-tube is replaced by a conductance layer at the tube wall with the same significant impact as the original system. Hence, the equivalent tube will act as a lumped body, which possesses those resistances and exposed to the conditions of the grout or filling resistance presented in Figure 1b. For the tube resistance (R_p), the general form of resistance analogy to the electric circuit in series defined as follows:

$$R_p = \frac{1}{\pi\, d_i\, h} + \frac{\ln\left(\frac{d_o}{d_i}\right)}{2\,\pi\, k_p} \tag{14}$$

The pipe thermal resistance will be implemented for the equivalent geometry for the estimation of total thermal resistance of the borehole geometry. However, this resistance has no significant influence for the case where there is evaporation or condensation in a DX buried heat exchanger for heating and cooling modes in winter and summer respectively. The evaporation and condensation heat transfer coefficient are so high when compared with that of the brines used for the indirect geothermal systems. The thermal conductivity of ground tubing is also high, copper tube is usually used for direct geothermal heat exchangers with about 400 W/m. °C. Hence, this resistance has no significant impact on the heat transfer rate through the filling around the tube for both modes.

Shunt Resistance

The legs of the U-tube transfer heat in the direction of higher to lower legs temperature levels. The thermal shunt resistance (R_s) is modeled as isothermal pipe-to-pipe conduction shape factor in an infinite medium per unit length Holman (2010) as:

$$S_s = \frac{2\,\pi}{\cosh^{-1}\left\{2\left(\frac{S_p}{d_o}\right)^2 - 1\right\}} \tag{15.a}$$

$$R_s = \frac{1}{S_s\, k_g} = \frac{\cosh^{-1}\left\{2\left(\frac{S_p}{d_o}\right)^2 - 1\right\}}{2\,\pi\, k_g} \tag{15.b}$$

For condensation and evaporation processes inside the U-tube, the mean temperature difference of the fluid between both legs tends to be zero. This phenomenon is usually assigned for the thermal process where change of phase takes place such as boiling and condensation of pure fluid. It may also be assumed for the case where there is a non-azeotrop mixture or azeotrop mixture having a negligible temperature glide such as (*R-410A*) refrigerant. Hence, the heat transfer rate in the shunt zone $(\dot{Q}_S)$ between the two legs of the U-tube tends to zero too.

Filling Thermal Resistance

The single tube equivalent diameter will only be used for the calculation of thermal resistance of the filling. This resistance could be expressed from heat conduction in a composite cylindrical surface presented as:

$$R_f = \frac{\ln\left(\frac{D_B}{d_e}\right)}{2\,\pi\,k_g} \tag{16}$$

Table 1 illustrates a comparison for the grout thermal resistance expressions and magnitudes of (β) for various correlations.

Table 1. *Correlations of Grout Thermal Resistance for a Single U-tube and Values of the Coefficient (β) for Various Expressions*

Model	Correlation of R_f	β
Claesson and Dunand (1983)	$R_f = \frac{ln\left(\frac{D_B}{\sqrt{2}\,d_o}\right)}{2\,\pi\,k_g}$	$\sqrt{2}$=1.414
Bose et al. (1985)	$R_f = \frac{ln\left(\frac{D_B}{\sqrt{n}\,d_o}\right)}{2\,\pi\,k_g}$	$\sqrt{2}$=1.414 *n=2* for a single U-tube
Mei and Baxter (1986)	$R_f = \frac{ln\left(\frac{D_B}{\beta\,d_o}\right)}{2\,\pi\,k_g}$	1.0-1.662 $\beta_m = 1.28$
Gu & O'Neal (1998)	$R_f = \frac{ln\left(\frac{D_B}{d_o}\sqrt{\frac{d_o}{S_p}}\right)}{2\,\pi\,k_g}$	$d_e = \sqrt{S_p\,d_o}$ $\beta = \sqrt{2} - 2\sqrt{2}$
Fischer and Stickford (2010)	$R_f = \frac{ln\left(\frac{D_B}{\beta\,d_o}\right)}{2\,\pi\,k_g}$	1.84
Present Work	$R_f = \frac{ln\left(\frac{D_B}{\beta\,d_o}\right)}{2\,\pi\,k_g}$	$\sqrt{3}$=1.732

Ground Thermal Resistance

The thermal resistance of soil to heat transfer may also be considered here. Garbai and Méhes (2008) has included the effect of ground as a resistance to heat transfer from or to the U-tube fluid for a region extended to infinity. They have concluded that after one year of operation, the heat transfer process through the ground heat exchanger can be defined as a steady state heat flow condition. Their work revealed that the ground thermal resistance reached a steady state value of

0.053 m.°C/W for a ground thermal conductivity of 2.42 W/m. °C. Hence, it was decided to implement this value at the present work. Their correlation for the grout thermal resistance was deduced for the general expression of offset cylinders from Holman (2010) as:

$$R_f = \frac{1}{S_f \; k_g} \tag{17.a}$$

$$S_f = \frac{2\,\pi\,L}{\cosh^{-1}\left\{\frac{D_B{}^2 + d_o{}^2 - S_p{}^2}{2\,D_B\,d_o}\right\}} \tag{17.b}$$

Borehole Thermal Resistance

The model presented here is a one dimensional heat transfer rate in the radial direction. The equivalent thermal resistance of the borehole of the single tubing represents the heat obstruction for the U-tube system in the form:

$$R_B = R_f + R_p \tag{18.a}$$

$$R_B = \frac{\ln\left(\frac{D_B}{d_e}\right)}{2\,\pi\,k_g} + \frac{1}{\pi\,d_i\,h} + \frac{\ln\left(\frac{d_o}{d_i}\right)}{2\,\pi\,k_p} \tag{18.b}$$

Total Thermal Resistance

The tubing of the ground heat exchanger is subjected to a total thermal resistance to heat transfer defined as:

$$R_t = R_f + R_p + R_{ground} \tag{19.a}$$

$$R_t = \frac{\ln\left(\frac{D_B}{d_e}\right)}{2\,\pi\,k_g} + \frac{1}{\pi\,d_i\,h} + \frac{\ln\left(\frac{d_o}{d_i}\right)}{2\,\pi\,k_p} + +R_{ground} \tag{19.b}$$

The ground thermal resistance is presented as that of the soil surrounding the borehole resistance, which is a time dependent measure, Garbai and Méhes (2008).

Case Study

The objective is to provide a simple tool for the prediction of heat transfer rate rejected or absorbed by a ground single U-tube heat exchanger to perform heating or cooling demands. For the case where a DX geothermal heat pump system, the ground heat exchanger works as an evaporator or condenser for heating and cooling purposes respectively. For such cases, the following condition could be considered:

1. During the condensation or evaporation processes, the change of phase takes place in an isothermal process for pure fluids and mixtures having negligible temperature glide.
2. Copper tubing is usually implemented for such purpose that has a high thermal conductivity to ensure easy way to heat flow through the tube wall.
3. One dimensional heat flow in the radial direction where a homogenous conditions present outside the U-tube.
4. The single equivalent tube possesses the thermal resistances as those of the U-tube for the convection of fluid flow and conduction of the tube wall.
5. Negligible influence of surface temperature fluctuations on the ground temperature.
6. Negligible thermal contact resistance between U-tube wall to grout and grout filling wall to the soil representing the constant temperature source or sink.

Condensation Heat Transfer Coefficient

Xiangchao et al. (2010) have reported data for condensation of *R-410A/oil* mixture at mass flux density ranged between 200 to 600 kg/m^2 s and heat flux in the range of (4-19) kW/m^2. Their data showed a deterioration of condensation heat transfer coefficient with oil percent increase. The results showed that for condensation at 40 °C, the heat transfer coefficient of pure (*R-410A*) was ranged between 2.4 to 4.6 kW/m^2 °C for the test range of vapor quality between 0.2 and 0.9 and tube diameter of 5 mm. Kim and Shin (2005) reported their experimental data for condensation heat transfer coefficient in 9.52 mm outside diameter at heat flux of 11 kW/m^2, condensation temperature of 45 °C, mass flux velocity of 273 to 287 kg/m^2 s and vapor quality of (0.1 – 0.9). The data presented a range between 2 to 3 kW/m^2 °C depending on vapor quality.

Grout Thermal Conductivity

Sagia et al. (2012) presented a tabulated list of the thermal conductivity of a number of grout mixtures as deduced from Gaia Geothermal (2009).

Table 2. *Thermal Conductivity of Grout Mixtures, Gaia Geothermal (2009)*

Grouts	**Thermal Conductivity (W/m K)**
20% Bentonite	0.73
30% Bentonite	0.74
Cement Mortar	0.78
Concrete 2100 kg/m^3	1.04
30% Bentonite - 30% Quartzite	1.3
30% Bentonite - 40% Quartzite	1.47
60% Quartzite- Flowable Fill (Cement+Fly Ash+Sand)	1.85
Concrete (50% Quartz Sand)	1.9

The range of grout thermal conductivity used in the industrial sector for fabrication of (GHE) as shown in Table 2 was used for the verification purpose of the present model.

Copper Tubes

The copper tubing diameter for the ground heat exchangers are usually selected in the range of (1/4-5/8) in. nominal or standard diameter of type (L) copper standards based on ASTM B88, Copper Development Association Inc. (2019). These sizes give outside diameters of (9.5-19.05) mm and inside diameters of (8-16.9) mm and wall factor of (12.5-17.86). Small tubing diameters are preferable for the (DX) ground heat exchangers to minimize the circulating refrigerant amount in the heat pump unit. The tube-bending radius of copper tubing is usually fabricated in the range of (2-3) times the outside diameter as a rule. Higher values are also possible depending on the available resources to accomplish the fabrication, Winton Machine Company (2019).

Methodology

Typical operating conditions were selected for comparison with existing models for the assessment of the thermal resistance of the ground heat exchanger (GHE). The following conditions were considered for the verification of the present work:

1- The condensation heat transfer coefficient for *R-410A* refrigerant is constant and fixed at 3000 W/m^2 °C as a typical reference value deduced from Xiangchao et al. (2010) and Kim and Shin (2005).
2- The copper U-tube has equal tube diameters for the descending and ascending fluid carrier legs. The respective dimensions of the test geometries are presented in Table 3.

Table 3. *Dimensions of Test Geometry Configurations*

Geometry	**WF**	**d_o (mm)**	**S_p (mm)**	**D_B (mm)**	**d_o/D_B (---)**	**S_p/D_B (---)**
1	14.29	12.7	42	75	0.17	0.56
2	15.63	15.875	55.6	90	0.18	0.62
3	17.86	19.05	67	100	0.19	0.67

Results and Discussion

Grout Specific Thermal Resistance

The comparison of grout specific thermal resistance with other correlations is presented in Figure 2 for all geometry configurations. The general trend of the behavior of the grout specific thermal resistance shows that it decreases with grout thermal conductivity increase and vice versa.

Figure 2a. *Grout Specific Thermal Resistance at WF=14.29*

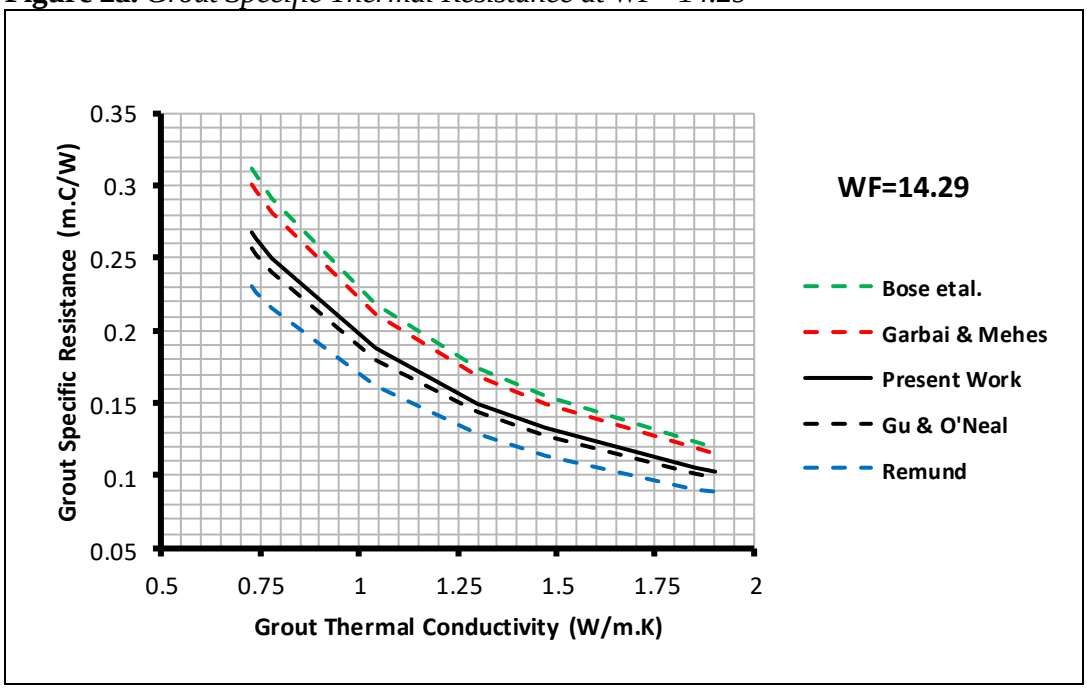

Figure 2b. *Grout Specific Thermal Resistance at WF=15.63*

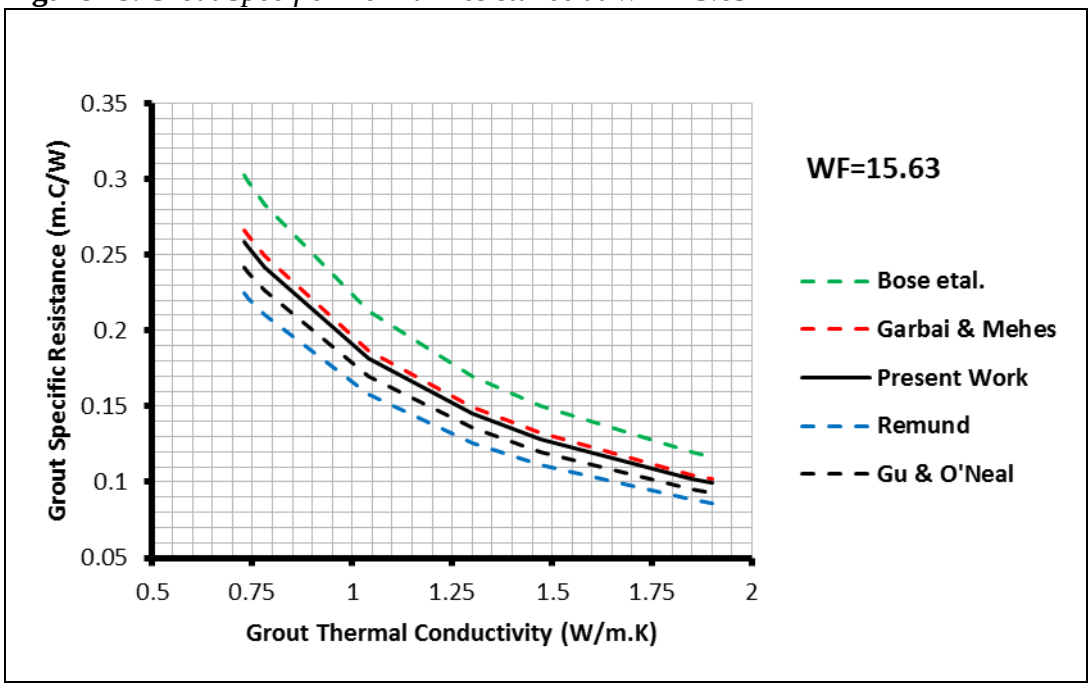

Figure 2c. *Grout Specific Thermal Resistance at WF=17.86*

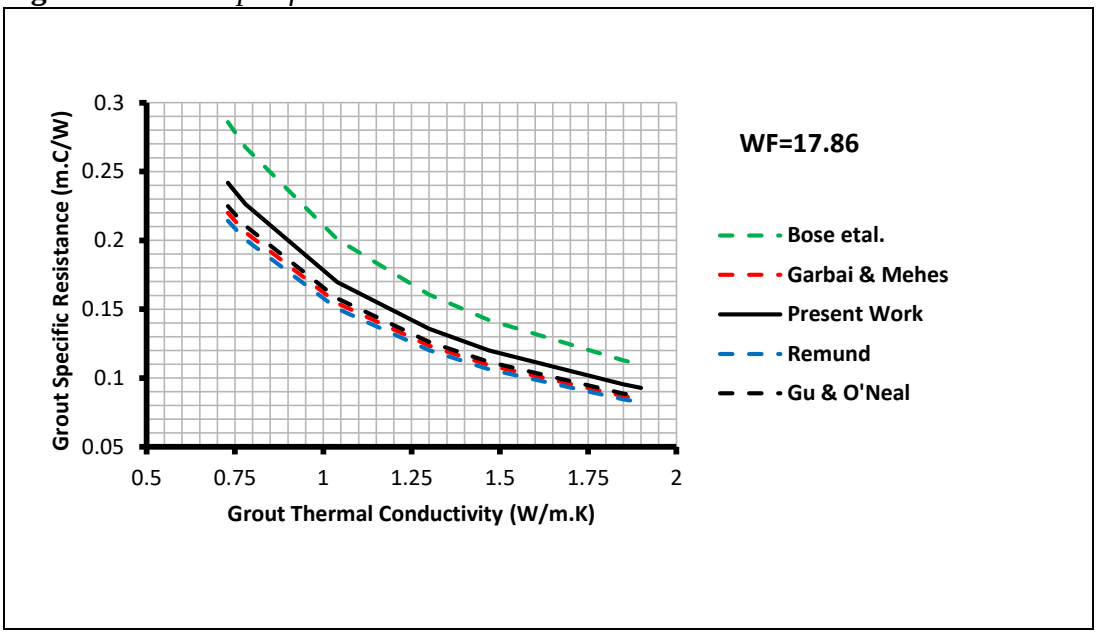

For all tested geometries, Bose et al. (1985) correlation produced the highest thermal resistance among other models whereas Remund (1999) correlation revealed the lowest one; this was regardless of the tube geometry. The present model prediction occupied the middle zone bounded by those correlations as illustrated in Figure 2.

Equations (3, 4 and 16) show that these relations share the idea of using an equivalent diameter to represent the U-tube system centered at the borehole. Table 4 shows some of the calculated values for the geometry configurations considered by those equations for geometry (1).

Table 4. *Geometrical Presentation of the Present Work and Other Investigators for WF=14.29*

Model	**d_o (mm)**	**S_p (mm)**	**d_e (mm)**	**A_e (mm^2/m)**	**V_e (mm^3/m)**	**$A_{U\text{-}tube}$ (mm^2/m)**	**$V_{U\text{-}tube}$ (mm^3/m)**	**A_{red} (%)**	**$V_{inc.}$ (%)**
Gu and O'Neal	12.7	42	23.1	72.57	419.1	79.8	265	10	58.2
Present Work	12.7	42	22	69.12	380.1	79.8	265	15.5	43.4
Bose et al.	12.7	42	18.96	56.42	282.34	79.8	265	41.4	0

The numerical values illustrate that the equivalent diameter predicted by Bose et al. (1985) was the lowest among other relations and hence higher thermal resistance. Their model was based implicitly on the assumption of using the fixed volume per unit length which was in effect caused a loss of heat transfer area by 41.4 % compared to the present work and Gu & O'Neal (1998). The latter showed the lower area reduction percent during the transformation to the single equivalent diameter, it was about 10 % whereas the present work showed a reduction of 15.5 % for the equivalent surface area when compared to the original U-tube one.

This result emphasizes that regardless of the grout volume packed in the borehole, it will reach a steady state operation and has no significant effect on the process of heat transfer under the steady state condition. Whereas, the surface area of piping system represents the major factor which possesses the larger contribution influence on heat transfer rate through the borehole. This is since other sources of thermal resistances are time independent such as pipe, grout and ground resistance when approaches the steady state condition. The numerical values of the predicted thermal resistance of the present work for the test geometries are presented in Table 5 at grout thermal conductivity of 0.73 W/m.K.

Table 5. *Present Work Test Geometries and Predicted Thermal Resistance at Grout Thermal Conductivity of (0.73) W/m.K*

Geometry	WF	d_o (mm)	S_p (mm)	D_B (mm)	d_e (mm)	R_g (m.°C /W)	R_t (m. °C /W)
1	14.29	12.7	42	75	22	0.267	0.33
2	15.63	15.875	55.6	90	27.5	0.259	0.32
3	17.86	19.05	67	100	33	0.242	0.30

The results for different geometries are compared to those predicted by Gu and O'Neal (1998) are illustrated in Figure 3. It is clear that these correlations predicted a similar data trend for the grout thermal resistance and close to each other in their numerical magnitudes.

Figure 3. *Comparison of the Grout Specific Thermal Resistance with Gu and O'Neal Model at Various Borehole Geometry Configurations*

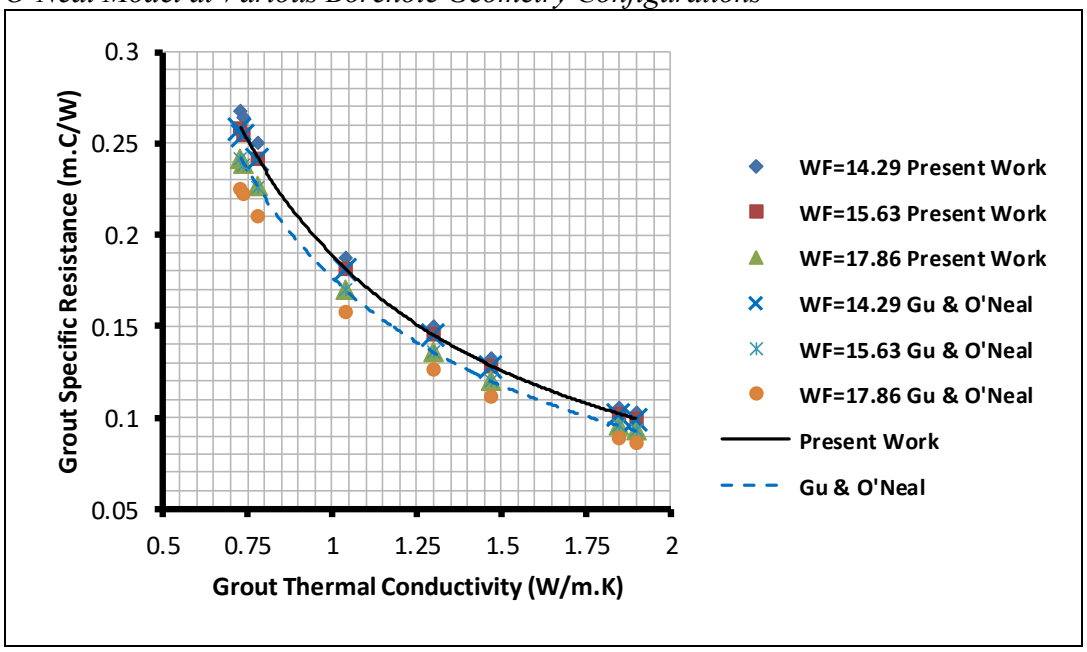

The general trend of the predicted grout thermal resistance is compared to other correlation in Figure 4.

Figure 4. *Data Trend Comparison of Grout Specific Thermal Resistance for Various Geometry Configurations with Other Investigators*

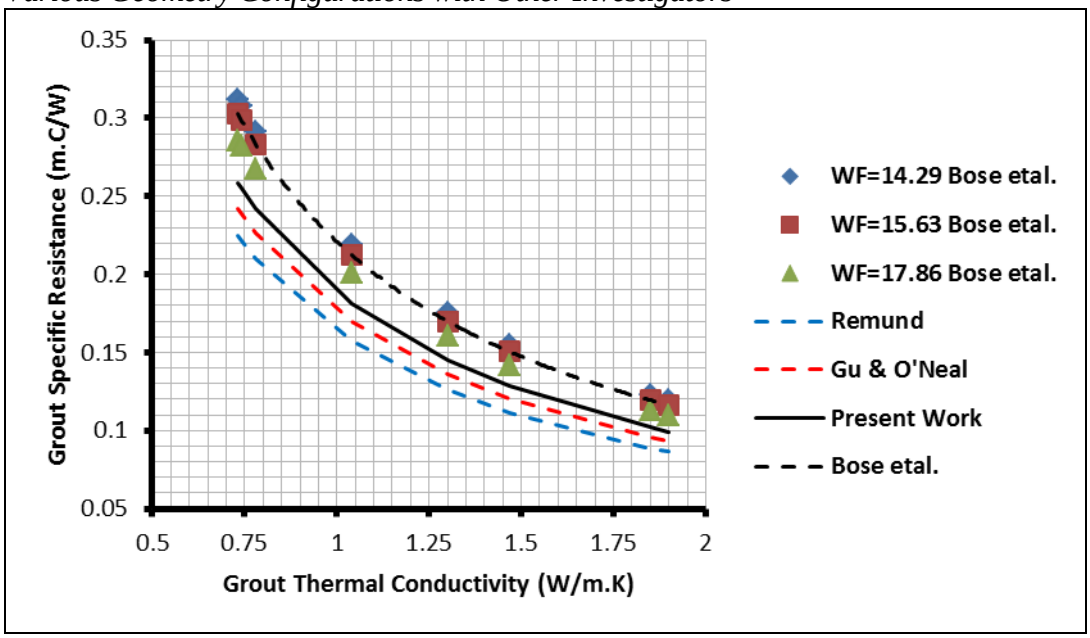

It is obvious that all models predict the same trend of data for the grout thermal resistance and showed a consistence with thermal conductivity of packing. The bigger tube size WF=17.86 showed a lower grout thermal resistance, this is due to the reduction of grout layer with increasing of the tube diameter. This phenomenon was also confirmed by other investigators.

Specific Total Thermal Resistance

The developed correlations for the grout thermal resistance by Garbai and Méhes (2008), Bose et al. (1985), Gu and O'Neal (1998), and Remund (1999) were implemented in eq. (19) for comparison with the present work, Figure 5. The models developed by Bose et al. (1985) and Garbai and Méhes (2008) showed similar values of the thermal resistance predictions and were higher than those of the present work, Gu and O'Neal (1998) and Remund (1999) models, Figure 5a and 5b. They exhibited a deviation in the range of (10.6-13.3)% and (21-28)% higher than the present model and that of Remund (1999) respectively for WF=14.29, Figure 5a. The corresponding values at WF=15.63 were (10.6-13.8)% and (20-27)% higher than those of the present work and Remund (1999) respectively, Figure 5b.

Figure 5a. *Specific Total Resistance at WF=14.29*

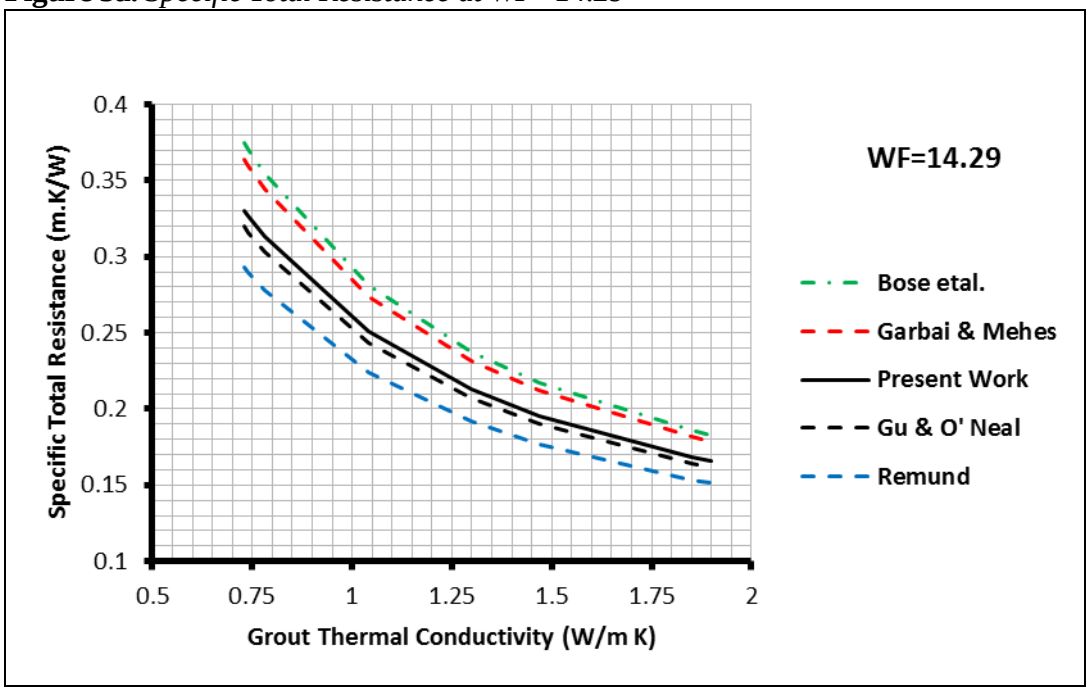

Figure 5b. *Specific Total Resistance at WF=15.63*

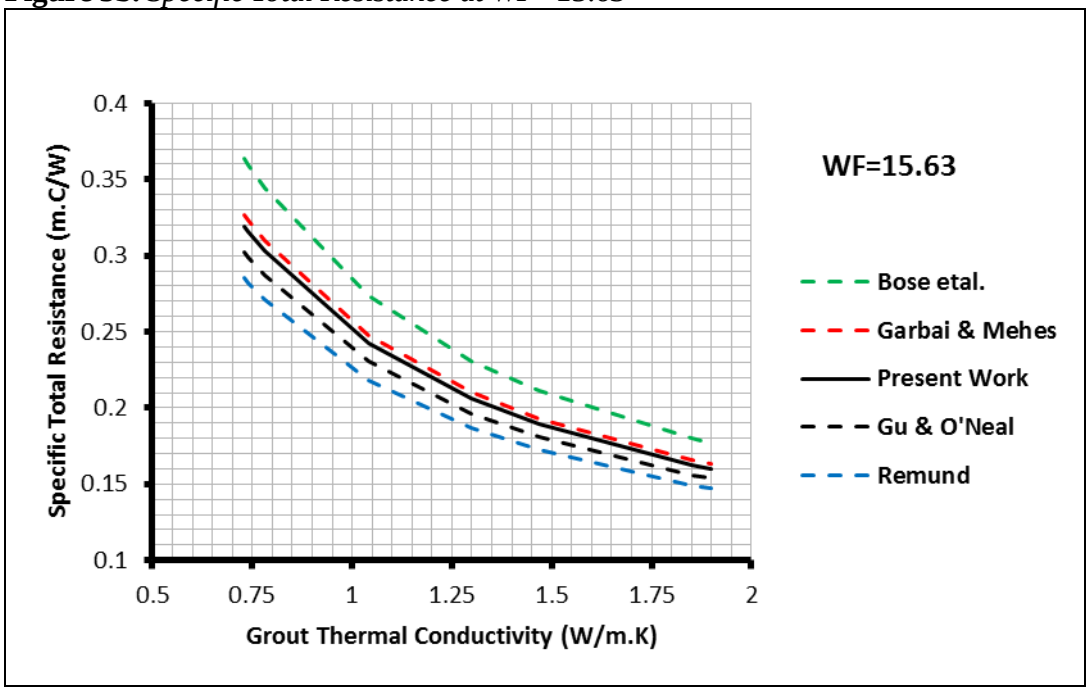

Figure 5c. *Specific Total Resistance at WF=17.86*

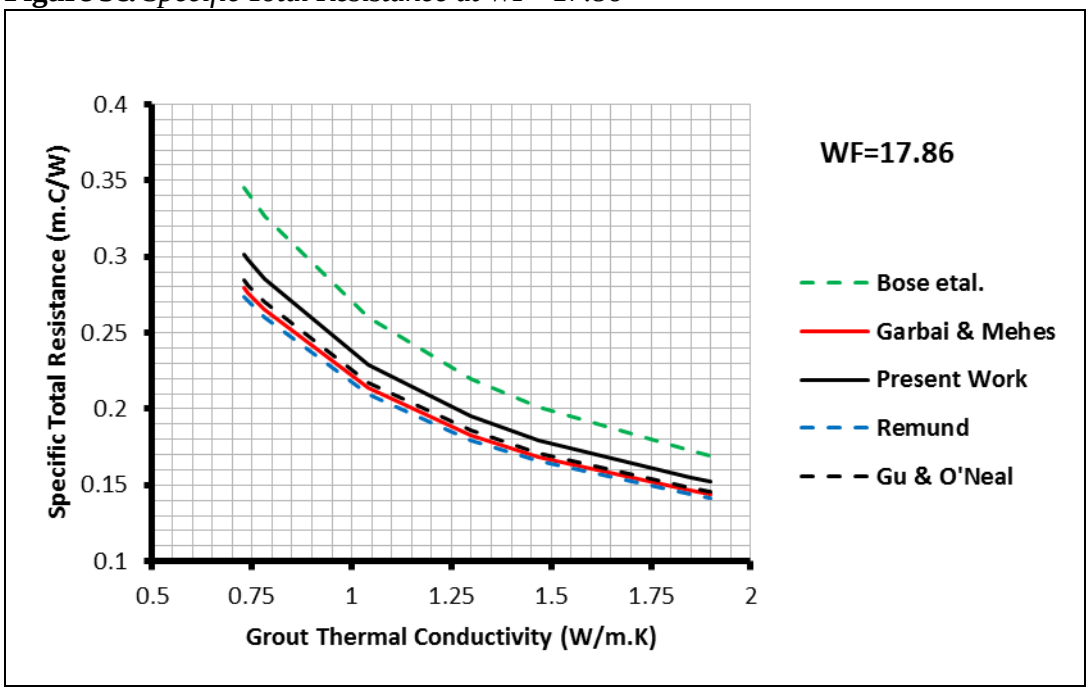

The other correlations predicted moderate values of total thermal resistances to be in the range of those predicted by Bose et al. (1985) and Remund (1999). The Gu and O'Neal (1998) correlation showed a closer thermal resistance than other correlation to the predicted values of the present work, Figure 5a and 5b. Moreover, the present work predicts exactly the same thermal resistance as that of Gu and O'Neal (1998) when the tube spacing of U-tube inside the borehole was selected as (3 d_o). Bose et al. (1985) correlation has also revealed higher values and Remund (1999) produced the lower resistance for geometry (3) but Garbai and Méhes model predicted almost similar values to those of Remund (1999).

The present work as other investigations has revealed the important role of the grout thermal conductivity on the overall thermal performance of the ground heat exchanger. The specific total thermal resistance of the heat exchanger was halved when (k_g) was increased from 0.73 W/m.K to 1.9 W/m.K for all of the examined configurations as shown in Figure 5. Hence, the heat transfer rate to or from the ground source at the highest tested (k_g) will be a double of that predicted at the lowest (k_g) when the heat exchangers operate under the same conditions.

Conclusions

A model was postulated for the estimation of thermal resistance for a single U-tube ground-coupled heat pump implemented in the geothermal energy source. The equivalent diameter derivation technique showed a consistence with other published models. The grout thermal conductivity (k_g) showed a high impact on the thermal performance of the borehole geometry. The minimum heat exchanger specific total thermal resistance (R_t) was predicted at (k_g) of 1.9 W/m.K for all of

the investigated geometry configurations. Hence, the maximum heat transfer rate to or from the ground source is expected to be at the highest tested grout thermal conductivity. Increasing of (k_g) from 0.73 W/m.K to 1.9 W/m.K has halved (R_t) of the heat exchanger. The maximum (R_t) was estimated at the smaller tube size/borehole geometry and (k_g) of 0.73 W/m.K, it fell within the range of (0.3-0.33) m.°C/W. The heat conduction through the shunt $(\dot{Q}_s)$ between the legs of the U-tube vanishes for isothermal evaporation and condensation processes. The prediction of (R_t) for the heat exchanger showed a good agreement with previous published models in the field. The outcome of this work could be used for a preliminary thermal design of ground source heat pump with acceptable confidence.

Nomenclature

Parameter	Definition
A	Surface area, m^2
d	Diameter, m
D_B	Borehole diameter, m
h	Heat transfer coefficient, W/m^2 K
k	Thermal conductivity, W/m.K
L	Tube length or borehole depth, m
P	Perimeter of tube, m
$\dot{Q}$	Heat transfer rate, W
r	Radius, m
R	Specific thermal resistance, m.°C /W
S	Shape factor of cylindrical object, m
S_p	Center to center tube spacing, m
t	Tube thickness, m
ΔT	Temperature difference, K
U	Overall heat transfer coefficient, W/m^2 K
V	Volume of tube, m^3
WF	Tube wall factor defined as (d_o/t)
x	A variable defined in eq. (6.b)

Subscription

B	Borehole
bend	Bending
e	Equivalent
f	Filling
g	Grout
i	Inside
in	Inlet port
inc.	Increase
m	Mean value

o	Outside
out	Outlet port
p	Pipe value
red	Reduction
s	Shunt
t	Total

Greek Letters

β	Coefficient defined in eq. (2)

References

Bose JE, Parker JD, McQuiston FC (1985) *Design/data manual for closed-loop ground-coupled heat pump systems*. Atlanta: American Society of Heating, Refrigeration and Air Conditioning Engineers (ASHRAE).

Carslaw HS, Jaeger JC (1959) *Conduction of heat in solids*. 2nd Edition. London: Oxford University Press.

Claesson J, Dunand A (1983) *Heat extraction from the ground by horizontal pipes - A mathematical analysis*. Stockholm: Document D1, Swedish Council for Building Research.

Copper Development Association Inc. (2019) *DX geothermal heating/cooling*. Retrieved from: https://www.copper.org/applications/plumbing/apps/dx_gt_htg_clng.html. [Accessed 16 September 2019].

Fischer RD, Stickford GH (1983) *Technical and economic feasibility of horizontal, multiple shallow-well and deep-well ground coupling*. ORNUSub/80-78001 3&06. Oak Ridge, Tennessee: Oak Ridge National Laboratory.

Gaia Geothermal (2009) *Ground Loop Design Software*. GLD.

Garbai L, Méhes S (2008) Heat capacity of vertical ground heat exchangers with single U-tube installation in the function of time. *WSEAS Transactions on Heat and Mass Transfer* 3(3): 177-186.

Gu Y, O'Neal DL (1998) Development of an equivalent diameter expression for vertical U-tubes used in ground-coupled heat pumps. *ASHRAE Transaction* 104, part (2)-4214: 1-9.

Hafiz MK, Birgitta JM, Erkki H (2017) Analysis of ground heat exchanger for a ground source heat pump: a study of an existing system to find optimal borehole length to enhance the coefficient of performance. *WSEAS Transactions on Heat and Mass Transfer* 12(Apr): 38-47.

Holman JP (2010) *Heat transfer*. 10th Edition. McGraw-Hill, 83-86.

Ingersoll LR, Zobel OJ, Ingersoll AC (1948) *Heat conduction with engineering and geological application*. New York: McGraw Hill.

Ingersoll LR, Zobel OJ, Ingersoll AC (1954) *Heat conduction with engineering, geological and other applications*. Revised Edition. Madison: University of Wisconsin Press.

Kavanaugh S (1985) *Simulation and experimental verification of vertical ground coupled heat pump systems*. PhD Thesis. USA: Oklahoma State University.

Kim M, Shin J (2005) Condensation heat transfer of R-22 and R410A in horizontal smooth and microfin tubes. *International Journal of Refrigeration* 28(6): 949-957.

Mei VC, Baxter VD (1986) Performance of a ground coupled heat pump with multiple dissimilar U-tube coils in series. *ASHRAE Transactions* 92(2A): 30-42.

Muttil N, Chau KW (2006) Neural network and genetic programming for modeling coastal algal blooms. *International Journal of Environment and Pollution* 28(3/4): 223-238.

Remund CP (1999) Borehole thermal resistance: laboratory and field studies. *ASHRAE Transactions* 105: 439-445.

Sagia Z, Stegou A, Rakopoulos C (2012) Borehole resistance and heat conduction around vertical ground heat exchangers. *The Open Chemical Engineering Journal* 6(1): 32-40.

Sharqawy MH, Mokheimer EM, Badr HM (2009) Effective pipe-to-borehole thermal resistance for vertical ground heat exchangers. *Geothermics* 38(2): 271-277.

Tarrad AH (2019) A borehole thermal resistance correlation for a single vertical DX U-tube in geothermal energy application. *American Journal of Environmental Science and Engineering* 3(4): 75-83.

Winton Machine Company (2019) *Tips for bending small diameter copper tubing with a CNC machine*. Retrieved from: https://www.wintonmachine.com/tips-for-bending-small-diameter-copper-tubing/. [Accessed 15 September 2019].

Xiangchao H, Guoliang D, Haitao H, Yu Z, Yifeng G, Bin D (2010) Condensation heat transfer characteristics of R410A–oil mixture in 5 mm and 4 mm outside diameter horizontal microfin tubes. *Experimental Thermal and Fluid Science* 34(7): 845-856.

Zeng H, Diao N, Fang Z (2003) Heat transfer analysis of boreholes in vertical ground heat exchangers. *International Journal of Heat and Mass Transfer* 46(23): 4467-4481.

Zhu L, Chen S, Yang Y, Sun Y (2019) Transient heat transfer performance of a vertical double U-tube borehole heat exchanger under different operation conditions. *Renewable Energy* 131(Feb): 494-505.

Athens Journal of Technology & Engineering 2020, 7(2): 93-116
https://doi.org/10.30958/ajte.7-2-2

Detection of Oil Slicks in the Adriatic Sea (Mediterranean) Using Satellite SAR Imagery

By Marinko Oluić[*], Mira Morović[±] & Andrei Ivanov[‡]

The goal of this paper was the detection and mapping of oil slicks in the Adriatic Sea (Mediterranean) related to bottom seeps, using a series of 34 Envisat and Radarsat-2 SAR images from the period 2003-2013. The images were analyzed using SCANEX' web-GIS GeoMixer tool. The registered oil slicks were sorted by years and by categories, indicating natural seeps with high, mid or low probability. The recurrent slicks at some places are sings of natural seepage phenomena and generally correspond to areas where crude oil may leak from seabed seeps, in accordance with tectonic and seismic information revealed.

Keywords: *Adriatic Sea, Satellite imagery, Oil slicks/seeps Detection*

Introduction

The Adriatic Sea is a semi-enclosed part of the Mediterranean, covering the area of about 138,600 km^2 (Lušić and Kos 2006). In Croatian part of the Adriatic Sea many geological and geophysical studies were carried out including exploratory drilling, which proved presence of oil and gas in some areas. The gas has been exploited in the North Adriatic Sea since the 80s of the last century.

Various remote sensing techniques were used in many areas of the world to detect natural oil seeps at the sea floor. Satellite remote sensing could be the best approach to more accurate estimate of natural oil seepage rates, and according to Kvenvolden and Cooper (2003) natural seeps account for about 47% of the crude oil entering the marine environment. It is well known that microwave sensors have the advantage for oil slick detection due to the unique sensitivity of the radar signal to the small-scale roughness (short-scale wind induced waves) of the sea surface (Topouzelis et al. 2007, Akar et al. 2011). Radar backscattering levels decrease on slicks and they appear as a dark patches with lower backscatter from the sea surface (Girard-Ardhuin et al. 2003). Therefore, systematic and global applications of satellite images can help locate natural oil seeps and improve estimates of seepage rates into the oceans (Hu et al. 2009). It is also possible to distinguish between anthropogenic oil spills, natural seepage slicks and look-alikes using semi-automatic discrimination and visual inspection of detected dark spots (Bayramov et al. 2018).

In the world seas the oil slick detection and mapping based on satellite data were often used for hydrocarbon exploration and oil seeps detection, such as in the

[*]Adviser, GeoSat Co, Croatia.
[±]Consultant, Institute of Oceanography and Fisheries, Croatia.
[‡]Researcher, Shirshov Institute of Oceanology, Russian Academy of Sciences, Russia.

Gulf of Mexico (Friedman et al. 2002), the South Caspian Sea (Zatyagalova et al. 2007, Ivanov and Zatyagalova 2008), the Black Sea (Evtushenko and Ivanov 2013), Australian shelf (O'Brein et al. 2005), Santa Barbara Channel, California (Leifer et al. 2006), Lake Baikal (Ivanov 2012) etc.

Registered oil slicks and oil spills in Middle Adriatic mostly appear from anthropogenic sources (ships) or biogenic sources like phytoplankton blooms (Morović and Ivanov 2011, Morović et al. 2014, Morović et al. 2015). However, part of these oil slicks may be related to natural seepage.

Main geo-tectonic framework of the Adriatic Sea resulted as the disintegration of the Adriatic micro-plate. It is sinking below the Eurasian tectonic plate, accompanied by frequent, though not particularly intense seismic activity. We supposed that leaking of the oil might occur through a local fracture zones in the sea floor bedrock. This would be seen as oil slicks on he sea surface and could be indication of oil deposits. In addition, the gas seeps may possibly be linked to salt structures in the Middle Adriatic.

Detection of marine seepage with Synthetic Aperture Radar (SAR) could provide the first indication of undersea petroleum systems. Performed analysis of Envisat SAR images showed that there are many small size dark surface manifestations (slicks) visible on SAR images acquired at low wind conditions.

The main goal of this investigation was detection, mapping and identification of natural oil slick/seep manifestations, and their spreading in the Middle Adriatic, based on the SAR satellite data, performed for the first time in the Croatian waters (Oluić et al. 2014).

Study Area

The study area is the Middle Adriatic, encompassing more than 17,000 km^2 (Figure 1).

Figure 1. (Left) *The Satellite Mosaic of the Mediterranean;* (Right) *The Location of Investigated Area (Black Polygon) at the Adriatic Bathymetry Map*

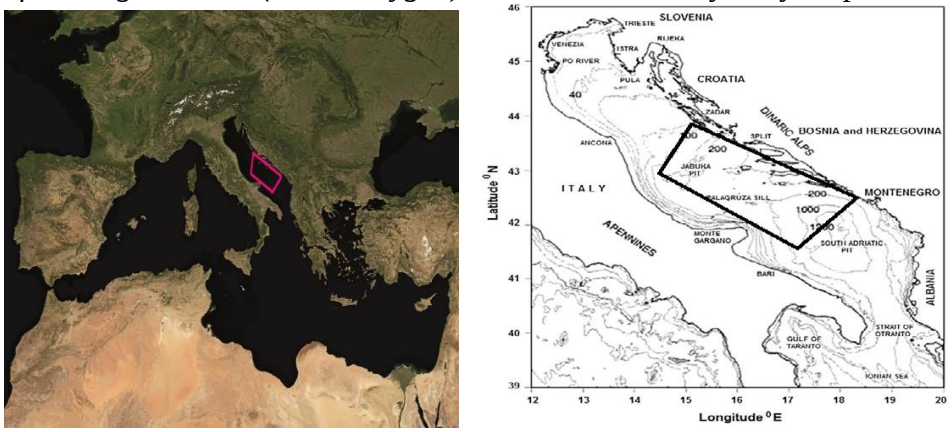

However, the investigated area was somewhat wider due to a different coverage of the satellite images, which allowed better locating of oil phenomena relative to the coast and islands.

The investigated area spreads over the Middle Adriatic covering Jabuka Trough and Palagruža Sill and extends partly to the Southern Adriatic Basin. Bathymetry over the Adriatic axis crossing the area along the marked polygon gradually deepens from the isobaths 100 m to 1,200 m depth.

Tectonic and Seismic Activity of the Adriatic Seabed and Oil Origin

Tectonics

The Adriatic Basin is detached part of the African tectonic plate, known as Adriatic micro-plate (Devoti et al. 2002, Battaglia et al. 2004). The African and Eurasian plates started to collide at Early Cenozoic and collision between these plates has continued up to the present time (Volpi 2017). The Adriatic micro-plate has been subducted beneath the Eurasian plate and is still sinking toward north and northeast at a rate of about 4 mm/year (Oluić 2015). The structure and topography of the Adriatic microplate is dominated by the collision of these two plates. The rocks in the Adriatic micro-plate have sedimented over the crystalline complex in submerged depressions. Approximate depth of crystalline basement is varying between 6 and 14 km (Brdarević and Oluić 1979).

There are several submerged basins/depressions in which sedimentary rocks have developed, composed mostly of biogenic carbonates and evaporites. The most important depression is the Middle Adriatic Depression (MAD), characterized with crystalline basement at depths of more than 9 km beneath the sea floor (Figure 2). However, the deepest formation is the so called "Primorsko-dalmatinska depression" (Littoral-Dalmatia Depression), reaching the depth of about 14 km (Brdarević and Oluić 1979).

In CAD there are several different sea floor morphologies like pockmarks, mud volcanoes and mud carbonate mounds, as a result of the mobilization of gas trough fracture systems and pathways for fluid seepage, that are mostly related to present halokinetic activity of the deep, Triassic evaporite occurrences (Geletti et al. 2008). Several emerged positive structures (horsts) of the crystalline rocks have been recognized as well, such as "Primorsko-dalmatinska elevation", in which crystalline rocks are lying at depth of about 6 km.

Figure 2. *The Structure and Morphology Map of Cristalline Rocks in the Central Adriatic*

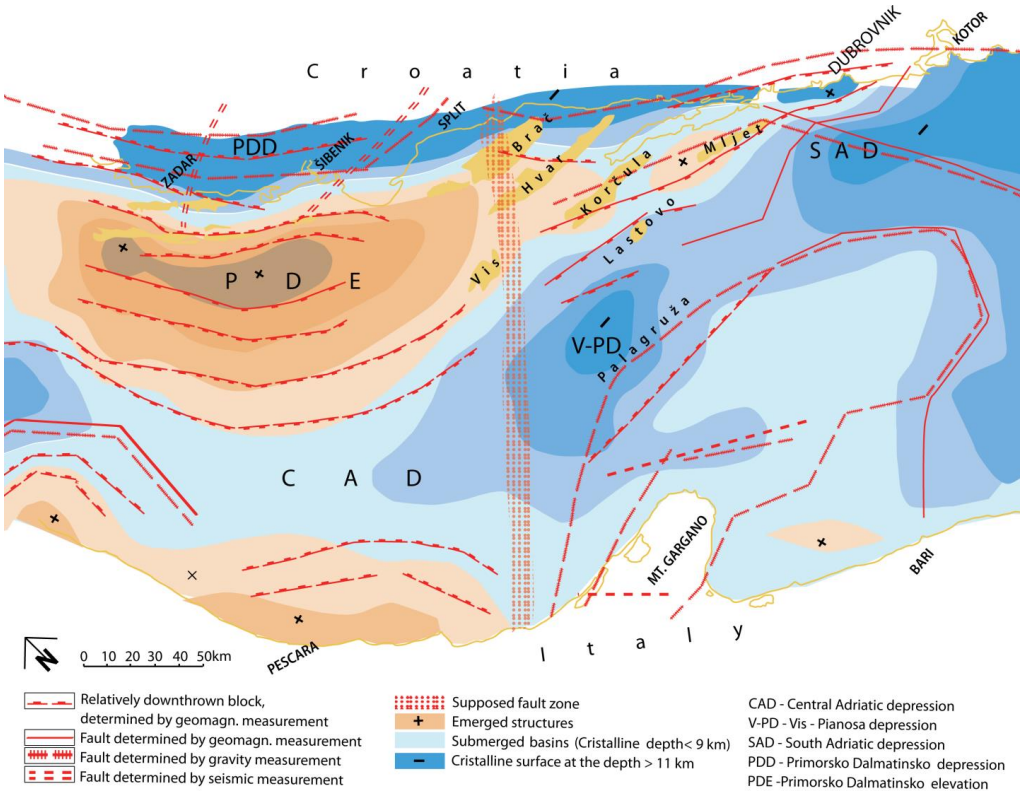

Source: Brdarević and Oluić 1979; simplified.

There is a number of active faults, which have a significant influence on position, and distribution of sedimentary rocks. Some blocks subsided along the vertical and subvertical faults for about 5 km, whereas others have been moved reversely, generally in SW-verging fault system extending along the Adriatic axis. There are also transverse tectonic structures, deformation zones of regional importance. These structures have been caused by complex tectonics, by magmatism and gravity, and also by salt tectonics (Tufekčić 2015). The salt structures have typical widths of 5-10 km and they seem generally connected to thrust faults, mainly active during the Upper Pliocene (Geletti et al. 2008). Sediment diapirs occurring on the seabed associated with continuous release of gas are well known (Hovland and Curzi 1989). The salt structures are particularly important, because they act as gas seeps in the Middle Adriatic Sea (Geletti et al. 2008). The example is Jabuka Islet, where Triassic igneous bodies are extruded by salt tectonics (Pikelj et al. 2015). Due to rapid subsidence of marine basins, which occurred particularly in the Mesozoic and Neogene, very thick sedimentary deposits have been formed in places thicker than 8 km. Permo-Triasic rocks thick about 2.5 km have sedimented on the basement, while Jurassic, Cretaceous, and Eocene sediments are more than 1 km thick (Volpi 2017). The subsidence of large Jurassic and Cretaceous blocks/basins caused the emergence of oil and gas bearing rocks, covered by very thick clastic sedimentary sequence of the upper Eocene-Oligocene age (Grandić et al. 1999) and thick series of Neogene sediments (Brkić

et al. 2013). In CAD the early Quaternary and Pliocene sediments are 1-1.5 km thick (Hovland and Curzi 1989). The CAD is elongated in a NW-SE direction with thick sedimentary rocks important for hydrocarbon accumulation, since for the formation of hydrocarbon in sedimentary basins minimum sediment thickness of 2 km is necessary (Soloviev 2002).

The Adriatic Basin has both biogenic (microbial) and deep thermogenic petroleum systems. The Upper Triassic and Lower Jurassic source rocks in the Adriatic Sea, represented mostly by carbonates, bear oil and gas deposits (Cota et al. 2015). Triassic source rocks, composing an active Triassic petroleum system, have been sedimented in the carbonate-evaporite environment along the Croatian part of the Adriatic Basin (Cota et al. 2015).

Exploration activity in the Croatian waters of Middle Adriatic was focused on the rocks of the Creataceus carbonate platform (Wrigley et al. 2014). The oil deposits have been discovered in carbonate reservoirs at depths of 4,000-5,300 m, but according to Casero and Bigi (2013) the main reservoir can be around 1,300 m deep, below sea floor. Hydrocarbon exploration of the Middle Adriatic has been carried out since 1960s through seismic surveys and drilling (Mattavelli et al. 1991). In the period of 1955 to 80s last century, more than 190 oil and gas fields throughout the Adriatic Sea have been discovered, mostly on Italian side, and a few dozens were found in Croatian waters too (Cota et al. 2015).

The first report of a gas seep in the Adriatic Sea was gas bubbling at the sea surface off Rovinj (North Adriatic), Croatia in 1940 (Conti et al. 2002). In the northern part of Middle Adriatic large actively seeping pockmarks and hydrocarbon flows were discovered at depths of about 100 m; the flows were emanating from depressions up to a few hundred meters wide and a few meters deep (Stefanon 1981).

In MAD- present seabed pockmarks were formed by gas whose migration was facilitated by a pre–existing pathways made by subsidence in the Jabuka Trough (Curzi and Veggiani 1985, Mazzetti et al. 1987). On the other hand, Hovland et al. (1997) suggested that most promising areas to look for resources are active mud volcanoes, such as in the area of Jabuka Islet, especially when oil and gas coexist in reservoir (Etiope 2014).

Seismic Activity and Oil/Gas Migration in the Investigated Area

The explored area of the Adriatic seabed is seismotectonically very active. Frequent earthquakes appear mostly between Richter magnitudes $M < 3.0$ up to $M = 4.0$, but infrequently there occur earthquakes of magnitudes $M \geq 5.0$. Earthquake hypocentral depths mostly extend down to 12 km (Volpi 2017), but sometimes down to 15-20 km (Castello et al. 2006). Distribution of recent tectonically induced earthquakes of $M \geq 3.0$ is shown on the Figure 3. Generally, the highest number of earthquake epicenters grouped in several areas: west and southwest of Vis Island and southwest of Lastovo Island (Figure 3A). Most of the earthquakes, registered in the period 1985 to 2013, occurred from 2006-2013 (Figure 3B). The earthquake data coincided with increased number of registered oil slicks appearing on the sea surface in the period of our observations. This also suggest a correlation

between oil slicks and structural features, particularly fracture zones along which pathways of fluid seepage occur, bringing oil to the sea surface.

Figure 3. (A) *Spatial Distribution of Earthquake Epicenters in the Central Adriatic Occurring in the Period 1985-2013;* (B) *Temporal Distribution of Earthquakes of Magnitudes M ≥ 3 from 2000-2013*

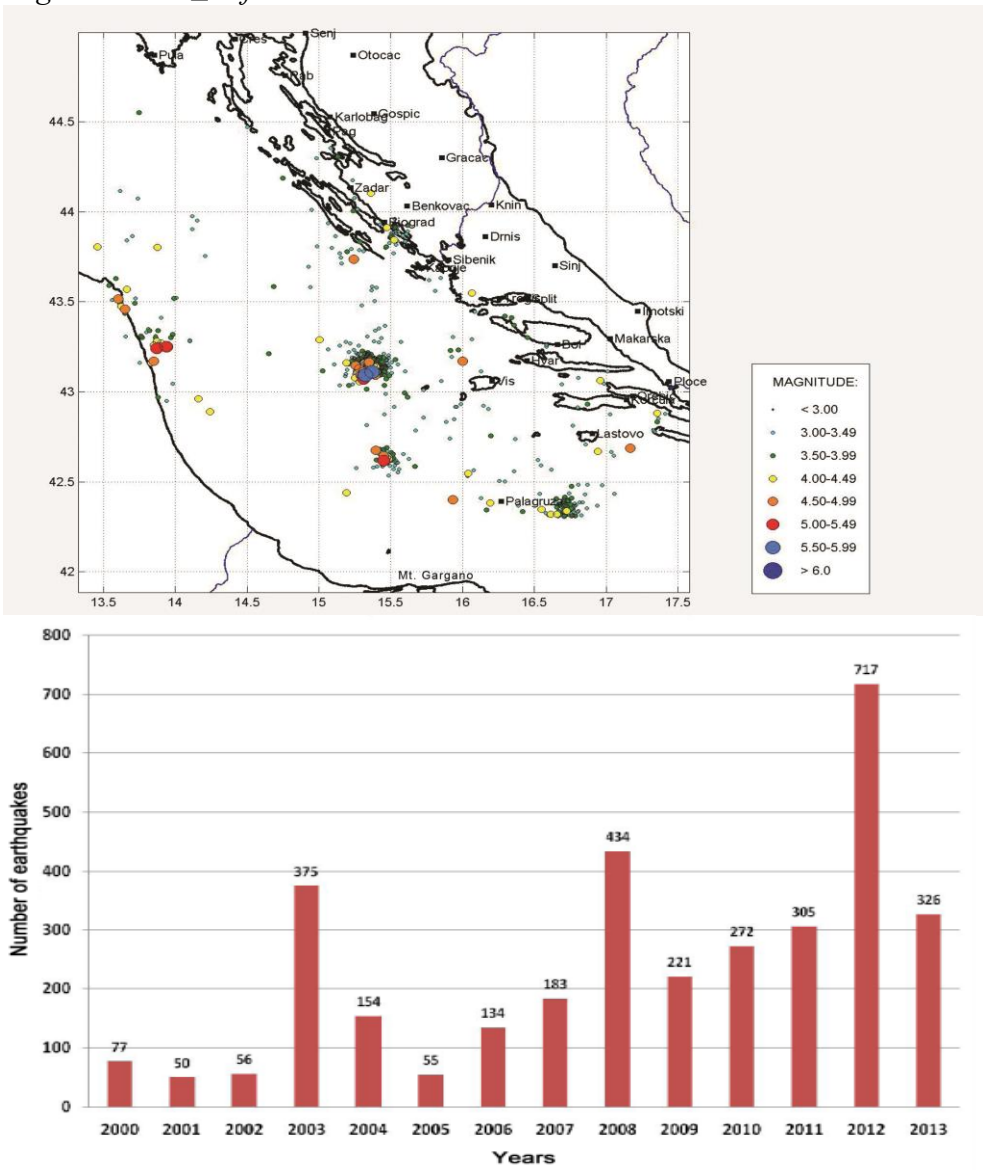

Source: Geophysical Institute "A. Mohorovičić", University of Zagreb.

Hydrothermal fluid releases, like the formation of pockmarks, may have been triggered by activefaulting and could be associated to earthquake activity (Judd and Hovland 2007). Observations suggest that pockmarks go into an active state before and during the earthquake, showing generally higher rate of gas venting from the sea floor (Dando et al. 1995). Observations have also shown enhanced gas emission immediately prior to the earthquake (Hovland et al. 2002). Pockmarks also became active by releasing gas a few hours before a major earthquake (Judd

and Hovland 2007). According to the same authors, the seeps are effective tools for determining whether or not a sedimentary basin has petroleum potential.

Seismotectonic activity can form vertical and subvertical faults. Often reverse slip occurs while fractures above petroleum reservoirs and seismic vibration can considerably increase the permeability due to desorption of gas from the rock matrix (Kouznetsov et al. 1994). In general, gas seepage results from the vertical migration of gas from accumulations in hydrocarbon reservoirs (Etiope 2014). The migration to the sea surface mostly occurs along fracture system.

If a petroleum reservoir is intersected by an active fault and the permeability in the fault zone increases after the earthquake, then there may be a rapid increase in the rate of upward gas/oil migration. In such a way, the gas bubbles and oil leak from the seabed towards the sea surface (Gurevich and Chilingarian 1993, Tary et al. 2012). Several authors have described gas seepages in the Middle Adriatic (Curzi and Vegiani 1985, Mazzetti et al. 1987, Hovland and Curzi 1989, Trincardi et al. 2004). However, bubblemarks are not permanent features, but are created intermittently by explosive eruptions and usually are connected to tectonic and earthquake activity. Methane gas accumulated in geological structures is buoyant and inclined to migrate towards the surface. After appearing on the sea surface, it evaporates, while oil remains for a while, being visible as oil slicks from the satellite SAR imagery (Etiope et al. 2014). Oil slicks have relatively short lives 6 - 48 hours (Mac Donald et al. 1993).

Material and Methods

SAR Satellite Images Used in the Investigation

Satellite SAR images have been acquired for the period 2003-2011 in the framework of an ESA project. The ESA Envisat SAR database was investigated in order to find suitable SAR images covering the Middle Adriatic. From the first analysis of Envisat SAR images (Image Mode with HH and VV polarization, at incidence angles 15-45^{o} and resolution 30 to 150 m), about 300 were selected from the ESA catalogue of which 31 images were suitable for detection of oil slicks/spills; these were selected and analyzed in details. The analyzed set also included 3 Radarsat-2 SAR scenes obtained in 2013. The acquisition times of analyzed images is shown in the Table 1.

Table 1. *The List of Processed and Analyzed SAR Images Acquired over the Middle Adriatic for the Period 2003-2013 (Radarsat Images are Marked with Asterix)*

Year	Month	Day	Hour	Minute	Year	Month	Day	Hour	Minute
2003	04	15	09	21	2008	09	11	09	18
2003	06	21	09	15	2008	09	24	09	10
2003	05	04	20	41	2008	11	20	09	18
2004	05	01	09	15	2008	11	20	09	18
2004	06	27	20	41	2009	07	23	09	18
2004	05	01	09	15	2009	11	18	09	10
2008	05	07	09	10	2009	12	07	09	12
2008	05	10	09	15	2010	08	28	09	15
2008	05	23	09	07	2010	07	05	09	12
2008	05	23	09	07	2010	07	21	09	09
2008	05	23	09	07	2010	09	07	09	01
2008	07	03	09	18	2010	09	13	09	12
2008	07	03	09	18	2010	10	02	20	33
2008	07	16	09	10	2011	06	24	09	17
2008	07	19	09	15	2013*	09	23	16	40
2008	08	04	09	12	2013*	08	30	16	40
2008	08	04	09	12	2013*	10	24	16	36

The Radarsat-2 SAR image acquired 2013-09-23 covered 150 x 150 km of marine area with spatial resolution of about 30 m (Scan SAR Narrow mode, pixel size 12.5 x 12.5 m and incidence angles 25-30^{o}). The other two Radarsat scenes were acquired in standard W1 mode, VV polarization and image size of 100 km swath width, at incidence angles 25-46^{o}, and with 25 m resolution.

Methods of Image Processing and Analysis

Oil slicks are visible on SAR images as dark patches, because these locally decrease the sea surface roughness, and in turn the radar backscatter on the sea surface. The oil slicks detection depends primarily on three key parameters that define sea-surface backscatter. These are: wind speed, polarization modes and incidence angle.

The ability of detecting the dark features increases with the increase of radar contrast between oil spill and the surrounding water, which, in turn, is a function of spill parameters, environmental conditions, and both oil release and weather conditions. Environmental factors determine spreading, drift and weathering of oil on the sea surface. Detecting the low contrast patches depends also on the speckle noise, which are present in the images. Application of different filters decreases noise level and improves the feature detection on the image. The next step in the image processing is dark spot detection, feature extraction and oil spill/slicks/look-alike identification and classification (Brekke and Solberg 2005).

The process of the oil spill identification consisted of several successive steps. The first step in the analysis of Radarsat images was to locate the oil slicks and its contours by visual inspection using distinguishing gradients, manual delineation and threshold separation. The filters were applied in order to increase contrast and reduce speckle noise. Adaptive filters based on appropriate scene and speckle

model are the most fitting filters for SAR images because they preserve structural and textural features. An established confidence guideline for oil interpretation (developed by *MDA*, Canada), has also been considered. It is based on the SAR signature in comparison to the surrounding sea state that indicates the possible presence of oil on the sea surface.

The Envisat SAR images were first processed using the *ESA* NEST SAR Toolbox v.5.1 software. Additional analysis of the Envisat images was performed by undersampling 3x3 pixels followed by reprojecting to geographical grid. Resampling is often sufficient for recognizing oil phenomena on the sea surface. It also allowed handling of large files so that these can be imported in GeoMixer tool (SCANEX Group: www.scanex.ru). Images are typically exported to GeoTIFF format.

After pre-processing (converting to a common format and geographical projection) and masking some elements (small islands, wind-dampening areas), the main task was detection of dark patches and bands in the images. Then adaptive thresholding was applied (Solberg et al. 1999, Solberg et al. 2003), because the radar contrast between a dark spot and the surrounding waters depends on weather conditions. Oil slicks identified on SAR images were analyzed with purpose to eliminate similar signatures generated by oil pollution of ships, biogenic slicks and other similar based on the following parameters: shape, size and aspect ratio, contrast, repetition in time and space, wind speed and contextual information. We tried to discriminate oil that originates from known sources, such as ship discharges or natural biogenous slicks.

The suspect slicks are further discriminated from look-alikes of oceanographic, atmospheric and coastal origin (Oluić et al. 2014). SAR images in GeoTIFF format were then imported to the GeoMixer and through this application the slicks were also registered, e.g. separated from homogeneous sea water. The GeoMixer allows performing of interactive analysis of geospatial data. This is a web-GIS application for collection, visualization, analysis, mapping and generation of information products based on satellite imagery. The images were imported and superimposed over geographic-bathymetric/nautical maps available in either in GeoMixer or outside. This system almost automatically generates final remote sensing products, e.g. oil spill maps, as drawn spills in additional layer. All detected oil slicks were vectorized, removed from an image background and put on the map projection. Finally, oil spill distribution layers in vector format were integrated in GeoMixer tool.

The GeoMixer allowed the mosaics to be created, as a summary of all images, merged on the bathymetric maps. All detected oil slicks from all SAR images were merged together in one layer covering the area of interest, and in such a way, the synthetic mosaic map of all detected spills was created.

At the same time the oil slicks and seep slicks were divided based on remote sensing data according to categories of probability: highly, moderately and low probable. The assigned attributes ranged from high probability (representing high confidence that the detected slick could represent oil seeps) to low probability (representing the slicks which could not represent oil seeps) as indicated through the categories of signature, morphology and detectability as highly probable,

moderately probable and low probable. In almost all cases, the results of analysis with GeoMixer coincided with previously detected spills from visual analysis of images and processed in the NEST software.

Since the oil releases from the sea floor sources are periodic to episodic in nature, the timing of the release is not deterministic, spatial- and temporal variability of oil slicks was studied from the time series of acquired SAR images. In order to see if oil slick occurred in similar locations in different times, the mosaic of all detected spills was brought to a simple drawing tool where slicks were analyzed by years and categories, and presented as a final summary map.

Very frequently, it was possible to detect candidates for natural oil seeps from grouping or clustering (recurrent in space) of oil slicks on the sea surface as dark signatures in SAR images acquired at different dates. If these structures are repeated in time, this provides additional evidences of the release points, i.e., location of seep sources. The exact identification of the oil slick on SAR images is of mayor importance to estimate volume of the discharged oil and indicators of presence of petroleum potential in the explored area.

Results

Radarsat-2 Images from 2013

Radarsat-2 SAR image acquired on 2013-08-30 (Figure 4) was analyzed accompanied with the wind extraction for the area of interest and presented in the Figure 5.

Figure 4. *Geo-Referenced Image from 2013-08-30, 16:40 UTC*

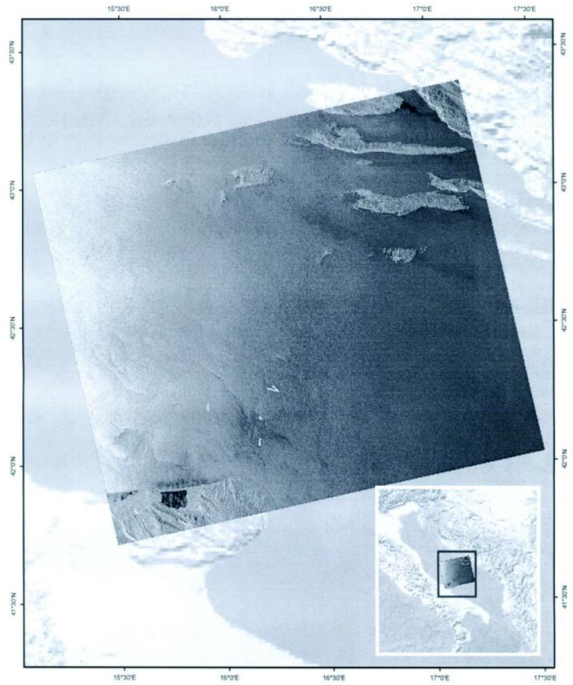

Source: © MDA- Geospatial Services Inc.

Figure 5. *Wind Extraction Result (Speed and Direction Values) Derived from the Radarsat-2 Image from 2013-08-30*

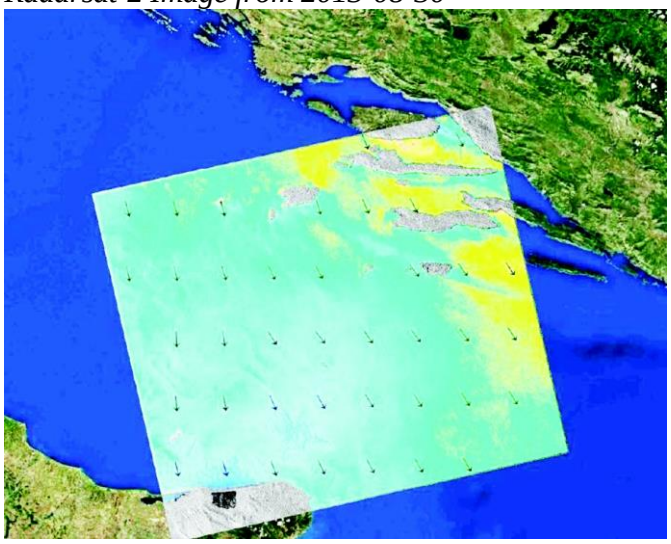

In Figure 4, a number of groups of slicks can be recognized as well as some individual slicks. Some groups of slicks definitely may be of different origin. Eventual candidates for oil seeps are mainly individual slicks, presented at enlarged segments and are marked by letters (Figure 6).

Figure 6. *Enlarged Subscenes of the Radarsat Image from 2013-08-30 with Detected Oil Spill/Slicks-Dark Patches (Blue-Anthropogenic, Green-Anthropogenic or Biogenic Slicks, Red Slicks Probably Related to Oil Seeps)*

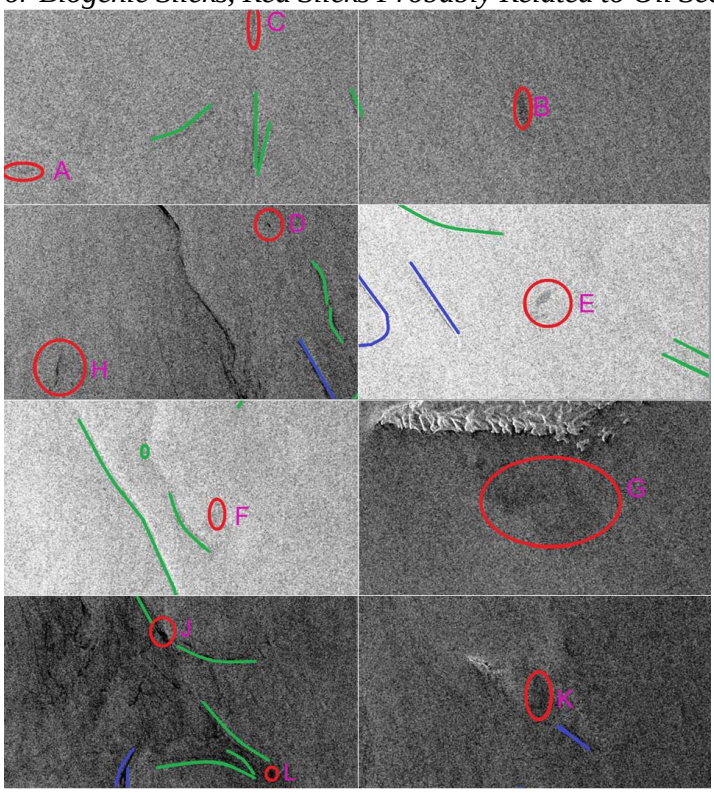

Beside a number of anthropogenic slicks and eventual biogenic slicks, it is possible to see high number of individual slicks marked in red as probable surface manifestations of oil seeps. Some of them are recognized as old once, since are spread over a larger area in the course of time, like those marked by A, B, E. Some slicks look fresh, like D and H. The three processed and geo-corrected Radarsat images were imported to GeoMixer and presented (Figure 7), where the locations of slicks are show by green squares. It is visible that the oil slicks have been grouped around Vis Island and around of Palagruža Islet, northeast of Gargano.

Figure 7. *Summary Map of Detected Oil Slicks from the Radarsat Images Acquired in 2013, (Green Squares) and Meteorological Stations (Black Triangles)*

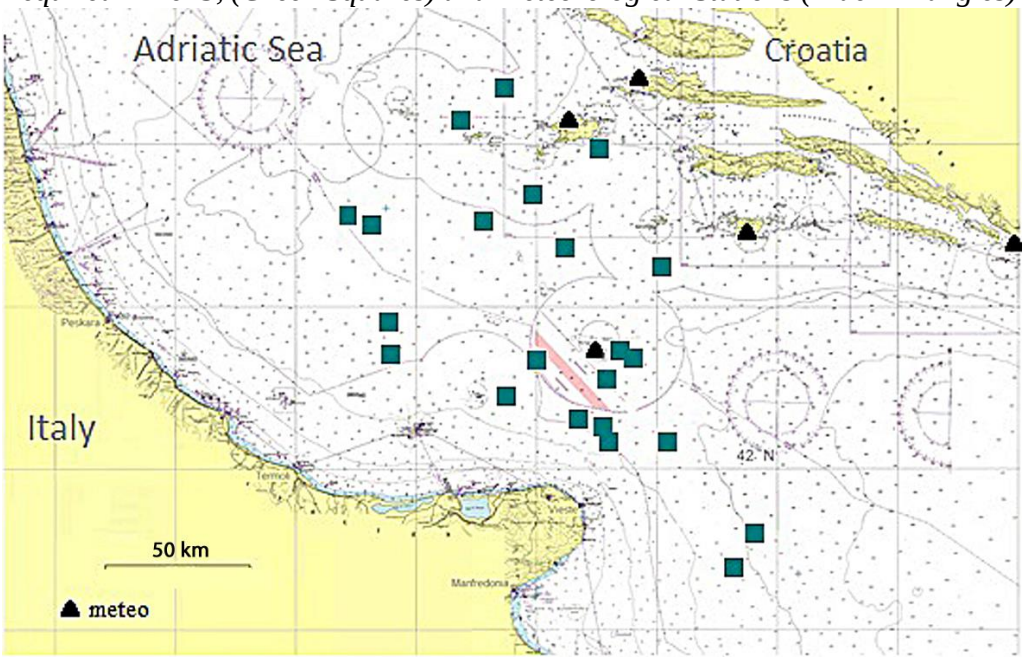

ENVISAT SAR Images from the Period 2003-2011

We selected the Envisat SAR imagery, which showed the potential oil phenomena and analysed them first via the NEST software (ESA) and latter through GeoMixer application. The software allows determination of geographical coordinates for every detected slick. It was possible to recognize many slick occurrences, although it was difficult to determine with certainty the origin of slicks. Nevertheless, on the SAR images it was possible to recognize and separate natural biogenic oil slicks from seep slicks. Focusing on every slick in every image, enlarging it several times, detailed view allowed obtaining characteristics of a particular oil slicks and attributing of their nature with some degree of probability. The GeoTIFF format images were imported to GeoMixer and through this software, the slicks were delineated.

It was noted that a number of observed slicks per image varied between images. Some SAR images have much higher number of slicks than others. Slick grouping detected in some SAR images could be indication of possible seep source.

Detecting slicks on SAR images strongly depend on the wind speed at the sea surface. A suitable wind speed, generally between 2 m/s and 6-7 m/s, was considered as a discriminating factor for acceptance of the images. If the wind was within the acceptable range over most of the area of interest, the SAR image is considered, and any areas of either too low or too high wind speed was in the latter phase masked-out and not used for analysis. Therefore, accompanying data for this analysis were also the wind data. Initially, for each time, when the images were acquired the wind speed was obtained from the SAR data or from meteorological stations located on the nearby islands or coast, as shown in the Table 2.

Table 2. *Example of 10-minutes Average Wind Speeds, Maximum 10 Minutes Gusts (m/s) with Directions Measured at Meteorological Stations for Dates and Hours of SAR Images: 20/11/2008, 23/07/2009 and 18/11/2009*

Wind (m/s)										
Weather station/ time	Hvar		Komiža		Lastovo		Palagruža		Prevlaka	
	10 min average speed	max.10-min gust	10 min average speed	max. 10-min gust	10 min average speed	max. 10-min gust	10 min average speed	max. 10-min gust	10 min average speed	max. 10-min gust
20.11.2008										
09:10	0.8	1.2	2.5	5.5			4.5	4.9	3.4	5.2
	45	62	343	338			298	287	11	28
09:20	0.6	0.8	3	5.5			3.6	5.3	4.2	5
	68	73	343	343			298	281	28	11
23.07.2009										
09:10	1.7	3.5			2.4	3.2	5.7	6.7	1.2	1.8
	129	141			146	146	158	146	96	141
09:20	1.7	3.3			1.8	2.6	6.2	6.8	0.7	2.1
	118	113			186	186	158	152	90	84
18.11.2009										
09:10	0.2	0.8	4.7	5.1	0	0	0.5	3.7	3	3
	124	118	343	338			180	208	6	6
09:20	0.6	0.9	2.5	4.8	3.1	3.2	1.1	2.9	3.6	6
	214	225	326	349	321	304	315	253	6	6

Source: Data from State Hydrometeorological Institute, Zagreb).

The wind data of meteorological wind fields derived from satellite images were also available through SCANEX. However, the shape and position of slicks was also strongly influenced by the sea currents.

On the Envisat SAR image from 2003-06-21 a large number of oil slicks of different forms and origin were detected (Figure 8), within the marked fields A, B, C. In enlarged parts of this image it is possible to observe sickle-like form of some

spills, and some of them were attributed to seep manifestations. In the Table 2 it is obvious that the wind speed was within the frame of the acceptable wind-speed conditions (average 5.2 m/s) suitable for oil slicks detection on the satellite SAR imagery.

On the Envisat SAR image from 2011-06-24 it is possible to recognize several slicks (1, 2, 3) of different forms and origin (Figure 9). The enlarged part of the image with oil slicks (2) is very distinctive and we recognized these as a sequence of seeps (encircled by red ellipse).

After creating mosaic of Envisat images in GeoMixer, it enabled delineating of slicks in different layers. The software allowed handling of slicks/spills independently from images and showing all slicks from different images together with a background map (Figure 10).

Figure 8. *Envisat SAR Image from 2003-06-21, 09:15 UTC (A); Enlarged Areas B, C and E where Large Number of Oil Slicks were Detected, and Especially Enlarged Segment 8 from Area C (D)*

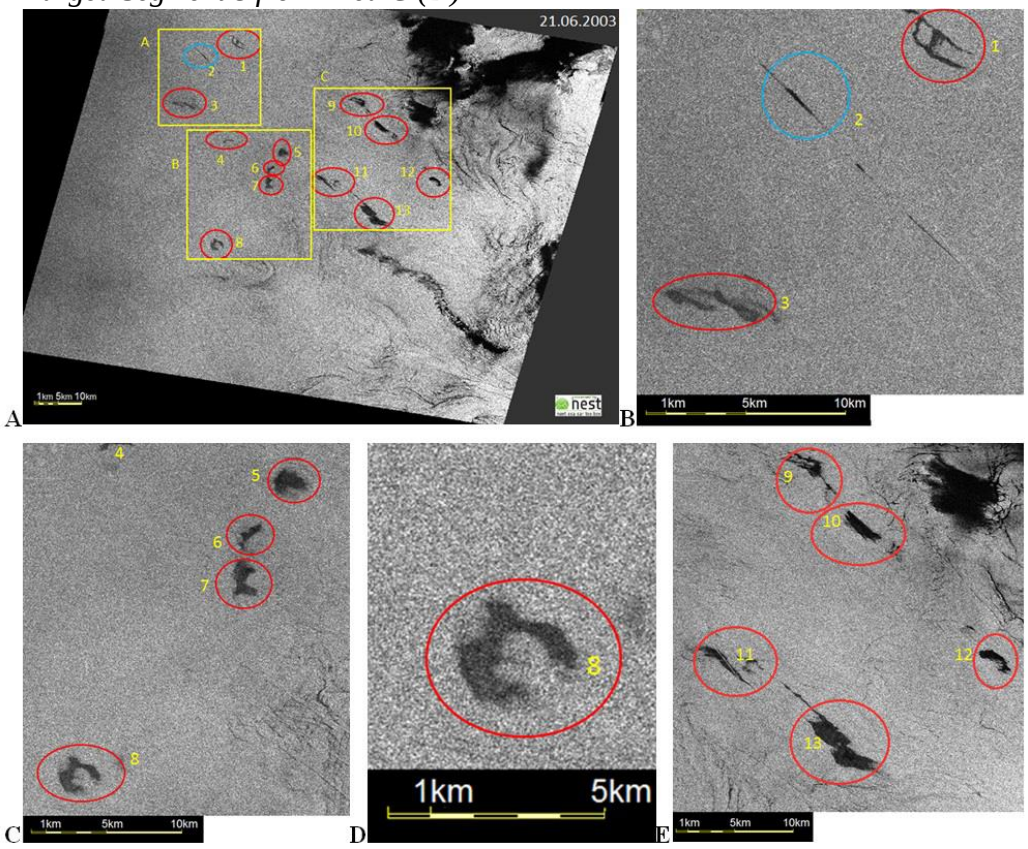

Source: © ESA.

Figure 9. (Left) *Envisat SAR Image (2011-06-24), 09:17 UTC;* (Right) *Enlarged Segment of Area 2 from the Same Image*

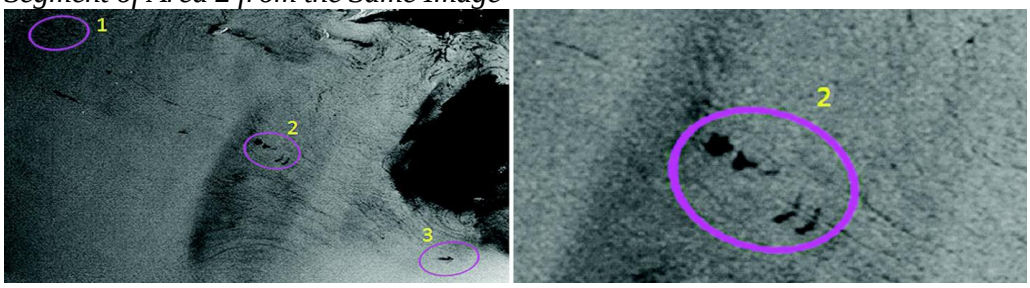

Source: © ESA.

The advantage of this approach is that all detected spills from all images in the investigated area could be seen on a single map, in order to see better their distribution and concentration. As seen from Figure 10, prevailing direction of elongated slicks is along the long axis of the Adriatic Sea, while lower numbers of slicks are oriented perpendicular to the Adriatic axis. Beside elongated forms, many small slicks have circular or sickle-like forms.

Figure 10. (Left) *Mosaic of the Envisat SAR Images with Detected Oil Slicks 2003-2011;* (Right) *Summary Map of the Same Data on the Background of Nautical Charts*

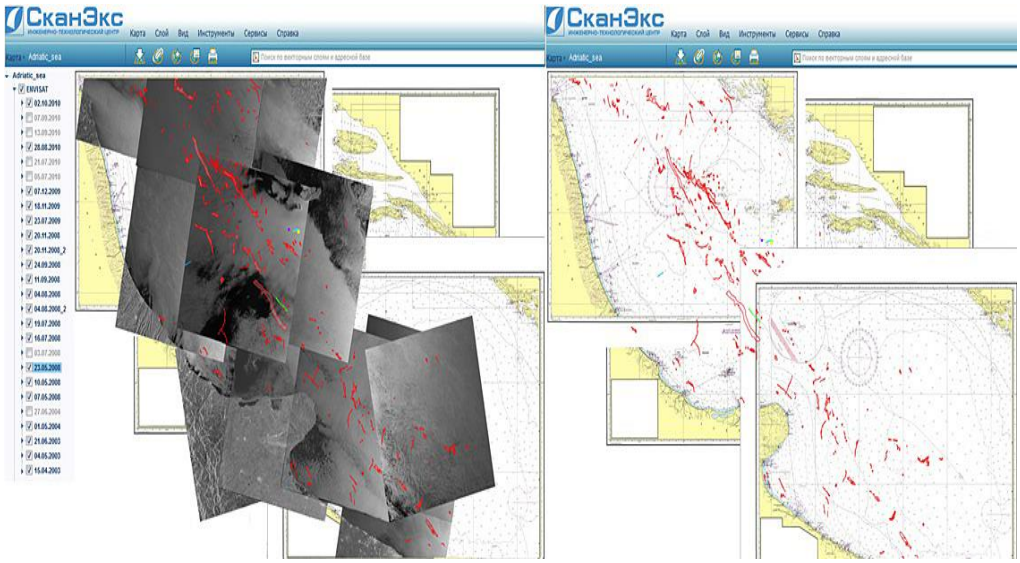

The summary map of detected oil slicks/seeps manifestations by *years* in the Middle Adriatic according to analysis of SAR images (Envisat and Radarsat-2) in the period 2003-2013 is shown on Figure 11. Slicks concentrate mostly in a few areas, e.g., west and southwest of Vis Island; southwest of Lastovo Island and east of Gargano. Small groups of slicks occurred also closer to the Italian coast at several locations. Based on selected criteria, it was possible to present spatial distribution of observed oil slicks/seep manifestations according to *categories of probability* (Figure 12). The slicks in blue color are probably from anthropogenic, ship origin. They mostly have elongated shape and are distributed along the long

Adriatic axis. Green colored slicks, distributed both along the Adriatic axis as well as transverse to the long axis, came also mostly from anthropogenic origin (fishing vessels or else). Most probable seep manifestations, shown in red, have the smallest size and are distributed mostly in the middle part of the Adriatic Sea.

It is obvious that some of the registered oil occurrences belong to the anthropogenic origin, but it is also clear that a part of them could have natural origin, either are natural biogenic films of planktonic origin or from natural seeps at the sea floor, which was of our primary interest. In order to be sure which one among registered oil slicks on SAR images are seep manifestations it would be necessary to analyze continuous flow of satellite SAR images acquired during a longer period of time and perform *in situ* sampling for chemical analysis.

Figure 11. *Summary Map for the Middle Adriatic of Detected Oil Slicks and Possible Seep Manifestations by Years, Based on the Analysis of Envisat and Radarsat-2 SAR Images for the Period 2003-2013*

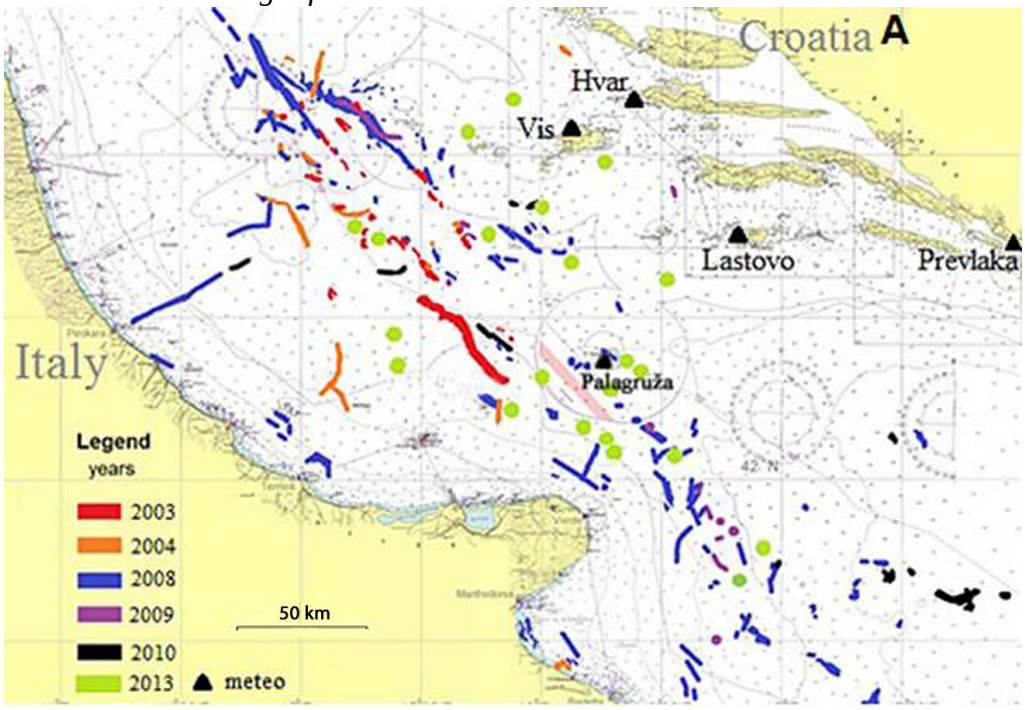

Figure 12. *Summary Map for the Middle Adriatic of Detected Oil Slicks and Possible Seep Manifestations by Categories, Based on the Analysis of Envisat and Radarsat-2 SAR Images for the Period 2003-2013*

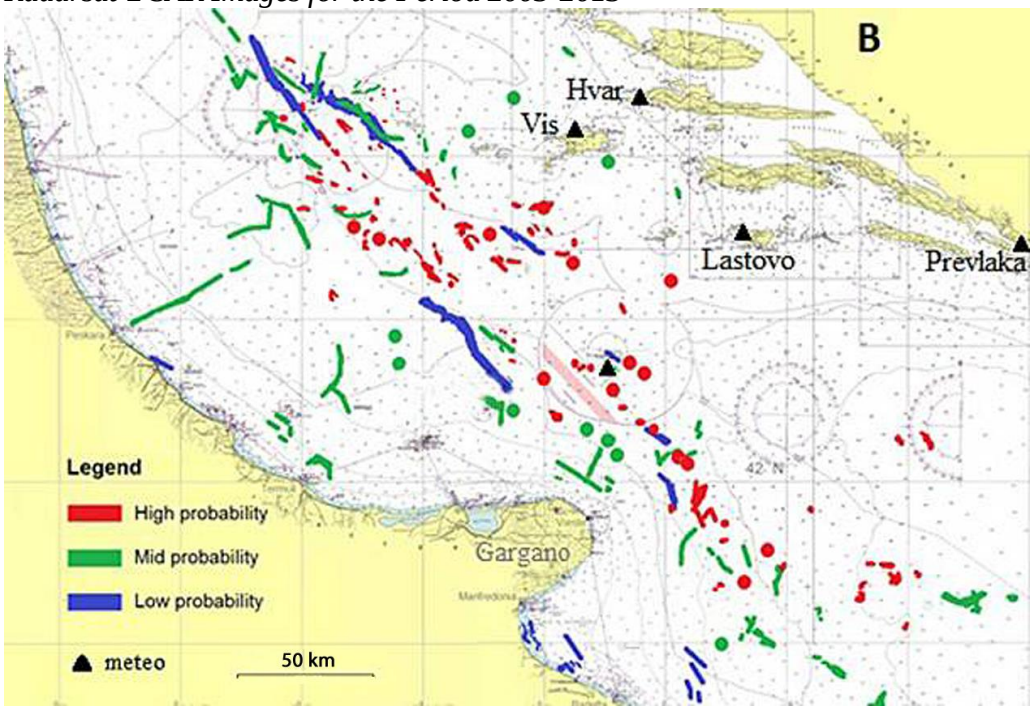

Oil Slicks and their Connection to the Seismotectonic Activity

The correlation between oil slicks concentration and tectonic structures and epicenters of earthquakes in the Middle Adriatic indicates that there is a connection between local tectonic ruptures, earthquake epicenters and oil slick phenomena since these occur most often along the brinks of the step-like East side of Middle Adriatic submarine depressions.

The basement of sedimentary rocks, i.e., the crystalline complex beneath the Adriatic Basin, is morphologically well expressed. It is characterized by many submerged depressions and emerged structures. The most important depression is CAD, oriented NW-SE (Figure 12).

Figure 13. *The Structure and Morphology Map with Isobaths of Cristalline Rocks and possible Oil Slick Fields (A, B, C, D) in the Middle Adriatic*

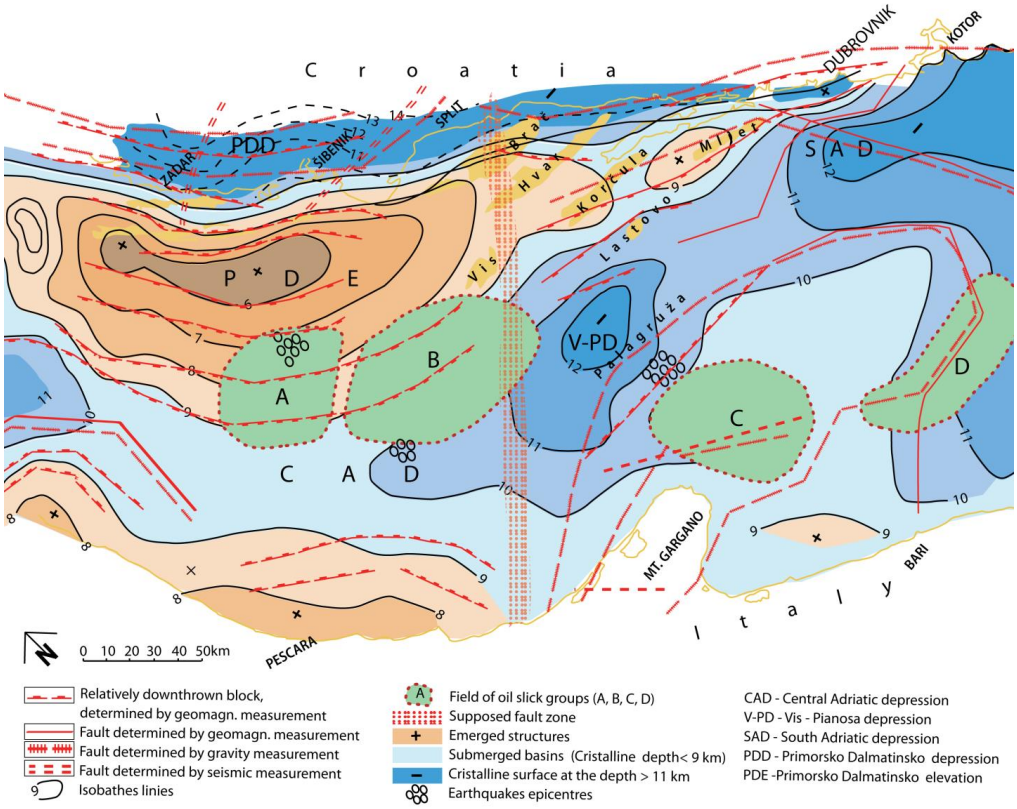

Source: Brdarević and Oluić 1979; simplified.

This depression has been formed by activity of numerous faults stretching along the eastern part of the Adriatic depression. By the parallel faulting, there developed a gradually-stepwise profiled submarine slope, directed towards the central part of the depression where crystalline rocks lie at depths of more than 9 km (the seabed depth varies in that region from 0 down to 190 m). The CAD is well separated by the regional transversal deformation zone Gargano-Split from the Vis-Pianosa Depression (V-PD).

The oil slicks are grouped in four fields (Figure 13). It is presumed that the concentration of registered oil slicks is connected to the local fracture system, whose earthquake activity enabled formation of pathways for liquid hydrocarbons (Field A). The group of oil slicks observed southwest of the Vis Island lies on the brink of the step-like profiled slope zone, formed by faulting, and associated to seismically active Field B. In the two fields east of Gargano, numerous oil slicks have been determined (Fields C and D). The Field C is situated between faults on the brink of V-PD. It is also associated with a remarkable seismic activity. Somewhat east of that field lies the Field D. It is characterized by the concentration of oil slicks extending along the fault, on the brink of South Adriatic depression. The sea depth at both fields and surrounding area ranges between 120-1,200 m.

Conclusions

The Envisat and Radarsat-2 SAR images have been used for slicks/seeps detection and their mapping in the Middle Adriatic, determining their frequencies and approximate oil leak sources. For these purpose a series of 34 SAR images acquired through the period of 10 years (2003-2011 and in 2013) have been processed and analysed.

In the Middle Adriatic, the sedimented rocks consist mostly of carbonate and evaporites with sources and reservoirs bearing hydrocarbons. Seismotectonic activity formed vertical and sub-vertical faults and fractures which can create pathways for fluid seepage so that gas and oil can migrate from seabed to the sea surface.

The oil slicks identification on satellite SAR images was performed by differing contrasts between the surface slicks and surrounding clear sea water. Using GeoMixer tool it was possible to register and separate slicks of different origin and determine their main characteristics.

Analyses of spatiotemporal distribution of oil slicks on satellite images enabled detecting of hot spots with persistence and temporal recurring in the same locations that indicates the presence of natural seeps.

Oil slicks were assigned according to the developed confidence levels of high, mid or low probability. The registered oil slicks and possible seeps were sorted by years and by categories of probability. Most slicks were of anthropogenic origin, but recurrent slicks at some places indicate natural seepage phenomena in the Middle Adriatic. The registered seepage slicks were concentrated in several fields. These phenomena were linked to local active faulting and associated earthquake activity which created pathways for fluids, gas bubbling and oil seeping. That can be an important indicator of hydrocarbon accumulations in the seabed. Our results suggest that annual seepage rates in the Middle Adriatic require further a systematic investigation of an extensive SAR time series.

Acknowledgements

Authors are very grateful to INA-Oil Co., Zagreb, Croatia, who partially supported this work (No: SN-1138/13). We also acknowledge the European Space Agency (ESA) for providing the Envisat SAR images through the ESA research project #19234 (PI M. Oluić). The work of Russian co-author was supported by the state assignment of the Russian Federal Agency of Science Organizations, theme No. 0149-2019-0003.We thank SCANEX Group (Russia) for opportunity to use GeoMixer application and web resources for processing and analysis of SAR images.

References

Akar S, Lutfi Süsen M, Kaymakci N (2011) Detection and object-based classification of offshore oil slicks using Envisat-ASAR images. *Environmental Monitoring Assessment* 183(1-4): 409-423.

Battaglia M, Murray HM, Serpelloni E, Bürgmann R (2004) The Adriatic region: an independent microplate within the Africa-Eurasia collision zone. *Geophysical Research Letters* 31(9): L09605.

Bayramov E, Kada M, Buchroithner M (2018) Monitoring oil spill hotspots, contamination probability modelling and assessment of coastal impacts in the Caspian Sea using SENTINEL-1, LANDSAT-8, RADARSAT, ENVISAT and ERS satellite sensors. *Journal of Operational Oceanography* 11(1): 27-43.

Brdarević N, Oluić M (1979) *Contribution to the knowledge of tectonic structure of the Adriatic Sea bottom*. Proceedings of the Faculty for Mining-Geology-Petroleum Engineering, University of Zagreb, on the Anniversary of the Establishment 1939-1979, 1-14.

Brekke C, Solberg AHS (2005) Oil spill detection by satellite remote sensing. *Remote Sensing of Environment* 95(1): 1-13.

Brkić V, Križ J, Omrčen B, Bejdić G (2013) Projekt Južni Jadran i primjena suvremenih tehnoloških dostignuća pri izradi istražne bušotine u podmorju dubokog mora (The project Southern Adriatic and application of recent technological achievements during experimental drilling in deep water seabed). Naftaplin: *Znanstveno-stručno glasilo Hrvatske udruge naftnih inženjera i geologa* 75: 54-74.

Casero P, Bigi S (2013) Structural setting of the Adriatic basin and the main related petroleum exploration plays. *Marine and Petroleum Geology* 42(Apr): 135-147.

Castello B, Selvaggi G, Chiarabba C, Amato A (2006) *Catalogo della sismicita. 1981-2002 ver.1.1* (Seismicity catalogue 1981-2002 ver.1.1). Roma, Italy: Instituto Nazionale di Geofisica e Vulcanologia – CNT.

Conti A, Stefanon A, Zuppi G (2002) Gas seeps and rock formation in the northern Adriatic Sea. *Continental Shelf Research* 22(16): 2333-2344.

Cota L, Troskot-Čorbić T, Koch G, Pandžić M (2015) *"Burno" facies as a key factor in hydrocarbon exploration of Middle and South Adriatic*. Proceedings of 8th International Conference and Exhibition on Oil and Gas Management, Šibenik, Croatia, 13-16 June 2015. Croatian Association of Mining Engineers No. 143-144, 71-78.

Curzi VP, Veggiani A (1985) I pockmarks nel mare Adriatico centrale (The pockmarks in the central Adriatic Sea). L'Ateneo Parmense. *Acta Naturalia* 21: 79-90.

Dando PR, Hughes AJ, Leahy Y, Niven JS, Taylor JL, Smith C (1995) Gas venting from submarine hydrothermal areas around the island of Milos, Hellenic Volcanic Arc. *Continental Shelf Research* 15(8): 913-929.

Devoti R, Ferraro C, Gueguen E, Lanotte R, Luceri V, Nardi A, Pacione R, Rutigliano P, Sciarretta C, Vespe F (2002) Geodetic control on recent tectonic movements in the central Mediterranean area. *Tectonophysics* 346(3-4): 151-167.

Etiope G (2014) *Natural gas seepage: the earth's hydrocarbon degassing*. Springer. ISBN=978-3-319-14600-3. DOI=10.1007/978-3-319-14601-0.

Etiope G, Panieri G, Fattorini D, Rgoli F, Vannoli P, Italiano F (2014) A thermogenic hydrocarbon seep in shallow Adriatic Sea (Italy): gas origin, sediment contamination and benethic foraminifera. *Marine and Petroleum Geology* 57: 283-293.

Evtushenko NV, Ivanov AY (2013) Oil seep manifestations in the southeastern Black Sea studied using satellite synthetic aperture radar images. *Izvestiya, Atmospheric and Oceanic Physics* 49(9): 913-918.

Friedman KS, Pitchel WG, Clemente-Colon P, Li X (2002) *GeoMEx - an experimental GIS system for the Gulf of Mexico region using SAR and additional satellite and ancillary data*. Proceedings of International Geoscience and Remote Sensing Symposium (IGARSS'02). IEEE International. DOI=10.1109/IGARSS. 2002.1027 177.

Geletti R, Del Ben A, Busetti M, Ramella R, Volpi V (2008) Gas seeps linked to salt structures in the Central Adriatic Sea. *Basin Research* 20(4): 473-487.

Girard-Ardhuin F, Mercier G, Garello R (2003) *Oil slick detection by SAR imagery: potential and limitation*. Proceedings of the Marine Technology and Ocean Science Conference OCEANS 2003, 22-26 September 2003, San Diego, USA.

Grandić S, Boromisa-Balas E, Susterčić M, Kolbah S (1999) Hydrocarbon possibilities in the Eastern Adriatic Slope zone of Croatian offshore. *Nafta* 50(2): 51-73.

Gurevich AE, Chilingarian VG (1993) Subsidence overproducing oil and gas fields, and gas leakage to the surface. *Journal of Petroleum Science and Engineering* 9(3): 233-238.

Hovland M, Curzi P (1989) Gas seepage and assumed mud diapirism in the Italian Central Adriatic Sea. *Marine and Petroleum Geology* 6(2): 161-169.

Hovland M, Gallagher VJ, Clennell BM, Lekvan K (1997) Gas hydrate and free gas volumes in marine sediments: example from the Niger Delta front. *Marine and Petroleum Geology* 14(3): 245-255.

Hovland M, Gardner JV, Judd AG (2002) The significance of pockmarks to understanding fluid processes and geohazards. *Wiley Editing Services. Geofluids* 2(2): 1-36.

Hu C, Li X, Pichel WG, Muller-Karger FE (2009) Detection of natural oil slicks in the NW Gulf of Mexico using MODIS imagery. *Geophysical Research Letters* 36(1): L01604.

Ivanov AY (2012) Unique phenomena in Lake Baikal, Russia imaged and studied with SAR and multi-sensor images. *International Journal of Remote Sensing* 33(23): 7579-7598.

Ivanov AY, Zatyagalova VV (2008) A GIS approach to mapping oil spills in a marine environment. *International Journal of Remote Sensing* 29(21): 6297-6313.

Judd A, Hovland M (2007) *Seabed fluid flow: impact on geology, biology and the marine environment*. Cambridge University Press.

Kouznetsov OV, Sidorov IV, Katz S, Chilingarian VG (1994) Interrelationships among seismic and short-term tectonic activity, oil and gas production, and gas migration to surface. *Journal of Petroleum Science and Engineering* 13(1): 57-63.

Kvenvolden KA, Cooper CK (2003) Natural seepage of crude oil into marine environment. *Geo-Marine Letters* 23(3): 140-146.

Leifer I, Luyendyk KB, Broderick K (2006) Tracking an oil slick from multiple natural sources, Coal Oil Point, California. *Marine and Petroleum Geology* 23(5): 621-630.

Lušić Z, Kos S (2006) Glavni plovidbeni putovi na Jadranu (The main sailing routes in the Adriatic). *Naše More* 53(5/6): 198-205.

MacDonald RI, Guinasso NL, Ackleson SG, Amos JF, Duckworth R, Sassen R et al. (1993) Natural oil slicks in the Gulf of Mexico visible from space. *Journal of Geophysical Research* 98(C9): 16351-16364.

Mattavelli L, NovelliL, Anelli L (1991) Occurrence of hydrocarbons in the Adriatic basin. *AAPG* 1: 369-380.

Mazzetti L, Segantin S, Tramontana M, Wezel CF (1987) Characteristics of pockmarks in the Jabuka Trough floor (Central Adriatic Sea). *Bolletino di Oceanologia Teorica e Applicata* 3: 237-249.

Morović M, Ivanov A (2011) Oil spill monitoring in the Croatian Adriatic waters: needs and possibilities. *Acta Adriatica* 52(1): 45-56.

Morović M, Ivanov A, Oluić M, Kovač Ž, Terleeva N (2014) *Distribution and sources of oil slicks in the Middle Adriatic Sea*. Proceedings of 12th Pan Ocean Remote Sensing Conference PORSEC, 4-7 November 2014, Bali, Indonesia.

Morović M, Ivanov A, Oluić M, Kovač Ž, Terleeva N (2015) Oil spills distribution in the Middle and Southern Adriatic Sea as a result of intensive ship traffic. *Acta Adriatica* 56(2): 145-156.

O'Brein GW, Lawrence MG, Williams KA, Glenn K, Barrett GA, Lech M et al. (2005) Yampi Shelf, Browse Basin, North-West Shelf, Australia: a test-bed for constraining hydrocarbon migration and seepage rates using combinations of 2D and 3D seismic data and multiple, independent remote sensing technologies. *Marine and Petroleum Geology* 22(4): 517-549.

Oluić M, Morović M, Ivanov A (2014) On application of SAR imagery from mapping of natural oil slicks in a part of Adriatic Sea. *INA-Report, Zagreb,* 175.

Oluić M (2015) *Earthquakes-causes and consequences with regards to Croatia and neighboring regions*. Zagreb: Prosvjeta.

Pikelj K, Hernitz-Kučenjak M, Aščić Š, Juračić M (2015) Surface sediment around the Jabuka Islet and the Jabuka Shoal: evidence of Miocene tectonics in the Central Adriatic Sea. *Marine Geology* 359(1): 120-133.

Solberg AHS, Storvik G, Solberg R, Volden E (1999) Automatic detection of oil spills in ERS SAR images. *IEEE Transactions in Geosciences and Remote Sensing* 38(4): 1916-1924.

Solberg AHS, Doken ST, Solberg R (2003) *Automatic detection of oil spills in ENVISAT, RADARSAT and ERS SAR images*. Proceedings IGARSS. IEEE 4: 2747-2749.

Soloviev A (2002) *Global estimation of gas content in submarine gas hydrate accumulations*. Proceedings 6 International Conference on Gas in Marine Sediments. St. Petersburg, Russia, 2000: 123-125.

Stefanon A (1981) *Pockmarks in the Adriatic Sea?* 2nd European Regional Meeting, Association of Sedimentologists, Bologna, Italy: 189-192.

Tary BJ, Gèly L, Guennou C, Henety P, Sultan N, Çağatay N, Vidal V (2012) Microevents produced by gas migration and expulsion at the seabed: a study based on sea bottom recordings from the Sea of Marmara. *Geophysical Journal International* 190(2): 993-1007.

Topouzelis K, Muellenhoff O, Ferraro G, Tarchi D (2007) *Satellite mapping of oil spills in the East Mediterranean Sea*. Proceedings of the 10th International Conference on Environmental Science and Technology, 2007, September 5-7, Kos Island, Greece.

Trincardi, F., Cattaneo, A., Correggiari, A. and Ridente, D. 2004. Evidence of soft sediment deformation, fluid escape, sediment failure regional weak layers within the late Quaternary mud deposits of the Adriatic Sea. *Marine Geology* 213: 91-119.

Tufekčić D (2015) *Triassic evaporate facies and their significance on petroleum prospects, mid-Adriatic basin*. Proceedings of International Conference and Exhibition June 2015 on oil and gas management, Šibenik, Croatia, 143-144: 79-86.

Volpi V (2017) *Geologia marina. Part I Mare Italiano-Adriatico* (*Marine Geology*. Part I Italian-Adriatic Sea) Universita di Trieste, Anno Academico.

Wrigley R, Marszaleka A, Rodriguez K, Hodgson N (2014) Offshore Croatia-hunting 'Big Oil? In the centre of Europe- *First Break* 32(5): 61-68.

Zatyagalova VV, Ivanov AY, Golubov BN (2007) *Application of Envisat SAR imagery for mapping and estimation of natural oil seeps in the South Caspian Sea*. Proceedings of Envisat Symposium, 23-27 April 2007, Montreux, Switzerland (ESA SP-636) Noordwijk: ESA Publication Division.

Athens Journal of Technology & Engineering 2020, 7(2): 117-132
https://doi.org/10.30958/ajte.7-2-3

Influence of Autonomous Vehicles on Freeway Traffic Performance for Undersaturated Traffic Conditions

By Osama ElSahly[*] & Akmal Abdelfatah[±]

Autonomous vehicles (AVs) are smart driving technology that is expected to alter the perception of transportation. The purpose of this study is to evaluate the impacts of AVs on freeway traffic performance at different percentages of AVs ranging from 0% to 100% and at two different undersaturated traffic volume levels with demand to capacity ratios of 0.6 and 0.8. The well-known VISSIM software was used to develop a microsimulation model to evaluate different scenarios that represent different market penetration rates of AVs and different demand to capacity ratios. The results showed that the minimum improvement was at 5% AVs and 0.6 demand to capacity ratio and the maximum improvement was achieved at 100% AVs and 0.8 demand to capacity ratio. The increase in the average speed ranges from about 5% to about 15%, the reduction in travel time ranges from about 1% to about 12% and the delay reduction is about 18% to about 97%. The improvement in traffic performance when AVs market penetration rates increases from 0% to 100% is attributed to the fact that the conventional vehicles (CVs) are replaced by AVs that can travel with higher constant speed and with a smaller time headway. Statistical t-test was carried out to examine the statistical significance of the difference between scenarios' average speeds and between the average speed of both AVs and CVs. The test revealed that there average speed values of AVs are significantly higher than CVs values for all AVs market penetration rates at demand to capacity ratios of 0.6 and 0.8. Because at these demand to capacity ratios the congestion is low. Thus, AVs can travel freely with speeds significantly higher than CVs.

Keywords: *Autonomous vehicles, Freeway performance, Conventional vehicles, Average speed, Travel time, Delay*

Introduction

The significant development of the smart driving technology is expected to alter the perception of transportation and the Autonomous Vehicles (AVs) are becoming the next generation of transportation modes. In the past few years automation technology has gone through a huge development from semi-autonomous vehicles to fully autonomous vehicles. Major vehicles' manufacturers and IT companies are investing billions of dollars to produce and develop the next generation of vehicles (Hao 2017).

Within UAE, Dubai is taking a big leap in the adaption of artificial intelligence and becoming the world largest laboratory for technology, research and development. Dubai has launched a future transportation strategy to transform 25% of Dubai's transportation to autonomous modes by 2030 (WAM 2016).

[*]Graduate Student, American University of Sharjah, United Arab Emirates.
[±]Professor, American University of Sharjah, United Arab Emirates.

There are many challenges that are expected to face the implementation of this technology. One of the major challenges that are expected to happen is the interaction between AVs and Conventional Vehicles (CVs) in the traffic fleet, using the same roads. This is expected to happen at the early stages of the adoption, as the market penetration rate, for AVs (percentage of AVs) would not be 100%. The AVs will start with a small market penetration rates and later the market penetration rates will increase gradually until it ultimately reaches 100%. The purpose of this study is to evaluate the impact of AVs on freeway traffic performance at different market penetration rates (percentage of AVs in the traffic flow) values and at two different congestion levels (0.6 and 0.8 demand to capacity ratios).
The paper consists of five sections that are organized as follows:

- Section 1 provides a brief introduction about AVs and the research conducted in this paper.
- Section 2 presents a literature and background review about AVs definition, advantages and disadvantages.
- Section 3 discusses the methodology regarding the modelling of AVs and scenarios that were considered in this research.
- Section 4 shows the results obtained from the simulation runs, discussion and analyses of the results
- Finally, section 5 summarizes the research outcomes and includes recommendations for future work

Literature Review

This section provides a review of the existing relevant researches on AVs regarding their potential impacts on different aspects.

Definition and Levels of Autonomous Vehicles

AVs are defined as self-driving or driverless vehicles that can operate without a human driver to control driving tasks such as steering, braking, deceleration and acceleration, or monitor the roadway constantly. AVs use a combination of sensors such as radar, computer vision, LIDAR, sonar, GPS, odometry and inertial measurement units to perceive their surroundings. Sensory information is interpreted by advanced control systems for path navigation and identification of obstacles and relevant signage (Verre 2018).

According to the Society of Automotive Engineering (SAE 2018), automation levels are classified into six levels; with level 0 represents no automation (CVs) and level 5 shows a full automation, which is the considered level of automation in this study (i.e., level 5).

Benefits of Autonomous Vehicles

AVs have several advantages that include the safety, sustainability, efficiency, convenience, social benefits, traffic performance and environmental impacts. In addition, they are expected to eliminate human errors that can cause accidents such reducing greenhouse gases emissions (Simon et al. 2015). According to the National Highway Traffic Safety Administration (NHTSA), 94% of crash accidents are due to human errors, and more than 35,000 people died in serious accidents in U.S. in 2015. So, AVs can save a lot of lives by eliminating accidents caused by human errors (NHTSA 2018).

AVs are equipped with many sensors in addition to vehicle to vehicle (V2V), vehicle to infrastructure (V2I) communications and driver assistance technologies such as Adaptive Cruise Control (ACC) and Intelligent Cruise Control (ICC). These technologies can positively impact the traffic performance as vehicles that are equipped with these technologies can track the leading vehicle and estimate the speed and distance differences. Based on that, ACC automatically accelerates or decelerates the vehicle to maintain a safe headway at desired speed and prevents rear-end collisions. This can reduce or optimize gaps between vehicles on the road and results in a smooth and safe traffic flow. It was found that a small percentage of vehicles equipped with these technologies results in a drastic reduction in traffic congestion, and thus increases traffic stability and road capacity (Kesting et al. 2007, Ioannou and Chien 1993, Aria et al. 2016, Tientrakool et al. 2011, Arnaout and Bowling 2011). This is consistent with the findings of the report Co-published by World Economic Forum and Boston consulting group in 2018. The results of the reports revealed that AVs are expected to cut urban travel time by 4%

In addition, AVs reduce the parking spaces needed in the city by 43.5%. As AVs can parks on their own after dropping the users at any remote parking lots outside the city. Also, they can park more closely to each other.

Furthermore, AVs can have social impacts by providing independent mode of transportation for disabled and elder people. In addition, they can reduce the stress on the drivers and increase the utility of in-vehicle time by enabling the passengers to do other activities during travel time rather than driving tasks (Litman 2014, Das et al. 2017).

The inclusion of AVs in an urban traffic fleet and its impact of AVs on urban air quality have been evaluated in a recent research. The results revealed that the increase of AVs market penetration rates in traffic fleet was associated with a decrease in Nitrogen Oxides (NOx) and Carbon Dioxide (CO_2) concentration in the air. Thus, AVs have the potential to improve urban air quality (Rafael et al. 2020).

Disadvantages and Risks of AVs

Although the implementation of AVs is expected to have many positive impacts, but there are also some negative potential impacts. The interaction between AVs and CVs and automation failure are examples of these possible negative impacts. In addition, there are some technical obstacles and risks

associated with the AVs. Such obstacles must be overcome to ensure that the AVs are safe to be used by travelers for daily travel. Testing AVs is used to reveal any risks or errors associated with these vehicles. The increase of automation level can lead to overreliance on automation that will degrade driving skills. This could be dangerous in case of system failure (Strand et al. 2014). Moreover, AVs can encourage people to travel more and thus increase vehicle miles' travel (VMT) and greenhouse emissions since they can provide an easy, comfortable and safe mode of transportation. In addition, added population of new travelers of elderly and disabled people can also increase VMT and greenhouse emissions (Bierstedt et al. 2014).

The limitations and risks of Automated Driving System (ADS) have been evaluated in a recent research work. It was concluded that a compromise between human driving and ADS is better to avoid the risks associated with ADS and get the maximum benefits of ADS (Bocca and Baek 2020).

Barriers to Implementation

AVs' cost is one of the major barriers to large-scale market adoption of these vehicles. AVs have technology needs that include sensors, communication software and guidance technologies that increase their cost besides engineering and computing requirements. These software and hardware costs make AVs unaffordable for most of the people. It is expected that the cost of AVs will decrease with mass production and large-scale adoption similar to any other technological advances. In addition, some advocates claim that fuel, insurance and parking-cost savings will partly offset these incremental costs (Fagnant and Kockelman 2015). This can make their price affordable over time and increase their ownership. In addition, lacking nationally recognized licensing and liability standards for AVs is considered as a main barrier to the implementation of AVs. Furthermore, there is a major concern on how to develop a robust system for AVs to protect their data and minimize the exposure to risk as they may be targeted or hacked by computer hackers or terrorists and manipulated remotely. Such actions can cause many problems such as accidents or traffic disruption or terrorism acts (Fagnant and Kockelman 2015).

Methodology

The microsimulation software VISSIM was used to build a simulation model of a mixed traffic of AVs and CVs in order to evaluate the impacts of AVs on traffic performance. The considered network consists of a 10-km stretch of a major freeway in Dubai (E 311) with five lanes in each direction and six junctions (two right-in-right-out junctions, a single point interchange and two full-cloverleaf junctions with additional ramps). The capacity of each lane is assumed to be 2000 vehicles per hour. Thus, the capacity of road is equal 10000 vehicles per hour in each direction. In addition, the posted speed is 110 Kph and the speed limit is 130 Kph.

AVs and CVs exhibit different driving behaviors that should be modeled to accurately simulate each type of vehicles. The driving behavior in microscopic traffic simulation is governed by several functions (such as; car following and lane changing behavior). Car following behavioral models control vehicle's longitudinal speed, acceleration and the gap between the lead vehicle and the following vehicle. Lane changing model determines when it is acceptable to change lanes and how to do so. The default driving behavior in VISSIM was used as a driving behavior model for CVs. However, some parameters in the default driving behavior were modified in order to model the presence of AVs in VISSIM. Using the VISSIM model, the impacts of AVs were evaluated at two demand to capacity ratios of 0.6 which corresponds to level of service C, and 0.8 which corresponds to level of service D. These two ratios are selected to represent under saturated conditions.

In addition, the impacts were evaluated at nine different market penetration rates (percentages) of AVs. The percentages of AVs were considered to be 5% to 25% with increments of 5%, to represent the early stages adoption and from 40% to 100% with 20% increment.

In total 18 scenarios were simulated. Each scenario was simulated for 5 runs using different random seed numbers, then the trimmed average of the three middle values for each scenario were considered as the average result (Aria et al. 2016, Ngan et al. 2004).

Modeling AVs

As mentioned before AVs have different capabilities and performance than CVs. AVs can be modeled in VISSIM through internal model interface and external interfaces as shown in Figure 1.

The presence of AVs was modeled by adjusting the default driving behavior parameters used in VISSIM to satisfy the main characteristics of AVs. VISSIM enables users to customize driving behavior parameters such as (car following, lane changing, lateral behavior and reaction to signal controls).

Although AVs driving behavior is under development, and there is no standard driving behavior model of AVs, in this research, AVs driving behavior model parameters are adjusted based on literature review.

Based on the general understanding of the driving behavior of AVs, it can be described as follows:

- AVs keep smaller standstill distance.
- AVs keep smaller headway.
- AVs keep the desired speed strictly (without a distribution).
- AVs accelerate & decelerate equally (without a distribution).

Figure 1. *AVs Modeling in PTV VISSIM (PTV Group, 2017)*

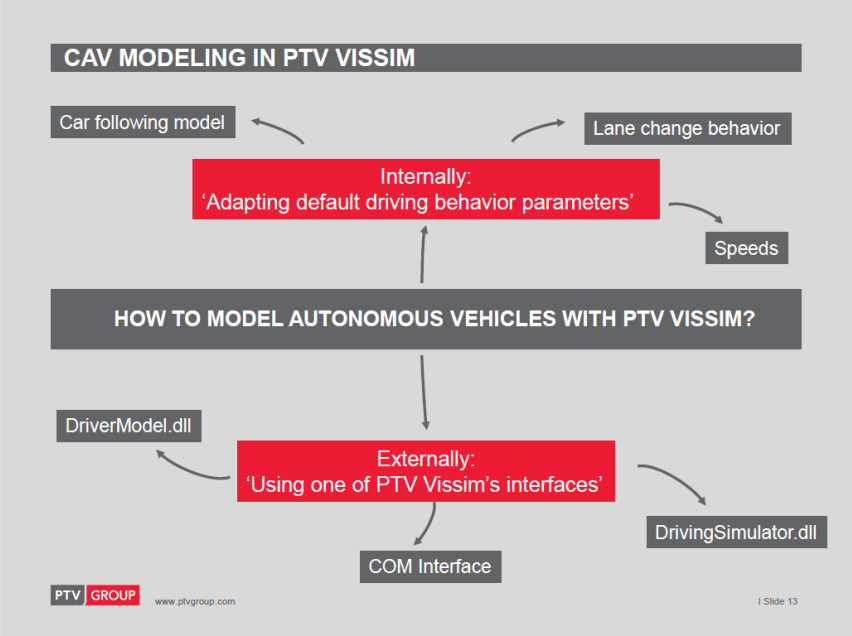

Results and Discussion

The impact of AVs on freeway traffic performance was evaluated at different market penetration rates (0%, 5%, 10%, 15%, 20%, 25%, 40%, 60%, 80%, and 100 %) and at two different demand to capacity ratios (0.6 and 0.8). Some statistical analyses were conducted to interpret the results obtained from simulation runs. Descriptive statistics such as trimmed average and standard deviation for each scenario were calculated. Moreover, t-test was carried out to test the hypotheses that were assumed and to examine the significance of the difference between scenarios.

Results Relative to Different Market penetration rates of AVs

In this section, the performance of both AVs and CVs (in terms of average speed, travel time and delay) for each demand to capacity ratio is evaluated at each AVs market penetration rates scenario. The numerical values, reported in this section, are the percent improvements or reductions for each demand to capacity ratio at different market penetration rates scenarios, compared to the baseline scenario, which is 0% AVs. Because of the lack of available data, the base model is not calibrated against real-life data. Therefore, the values of speed, travel time and delay are not of much interest and the numerical values, reported in this section, are the percentage of the increase or reduction for each market penetration rates scenario, compared to the baseline scenario, which is 0% AVs (i.e. 100% CVs).

It should be noted that at 100% AVs the traffic fleet consists of AVs only and no CVs exist in the network. Therefore, the discussion of average speed, travel time and delay will be for the AVs only.

Average Speed

The trimmed average of the speeds for AVs and CVs for 0.6 and 0.8 ratios were obtained at different market penetration rates scenarios. When the demand to capacity ratio is set to be 0.6 or 0.8, the average speeds for AVs and CVs are obtained for all AVs market penetration rates s, as summarized in Tables 1 and 2.

Table 1. *Percentage of Average Speed Improvement for AVs*

AVs market penetration rates	Demand to capacity ratio	
	0.6	**0.8**
5%	4.5	4.3
10%	5.0	4.9
15%	5.3	5.5
20%	5.5	6.1
25%	5.9	6.8
40%	6.8	8.3
60%	7.9	10.4
80%	8.8	12.5
100%	9.7	14.5

Table 2. *Percentage of the Average Speed Improvement for CVs*

AVs market penetration rates	Demand to capacity ratio	
	0.6	**0.8**
5%	0.2	0.5
10%	0.6	1.0
15%	0.7	1.3
20%	1.1	1.7
25%	1.4	2.3
40%	1.9	3.4
60%	2.8	5.1
80%	4.0	6.8

From Tables 1 and 2, the average speed for both AVs and CVs increased as AVs market penetration rate increased from 5% to 100%. When comparing the results of AVs and CVs it can be noted that AVs have higher improvement percentages than CVs. The improvement for AVs at 0.6 demand to capacity ratio ranges from about 5% with 5% AVs to about 10% with 100% AVs. On the other hand, the improvement for CVs ranges from about 0.2 with 5% AVs to around 4% with 80% AVs.

Moreover, noted form the two tables that improvement percentages increased with the increase of the demand to capacity ratio from 0.6 to 0.8. The percentage of improvement for AVs increased from about 10% to about 15% for AVs (at

100% AVs) and from about 4% to about 7% for CVs (at 80% AVs), which is consistent with Aria et al.'s (2016) findings that the positive impacts of AVs will be more efficient and highlighted when the network becomes more crowded.

Travel Time

Considering 0.6 and 0.8 demand to capacity ratios, the simulation results for the travel times for AVs and CVs, are discussed in this section. The comparisons in this section show the percentage of reduction in travel time, relative to the 0% AVs. For demand to capacity ratios of 0.6 and 0.8, the results are presented in Tables 3 and 4.

Table 3. *Percentage of Travel Time Reduction for AVs*

AVs market penetration rates	Demand to capacity ratio	
	0.6	**0.8**
5%	0.33	3.7
10%	0.67	4.5
15%	1.2	5.4
20%	1.3	5.6
25%	1.96	5.8
40%	3.5	7.1
60%	5.1	8.6
80%	6.6	10.1
100%	8.1	11.7

Table 4 *Percentage of Travel Time Reduction for CVs*

AVs market penetration rates	Demand to capacity ratio	
	0.6	**0.8**
5%	0.07	0.57
10%	0.26	0.2
15%	0.5	1.1
20%	0.48	1.6
25%	0.90	2.1
40%	1.8	2.7
60%	2.8	4.1
80%	3.4	5.5

Similar to what was observed in average speed results, Tables 3 and 4 show that the travel time improved as the market penetration rates of AVs increased from 5% to 100%. At 0.6 demand to capacity ratio the travel time for AVs decreased by 8% with 100% AVs while the reduction in travel time for CVs is about 3.4% with 80% AVs. The reduction in travel time increased when the demand to capacity ratio increased from 0.6 to 0.8. The maximum reduction in travel time for AVs was obtained at 0.8 demand to capacity ratio with 100% AVs (about 12%), while the maximum reduction for CVs is about 5.5% with 80% AVs.

The reduction of travel time associated with the presence of AVs in the traffic is due to the fact the AVs travel with a smaller time headway (THW), compared to

CVs. This, in turn, increases the number of gaps in the network, and thus decreases the travel time of vehicles.

Delay

The delay is calculated by subtracting the free flow travel time (when the vehicles travel with posted speed) from observed travel time (when the vehicles travel with a speed less than posted speed). In addition, the ratios shown in the delay comparisons are the percentage of reduction in delay, relative to the 0% AVs. The delay data for AVs and CVs are depicted in Tables 5 and 6 respectively.

Table 5. *Percentage of Delay Reduction for AVs*

AVs market penetration rates	Demand to capacity ratio	
	0.6	**0.8**
5%	17.96	10.4
10%	25.6	17.1
15%	30.8	21.5
20%	34.1	27.2
25%	40.6	33.3
40%	54.4	45.4
60%	71.1	63.2
80%	84.1	79.1
100%	96.5	94.1

Table 6 *Percentage of Delay Reduction for CVs*

AVs market penetration rates	Demand to capacity ratio	
	0.6	**0.8**
5%	3.5	4.9
10%	9.3	9.6
15%	12.7	12.8
20%	16.95	16.5
25%	22.4	22.4
40%	33.2	32.3
60%	49.5	47.7
80%	59.7	61.3

According to Tables 5 and 6 the delay decreased (improved) as the market penetration rates of AVs increased. The delay reduction percentages for AVs at 0.6 demand to capacity ratio ranges from about 18% with 5% AVs to about 97%. The reductions for CVs range from 3.5% to about 60% at AVs percentage of 5% and 80%, respectively. At 0.8 demand to capacity ratio, the reduction percentages for AVs range from 10% with 5% AVs to about 95% with 100% AVs while the reduction for CVs ranges from 5% with 5% AVs to 62% with 80% AVs.

This reduction in delay resulted in a reduction in travel time that was observed in the previous section. However, the percentages of improvement for delay are much higher than travel time percentages because delay values are smaller in

magnitude, so any small improvement in delay time results in a significant percentage improvement in delay.

t-test

In this section, a test of hypotheses is conducted (using the t-test) to check that the variations of traffic performance measures are not random variations in the data, and that they are due to the difference between distributions. Two types of t-test were conducted; dependent and independent t-tests. Two hypotheses tests are formed and evaluated.

The Null hypothesis (H_0) assumes that there is no difference between the means of the two populations or scenarios (Devore et al. 2013).

$$H_0: \mu_1 = \mu_2$$

While the Alternative hypothesis (H_a) assumes that there a difference exist between the two means (Devore et al. 2013).

$$H_a: \mu_1 \neq \mu_2$$

Where:
μ_1: the mean of the first scenario.
μ_2: the mean of the second scenario.
Δ = the difference between means.

When conducting the t-test, two possible errors may occur. Type I error, which is rejecting H_0 when it is actually true and Type II error which is accepting H_0 when it is false.

The probability of making type I error is denoted by "α" and is called level of significance. In this test procedure $\alpha = 0.05$ will be used.

Dependent t-test

Dependent (paired) t-tests were carried out to compare the average speed of each market penetration rates scenario to determine if there is a statistical difference in average speed between consecutive scenarios or not. First the following equation was used to calculate t value.

$$t = \frac{\bar{d} - \Delta}{\frac{s_d}{\sqrt{n}}}, \qquad (1)$$

where,
n = number of pairs
$\bar{d}$ = the mean difference
Δ = the difference between means
s_d = standard deviation of the difference

Then P-value was determined from t curves with n-1 degree of freedom. Based on the P-value obtained the null hypothesis is accepted or rejected as follows:
if P-value $\leq \alpha$ reject H_0
if P-value $> \alpha$ accept H_0

- At 0.6 demand to capacity ratio

Table 7 shows the p-values and the decision of accepting or rejecting the null hypothesis.

Table 7. *t-test Results for Comparing Scenarios' Speeds at 0.6 Demand to Capacity Ratio*

Scenarios	P-value	Decision
0% and 5%	2.56E-04	reject H_0
5% and 10%	1.42E-04	reject H_0
10% and 15%	2.55E-03	reject H_0
15% and 20%	2.50E-04	reject H_0
20% and 25%	4.50E-04	reject H_0
25% and 40%	09.52E-06	reject H_0
40% and 60%	4.50E-05	reject H_0
60% and 80%	6.67E-08	reject H_0
80% and 100%	4.57E-07	reject H_0

According to Table 7, all p-values are significantly less than α (0.05). Therefore, the null hypothesis is rejected and there is a statistical difference between the average speeds of each scenario. This means that the average speed improved significantly with the increase of AVs market penetration rates from 0% to 100%.

- At 0.8 demand to capacity ratio

Table 8 contains the P-values at 0.8 demand to capacity ratio.

Table 8. *t-test Results for Comparing Scenarios' Speeds at 0.8 Demand to Capacity Ratio*

Scenarios	P-value	Decision
0% and 5%	3.71E-03	reject H_0
5% and 10%	2.32E-03	reject H_0
10% and 15%	1.75E-04	reject H_0
15% and 20%	3.45E-03	reject H_0
20% and 25%	5.73E-04	reject H_0
25% and 40%	1.32E-04	reject H_0
40% and 60%	1.66E-05	reject H_0
60% and 80%	8.59E-08	reject H_0
80% and 100%	1.62E-05	reject H_0

Table 8 shows that there is a significant difference between each market penetration rates average speeds at 0.8 demand to capacity ratio as all the P-values are much smaller than α so the null hypothesis is rejected similar to 0.6 case any change in AVs market penetration rates yields a significant difference in average speed.

Independent t-test

The independent (Pooled Variance) t-test was conducted to compare the means of the speed values of AVs and CVs in the same scenario (the same market penetration rate) to determine whether there is a significant difference between AVs and CVs speed values using the following equation:

$$t = \frac{\bar{x}_1 - \bar{x}_2}{\sqrt{\frac{{s_1}^2}{n_1} + \frac{{s_2}^2}{n_2}}} \quad (2)$$

where,
$\bar{x}_1$: mean of group1
$\bar{x}_2$: mean of group2
s_1 : sample variance of group1
s_2 : sample variance of group 2
n_1 : number of observations of group1
n_2 : number of observations of group 2

- At 0.6 demand to capacity ratio

Independent t-test was conducted between AVs and CVs average speeds, and P-values were calculated and summarized in Table 9.

Table 9. *t-test between CVs and AVs Speeds at 0.6 Demand to Capacity Ratio*

Scenarios	P-value	Decision
5%	1.9266E-08	reject H_0
10%	3.59779E-09	reject H_0
15%	1.98112E-08	reject H_0
20%	2.05817E-08	reject H_0
25%	5.01216E-09	reject H_0
40%	1.40731E-09	reject H_0
60%	3.17224E-12	reject H_0
80%	7.26973E-09	reject H_0

According to Table 9, there is a significant difference between AVs and CVs speed values at all market penetration rates as the congestion at this demand to capacity ratio is small, so AVs can travel freely with speeds significantly higher than CVs.

- At 0.8 demand to capacity ratio

The P-values at 0.8 demand to capacity ratio are obtained and shown in Table 10.

Table 10. *t-test between CVs and AVs Speeds at 0.8 Demand to Capacity Ratio*

Scenarios	P-value	Decision
5%	1.23986E-07	reject H_0
10%	8.15699E-08	reject H_0
15%	1.41604E-07	reject H_0
20%	5.60178E-08	reject H_0
25%	6.14618E-07	reject H_0
40%	2.82743E-08	reject H_0
60%	7.85416E-12	reject H_0
80%	4.085E-09	reject H_0

Similar to 0.6 case, there is a significant difference between the means of AVs and CVs speed values for the same reason that AVs travel much faster than CVs at low congestion.

Conclusions

Autonomous vehicles are the next generation vehicles that have drawn significant attention recently and it has become a major concern to major cities. As the use of AVs is an essential component for smart city. Dubai is planning to adopt this new technology as part of its transportation system's transformation process. However, the introduction of this technology is expected to have various impacts. These impacts should be studied in order to evaluate and maximize the benefits of these vehicles and minimize the risks and errors associated with them. The purpose of this research is to determine how the adoption of AVs can impact the traffic performance of Dubai's freeways.

The microsimulation software VISSIM was utilized to develop microsimulation model of a 10-km section of a major freeway in Dubai. The purpose of the simulation is to evaluate different scenarios that represent different market penetration rates s of AVs and different congestion levels. This study considered various market penetration rates s for AVs (0%, 5%, 10%, 15%, 20%, 25%, 40%, 60%, 80%, and 100%). It should be noted that the 0% was used as a benchmark for comparison purposes. Different traffic congestion levers were evaluated by considering two demand to capacity ratios of 0.6 and 0.8, representing undersaturated conditions. In summary, the results showed that:

1) Increasing AVs fleet percentage yields an increase in average speed and a decrease in travel time and delay, as CVs are replaced with AVs. This can be attributed to the fact that AVs strictly keep a constant speed without variation and travel with a smaller THW. Therefore, this provides smooth and uniform traffic flow in the network.

2) The performance improvement increases as the demand to capacity ratio increases, which is consistent with (Aria et al. 2016) findings that positive effects of AVs are highlighted when the congestion increases and when the traffic flow becomes denser.
3) The highest improvements were achieved at 0.8 demand to capacity ratio with 100% AVs. The average speed increased by about 15%, the travel time decreased by about 12%. However, the maximum reduction in delay was achieved at 0.6 demand to capacity ratio (around 97%) which is slightly higher than the delay reduction at 0.8 demand to capacity ratio (about 94%).
4) The comparison between scenarios, using dependent t-test, revealed that any change in AVs market penetration rates yields a significant difference in the traffic performance, at 0.6 and 0.8 demand to capacity ratios.
5) By comparing the mean of the average speeds of AVs and CVs, using independent t-test, it was noted that there is a significant difference between AVs and CVs speed values at all market penetration rates for both 0.6 and 0.8 demand to capacity ratios.

This research considered only the impacts of AVs on Freeway performance without any considerations of changing the lane width or changing any of the road characteristics. Therefore, future work can consider the following:

- Implementing the procedure followed in this paper for over saturated traffic conditions to achieve results that cover all possible real-life situations, especially during peak hours.
- Safety on both Freeways and intersections
- AVs' system failure and how they will perform in this case
- Performance of AVs on arterial streets' networks dealing with signalized junctions and roundabouts

References

Aria E, Olstam J, Schwietering C (2016) Investigation of automated vehicle effects on driver's behavior and traffic performance. *Transportation Research Procedia* 15: 761-770.

Arnaout G, Bowling S (2011) Towards reducing traffic congestion using cooperative adaptive cruise control on a freeway with a ramp. *Journal of Industrial Engineering and Management* 4(4): 699-717.

Bierstedt J, Gooze A, Gray C, Peterman J, Raykin L, Walters J (2014) Effects of next-generation vehicles on travel demand and highway capacity. *FP Think Working Group* 8.

Bocca A, Baek D (2020) Automated driving systems: key advantages, limitations and risks. *IEEE Conference Publication*. Retrieved from: https://bit.ly/394dnYp. [Accessed 20 February 2020].

Das S, Sekar A, Chen R, Kim H, Wallington T, Williams E (2017) Impacts of autonomous vehicles on consumers time-use patterns. *Challenges* 8(2).

Devore J, Farnum N, Doi J (2013) *Applied statistics for engineers and scientists*. 3rd Edition. Belmont, Calif: Duxbury.

Fagnant J, Kockelman K (2015) Preparing a nation for autonomous vehicles: opportunities, barriers and policy recommendations. *Transportation Research Part A* 77(Jul): 167-181.

Hao K (2017) *At least 47 cities around the world are piloting self-driving cars*. Retrieved from: https://bit.ly/2T0O5EW. [Accessed 20 February 2020].

Ioannou A, Chien C (1993) Autonomous intelligent cruise control. IEEE Transactions on Vehicular Technology 42(4): 657-672.

Kesting A, Treiber M, Schönhof M, Kranke F, Helbing D (2007) Jam-avoiding adaptive cruise control (acc) and its impact on traffic dynamics. *Traffic and Granular Flow* 5(Feb): 633-643.

Litman T (2014) Autonomous vehicle implementation predictions: implications for transport planning. *Transportation Research Board Annual Meeting*, 36-42.

Ngan V, Sayed T, Abdelfatah A (2004) Impacts of various parameters on transit signal priority effectiveness. *Journal of Public Transportation* 7(3): 71-93.

NHTSA (2018) *Automated vehicles for safety*. Retrieved from: https://www.nhtsa.gov/technology-innovation/automated-vehicles-safety. [Accessed 20 February 2020].

PTV Group (2017) PTV VISSIM & connected autonomous vehicles. *VISSIM User Manual*.

Rafael S, Correia L, Lopes D, Bandeira J, Coelho M, Andeade M, et al. (2020) Autonomous vehicles opportunities for cities air quality. *Science of the Total Environment* 712(Apr).

SAE (2018) Taxonomy and definitions for terms related to driving automation systems for on-road motor vehicles (J3016 ground vehicle standard) - SAE mobilus. *Saemobilus.sae.org, 2020*. Retrieved from: https://saemobilus.sae.org/content/j3016_201806. [Accessed 20 February 2020].

Simon K, Alson J, Snapp L, and Hula A (2015) Can Transportation Emission Reductions Be Achieved Autonomously? *Environ. Sci. Technol*., vol. 49, no. 24, pp. 13910–13911.

Strand N, Nilsson J, Karlsson I, Nilsson L, (2014) Semi-automated versus highly automated driving in critical situations caused by automation failures. *Transportation Research Part F: Traffic Psychology and Behaviour* 27(PB): 218-228.

Tientrakool P, Ho C, Maxemchuk F (2011) Highway capacity benefits from using vehicle-to-vehicle communication and sensors for collision avoidance. *IEEE Vehicular Technology Conference*, 0-4.

WAM (2016) *Mohammed bin Rashid approves Dubai autonomous transportation strategy final*. Retrieved from: http://wam.ae/en/details/1395294678474. [Accessed 20 February 2020].

World Economic Forum (2018) Reshaping urban mobility with autonomous vehicles lessons from the city of Boston. Retrieved from: http://www3.weforum.org/docs/WEF_Reshaping_Urban_Mobility_with_Autonomous_Vehicles_2018.pdf. [Accessed: 29 February 2020].

Athens Journal of Technology & Engineering 2020, 7(2): 133-156
https://doi.org/10.30958/ajte.7-2-4

Alternative Fastening Mechanism for Shear Connectors with Cold-Formed Steel Shapes Involved in Composite Sections

By Xavier Fernando Hurtado Amézquita[*] & Maritzabel Molina Herrera[±]

Over the past few decades, the use of steel-concrete composite sections has increased globally, to take advantage of compression strength in concrete and tensile strength in steel, ensuring its connection by employing stress transfer elements denominated shear connectors. The main connection systems, endorsed by the current design codes, are used by applying welding as a fastening mechanism to fix connectors and any alternative system must be validated through an experimental program. However, this thermal procedure produces a concentration of residual stresses during the cooling process and the risk of perforation in Cold-Formed Steel sections (CFS), affecting the behavior efficiency of the composite sections. In this research, self-drilling screws are proposed as an alternative mechanical system for connectors fastening. The system efficiency was initially compared to the powder-actuated nails mechanism, validating their advantages of installation and structural behavior. An experimental program was carried out to validate the capacity and performance of the system, through screw shear tests and full-scale beam tests. Therefore, it was possible to characterize the local behavior in the fastening mechanism and the overall behavior in the composite system. According to results, self-drilling screws are a viable alternative to use as a fastening mechanism in shear connectors for CFS and concrete composite sections. The composite system developed full capacity, even in inelastic range, without disconnection between materials. Self-drilling screws remained fixed on steel shapes without mechanical damage, allowing greater deformations than displacements under service conditions.

Keywords: *Composite sections, Shear connector, Cold-formed steel, Fastening mechanism, Self-drilling screws*

Introduction

Over the past few decades, the use of steel-concrete *composite sections* has increased globally. The basic principle of joining these two materials is to take advantage of their mechanical properties. In this way, steel sections can be loaded to high compression force, but efficiency is reduced in slender members due to their potential instability induced by lateral buckling, torsional buckling and/or local buckling, mainly in open sections (Valencia 2010). Therefore, optimization

[*]Assistant Professor, Department of Civil Engineering, La Salle University, Colombia.
[±]Associate Professor, National University of Colombia, Colombia.

of the composite section is based on the concrete slab to withstand compression stresses and on the steel shape to withstand tensile stresses.

Assembly of composite sections implies the attachment of stress transfer elements between materials, called *shear connectors*. These components can control possible uplifts and relative displacements on the connection interface. Moreover, the strain state is also modified due to the inclusion of shear connectors, thus a two-materials system becomes a composite system.

This system was initially proposed for bridges, and due to its good structural performance, its uses were expanded to flooring systems in buildings (Lakkavalli and Liu 2006).

Recently, within technologies with better structural efficiency, Cold-Formed Steel (CFS) sections have increased their structural applications in medium and small buildings (Hossain 2005), becoming a competitive alternative concerning Hot-Rolled Steel (HRS) sections, which are heavier but commonly used in conventional infrastructure (Hancock 2003).

The main advantages of CFS are versatility in the generation of different cross-sections, the possibility of using it in long spans, ease in industrial production, high strength-to-weight ratio and speed in packaging, transport and assembly (Yu and LaBooube 2010). Moreover, these sections are considered as an alternative to build sustainable structures in "green" construction (Alhajri et al. 2016, Irwan and Hanizah 2009, Lawan et al. 2015).

Currently, design codes, such as AISC 360, AISI S-100, NBR8800, AS/NZ 4600, S136, Eurocode4, JSCE/09, involve welding as a conventional methodology to fix studs, channels or perfobond ribs as the regulated shear connectors (AISI 2016, AISC 2016, ABNT 2008, AS/NZ 2005, CSA 2007, ECS 2004, JSCE 2009). This thermal process generates uncertainty in the structural behavior of the composite systems because it induces local residual stresses in steel sections and connectors, reducing both its mechanical capacity and efficiency. Moreover, in CFS, electrodes can perforate steel shape plates (Figure 1), due to the high temperature and limited thickness of the steel section (Erazo and Molina 2017).

Figure 1. *Damages in CFS Steel Plates Caused by Welding Process*

Source: Erazo and Molina 2017.

Therefore, knowing the disadvantages of welding, it is convenient to develop design methodologies, incorporating efficient alternative mechanisms for the mechanical fastening of shear connectors (Merryfield et al. 2016).

In this research, self-drilling screws are validated as an alternative mechanical system to fasten connectors. An experimental program was carried out in order to quantify the failure capacity of the system, involving screw shear tests and full-scale beam tests. The advantages of the proposed system were confirmed according to the mechanical adhesion and structural behavior showed.

Background

Different alternative mechanical fastening systems in CFS sections have been studied, to ensure an adequate system connection, regardless of the welding process.

Hanaor (2000) evaluated a bolts and nuts system and expansion anchor bolts in hardened concrete as shear connectors, through experimental push-out tests and full-scale beam tests. Displacements and rotations were observed in the bolts due to adjustments and clearance of the bolt predrilled holes, inducing early sliding between materials. Moreover, bolts presented ductile behavior, allowing large deflections in the composite systems.

Using bolted screws as transfer elements, Queiroz et al. (2010) evidenced local deformations in CFS sections, induced by stress concentration due to the limited thickness, reducing the capacity in the composite systems.

Figure 2. *Local Buckling in CFS-Concrete Composite Sections* a) *Push-Out Test* b) *Full Scale Beam Test*

a) b)

Source: Lawan et al. 2015.

Complete studies of bolted shear connectors were developed by Lawan et al. (2015), Lawan and Tahir (2015) and Tahir et al. (2016a, b), which involved the effects of bolt size and spacing between connectors in the behavior of CFS-concrete composite systems. Experimental programs included full-scale bending tests and push-out tests. According to the whole push-out results, the greater diameter size the better performance in the composite system is, but the failure

mode depends on this factor. Therefore, M12 bolts showed shear in screws, and greater sizes presented longitudinal and transversal cracks in concrete, although some specimens were not fully characterized due to the local buckling in the steel shape (Figure 2a). Bending tests also showed ductile behavior, as well as in the results of Hanaor (2000), allowing displacements up to service limit conditions. The main failure mode was transverse cracks beneath the concrete slab at load application points, accompanied by local buckling in steel shape (Figure 2b). In this way, the thickness plate becomes a relevant factor in the behavior of CFS-concrete composite systems.

Fontana and Bartschi (2002) applied powder-actuated fastening systems to fix alternative rib shear connectors made by cutting and folding CFS plates. Although the system was efficient, failure was generated mainly by connector bearing in push-out tests, due to the thickness plate, disassembling the composite systems.

Derlatka et al. (2019) also studied the effectiveness of powder-actuated nails in top-hat shear connectors, initially proposed by Lawson et al. (2001). In general, push-out test results showed ductile behavior in the composite system, being more effective in the shortest connectors (60 mm). Most of the failure modes were associated with rotation and cutting in steel nails, and tearing in shear connectors, with previous excessive deformations, decoupling the composite system, without evidence of damages in the concrete slabs (Figure 3). Currently, this mechanism is applied in commercial systems such as HILTI® and TECNARIA®.[1] These companies specify those systems must be used on plates of more than 6 mm thickness to avoid perforations, due to the force on fired nails. However, those products require a special tool to make this installation an efficient procedure.

Figure 3. *Typical Failure Modes in Powder-Actuated Fastening Systems* a) *Tearing in Rib Shear Connector* b) *Rotations and Decoupling of Composite System in Push-Out Test*

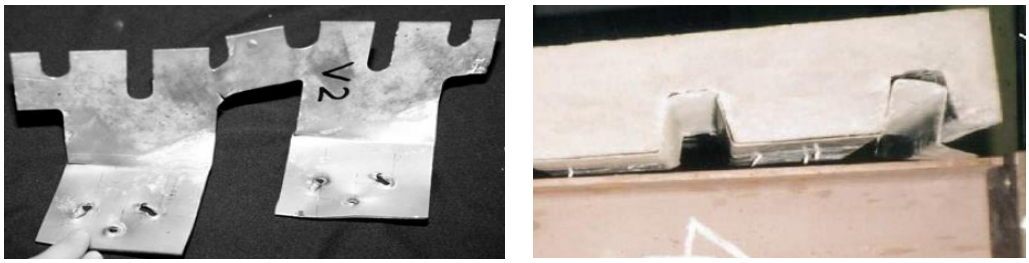

a) b)

Source: Fontana and Bärtschi 2002, Derlatka et al. 2019.

Lakkavalli and Liu (2006), Merryfield et al. (2016) and Kyvelou et al. (2017, 2018) used self-drilling screws as shear connectors in full-scale bending tests for CFS composite beams. Study factors involved in the researches were connectors spacing and comparison to other types of transfer elements such as bent-up tabs, bolt connectors and puddle welding. They found that the better system performance the shorter spacing is, developing higher bearing loads. The behavior was

[1]https://www.hilti.com.co, https://www.tecnaria.com.

characterized by high inelastic deformations, inducing bending and shear in screws, sliding of concrete slab on the steel beam and local buckling in steel shape (Figure 4). Self-drilling screws presented limited capacity, compared to welded systems; thus, it was necessary to install many connectors, becoming a non-practical and expensive system.

Figure 4. *Failure Modes in Self-Drilling Shear Connectors* a) *Bending in Screws* b) *Shear in Screws* c) *Local Buckling in Steel Shape*

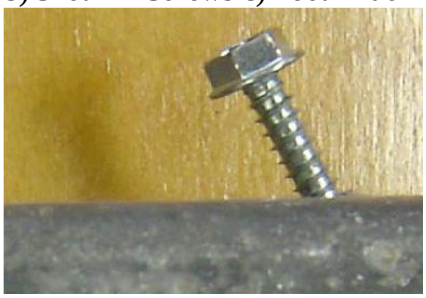

a)

b)

c)

Source: Lakkavalli et al. 2006, Merryfield et al. 2016.

All these types of shear connectors presented an adequate connection and stress transfer between materials. In contrast, bolted joints have not been technically endorsed yet, due to the lack of standardization of tests and results.

Methodology

Materials

Experimental tests involved two types of concrete compressive strength to build 100 mm thickness slabs: 21 MPa and 28 MPa.

The mechanical characteristics of steel differed according to each type of element used:

- Shear connectors: ASTM A424 - Type II, in 1.9 mm thickness.
- Screw shear test samples: ASTM A424 - Type II, in 1.5 mm and 2.0 mm thicknesses.
- Steel beams (C220x80x2.5): ASTM A1011, in 2 m and 4 m length, and 2.5 mm thickness.
- Self-drilling screws: ASTM A449 - Type I, in 6 mm diameter.

- Fired nails: HRC 57.5 (ASTM A276 440C), in 3 mm diameter.

Table 1 summarizes the main nominal mechanical properties of the materials.

Table 1. *Nominal Properties of the Materials*

Structural Component	Concrete		Steel		
	Compressive Strength (f´c)	Modulus of Elasticity (Ec)	Yield Strength (fy)	Ultimate Tensile Strength (fu)	Modulus of Elasticity (Es)
	(MPa)	(MPa)	(MPa)	(MPa)	(MPa)
Concrete Slab	21	21,736			
	28	25,098			
Steel Beam			340	410	200,000
Shear Connectors			240	345	200,000
Self-Drilling Screws			644	840	200,000
Fired nails			448	758	200,000

Source: Authors.

Experimental Program

Three experimental tests were programmed to characterize the alternative fastening mechanism: Fastening system comparison, screw shear test and full-scale beam test. All of them allowed identifying and qualifying the behavior of the system under service conditions, both qualitatively and quantitatively, acting in composite sections.

Fastening System Comparison

In this research, powder-actuated nails and self-drilling screw systems were selected for preliminary evaluation, which do not require sophisticated and specialized machines, compared to welded systems, increasing ease of installation and reducing operating costs in the construction field.

The efficiency of the systems was evaluated through a fastening experimental test, in two C220x80x2.3 mm back to back shapes (Figure 5a), with steel yield strength (fy) equal to 340 MPa. Figure 5 shows the geometrical characteristics of the systems to be compared, as well as the installation procedure required in each case.

Figure 5. *Fastening Mechanisms Compared* a) *Configuration of Test (Units in mm)* b) *Installation of Powder-Actuated Nails* c) *Geometric Detail of Fired Nails* d) *Installation of Self-Drilling Screws* e) *Geometric Detail of Self-Drilling Screws*

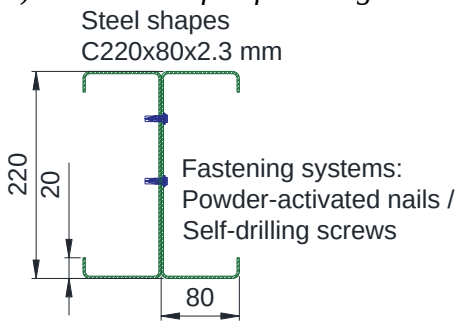

a)

b) c) d) e)

Source: Authors.

Screw Shear Test

The mechanical strength of the connection was evaluated by experimental screw shear tests. The axial tensile load was applied by Universal Testing Machine on steel plate samples, which were connected by self-drilling screws. The configuration of specimens is presented in Figure 6, and all the arrangements are defined in Table 2, where the thickness effect was validated in the failure capacity of the system. The test setup is shown in Figure 7.

Figure 6. *Configuration of Test Samples in Screw Shear Test (Units in mm)*

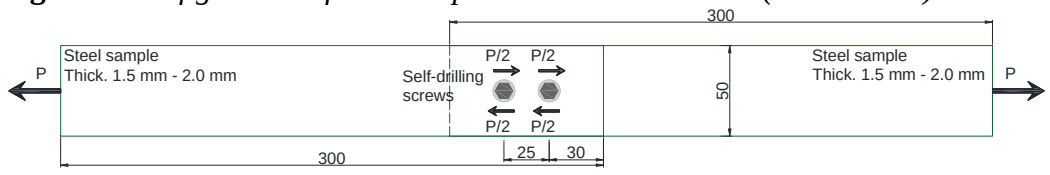

Source: Authors.

Figure 7. *Screw Shear Test Setup* a) *Front View* b) *Side View*

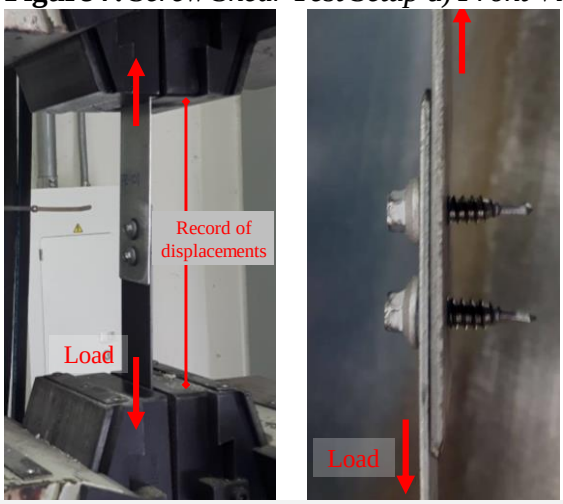

a) b)

Source: Authors.

According to the AISI S100, bolted connections must be designed for bearing failure in steel plates and shear in screws. Therefore, the ultimate limit states were previously reviewed, obtaining the nominal loads presented in Table 2.

Table 2. *Arrangement of Specimens in Screw Shear Test*

No.	Upper plate		Lower plate		Screws		Nominal resistance	
	Thickness	Yield Strength (fy)	Thickness	Yield Strength (fy)	Quantity and Diameter	Ultimate Tensile Strength (fu)	Nominal Failure Load	Type of nominal failure
	(mm)	(MPa)	(mm)	(MPa)	(mm)	(MPa)	(kN)	
PR-01	1.5	240	2.0	240	2 x 6	324	13.04	Plate bearing
PR-02/04	1.5	240	1.5	240	2 x 6	324	13.04	Plate bearing
PR-03/05	2.0	240	2.0	240	2 x 6	324	18.32	Shear screws

Source: Authors

Because metal drilling and molding work induce stress concentrations and temperature rise, a thermal scan was performed during the manufacturing process of the test specimens, using a FLIR E40 thermal imaging camera. It was found that the final temperature is not as relevant as in the welding processes, remaining below 38 °C due to the manual handling of parts. Figure 8 shows the thermal image taken from the scanner test.

Figure 8. *Installation Process of Self-Drilling Screws. Comparison between Real View and Thermal Image, Using a FLIR E40 Thermal Imaging Camera*

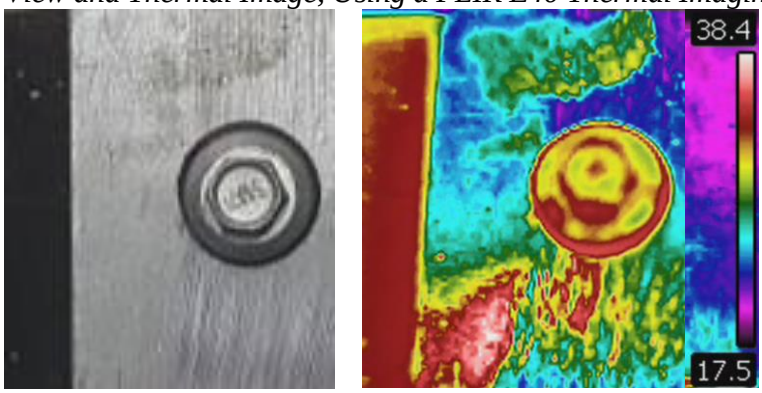

Source: Authors.

Full-Scale Beam Test

Bending tests on composite beams allow characterizing the global behavior of the fastening system during the service conditions, acting as a link between shear connectors and the steel section. In this research, 4-point-load experimental bending tests were carried out on simply supported specimens, assembled by a double C220x80x2.5 mm box section with a concrete slab (Figure 9a). Moreover, the ends of the steel beam were filled with concrete, to prevent local buckling, due to reaction forces. The setup of experimental tests is presented in Figure 9.

Figure 9. *Setup of Full-Scale Beam Tests* a) *Cross Section* b) *Four-Point Bending Test Setup* c) *General Arrangement of Shear Connectors. Top View (Units in mm)*

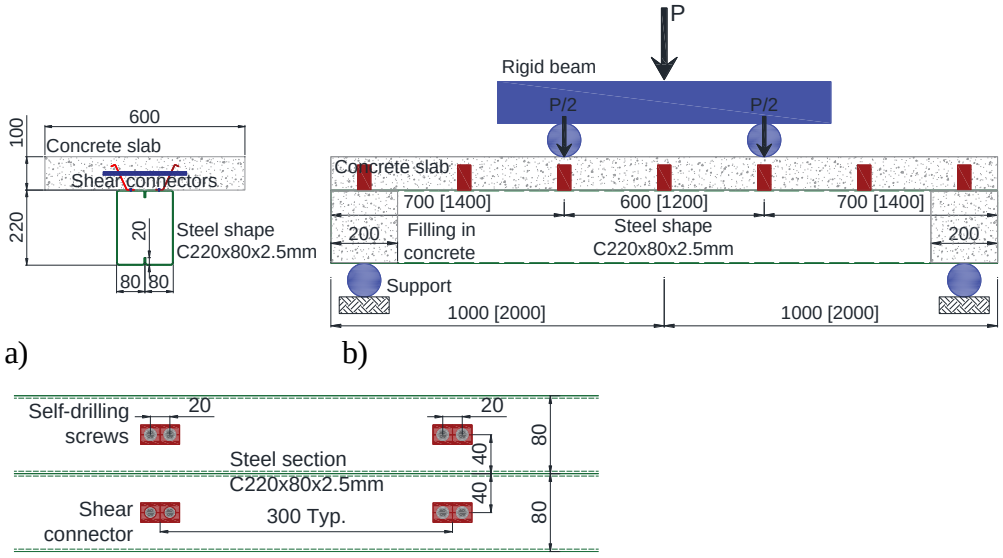

Source: Authors.

The load was applied through a hydraulic jack, with a capacity of 500 kN, and transmitted through rails to two-point loads on the concrete slab. The displacement control was employed for the monotonic test (Figure 10).

Figure 10. *Full-Scale Beam Test Setup*

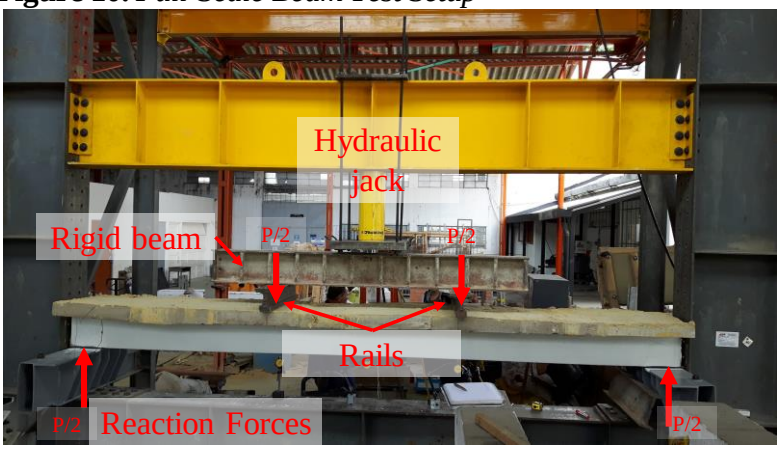

Source: Authors.

Beams deflections were recorded using dial indicators, located at thirds of the length, to verify symmetry in behavior. Additionally, strain gauges were attached to the steel sidewall to evaluate strain status throughout the tests (Figure 11).

The deformation states and the final deflection of the system were evaluated, as well as the maximum failure loads and failure modes. The configuration of specimens is defined in Table 3.

Figure 11. *Experimental Test Instrumentation*

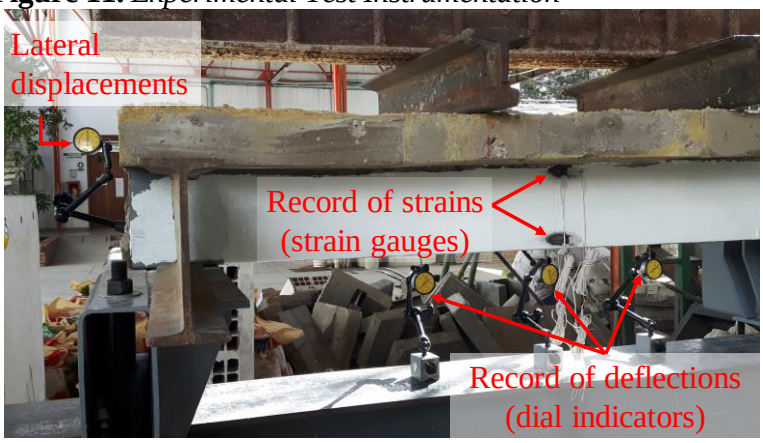

Source: Authors.

Table 3. *Configuration of Specimens in Full-Scale Beam Test*

No	Concrete Slab		Steel Section			Shear Connectors	
	Compressive Strength (f´c)	Thickness	Yield Strength (fy)	Thickness	Length	Thickness	Yield Strength (fy)
	(MPa)	(mm)	(MPa)	(mm)	(m)	(mm)	(MPa)
21-2	21.0	100	340	2.5	2.0	1.9	240
21-4	21.0	100	340	2.5	4.0	1.9	240
28-2	28.0	100	340	2.5	2.0	1.9	240
28-4	28.0	100	340	2.5	4.0	1.9	240

Source: Authors.

An analytical study was conducted, which allowed predicting the nominal failure loads.

According to AISC-10 and Eurocode4 recommendations, this type of non-compact steel shapes should be analyzed under elastic methods, due to its susceptibility to local buckling in steel plates because of the limited thickness. This condition avoids developing the plastic capacity on the entire steel section before the failure of the composite system. Table 4 shows the analysis of nominal loads, applying Strain Compatibility Method (SCM), by transforming a concrete cross-section into an equivalent steel section, to study only one material.

Although the plastic capacity of the steel cannot be developed, Table 4 also includes plastic analysis applying the Plastic Stress Distribution Method (PSDM), in order to know a possible range of workloads before failure.

The full composite action is considered in both analyses. Figure 12a includes stresses distribution in *SCM* and Figure 12b *PDSM* analyses.

Figure 12. *Stress State in Composite Sections* a) *Elastic Analysis* b) *Plastic Analysis (Units in mm)*

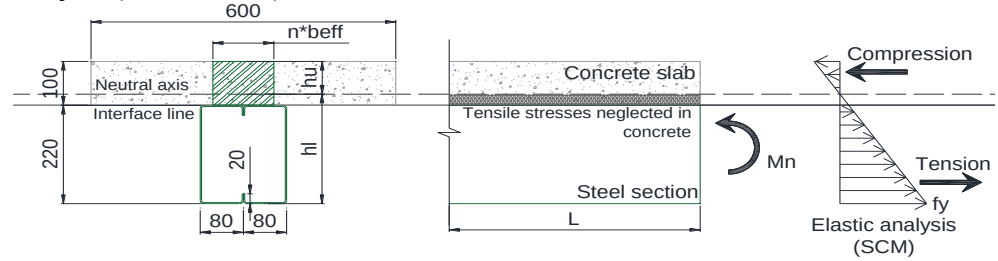

a)

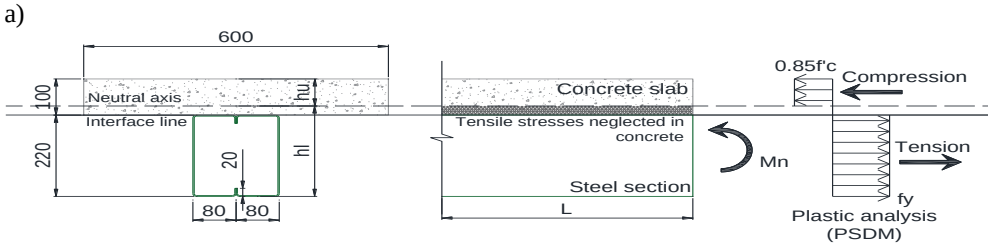

b)

Source: Authors.

Table 4. *Nominal Loads in Composite Sections*

Characteristics of the composite systems		Elastic analysis *Strain-Compatibility Method (SCM)*		Plastic analysis *Plastic Stress Distribution Method (PSDM)*	
Modular ratio	n	0.109	0.125	---	---
Upper distance neutral axis	hu (mm)	87.50	83.53	63.37	47.53
Lower distance neutral axis	hl (mm)	232.50	236.47	256.63	272.47
Nominal resistant moment	Mn (kN*m)	65.19	67.12	121.03	126.41
Nominal resistant Load 2 m	Pn (kN)	186.25	191.78	345.8	361.16
Nominal resistant Load 4 m	Pn (kN)	93.12	95.89	172.9	180.58

Source: Authors.

Results and Discussion

Fastening System Comparison

According to experimental results, both the powder-actuated nails and the self-drilling screws systems perforated the plates and connected the steel shapes. The final state of the fastening elements is shown in Figures 13 and 14.

Figure 13. *Fastening Systems Installed on Test Specimens (Top View)*

Source: Authors.

During the installation process, two relevant disadvantages were evidenced in powder-actuated nails systems:

- The fired nails had plastic covers, which remained after installation. This cover is necessary to direct the shots but restricts the useful length during the service conditions.
- Friction and adhesion with the steel shape were not enough due to the flat shank geometry of the fired nails. Therefore, the link between elements is lost quickly, even under low external loads.

Physical differences between the final state of fastening systems are evidenced in Figure 14. Thus, the limited capacity of the nail lengths becomes relevant.

Figure 14. *Fastening Systems Installed on Test Specimens* a) *Bottom View* b) *Front View*

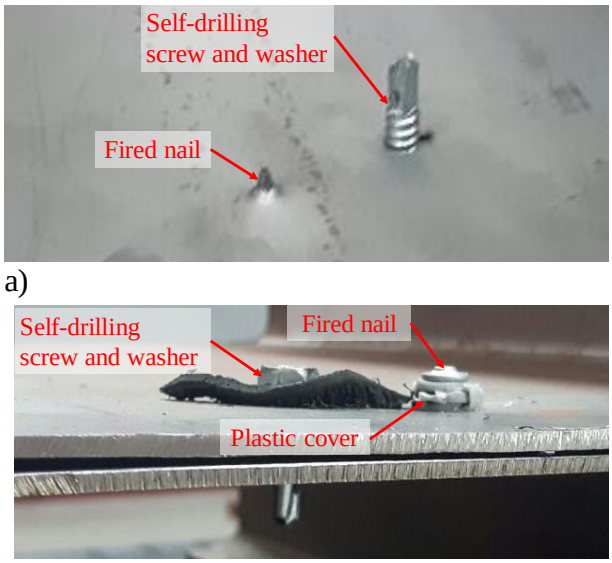

a)

b)

Source: Authors.

In contrast, the self-drilling screws system was an efficient fixing mechanism, ensuring the integrity of the assembled elements, despite the thickness restriction. Moreover, specialized tools are not required during the installation process, which makes it an easy system to be implemented on the field, without generating additional operating costs and avoiding the impacts presented by welding processes.

Therefore, guaranteeing the advantages of installation, self-drilling screws were used in the other characterization tests.

Screw Shear Test

Experimental screw shear tests were carried out according to the configuration presented in Table 2. Load and slip data were recorded during the test for all the specimens. Curves are presented in Figure 15, including the ultimate nominal limit states as horizontal lines.

Figure 15. *Load-Slip Curves for Experimental Screw Shear Test*

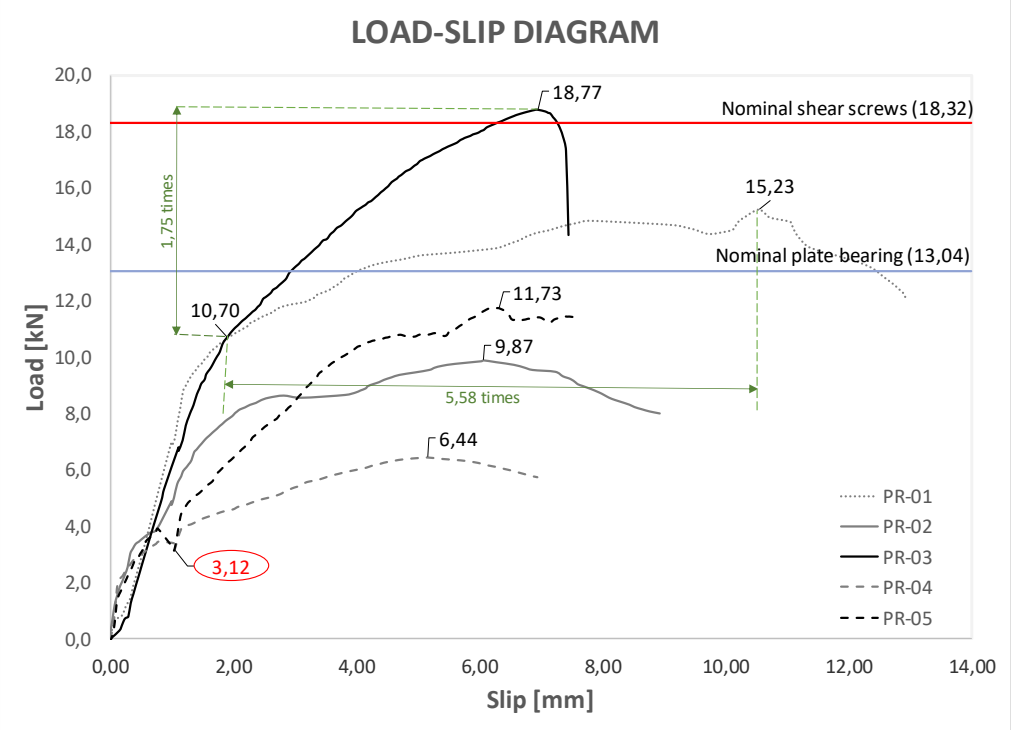

Source: Authors.

According to results, the 2.0 mm-thickness plate specimens, even in samples with combined thickness, exhibited a more stable behavior than 1.5 mm-thickness, reaching ultimate loads greater than nominal values: 1.02 times in PR-03 and 1.17 times in PR-01. Both specimens presented a similar elastic path before the initial damages in plates. Then, depending on the thicknesses, PR-03 showed a maximum failure load of 1.75 times the elastic load and PR-01 developed more inelastic displacements (5.58 times the elastic displacement) due to the deformability of the system.

The PR-02 and PR-04 (1.5 mm-thickness) could not reach the nominal plate bearing, which was obtained according to the AISI S100 formulation (Table 2). Therefore, it is relevant to review the applicability of the design formulation in plate thicknesses of less than 2.0 mm.

Although the PR-05 was 2.0 mm-thickness, it had an early instability due to machine handling, causing deterioration in the system capacity. A similar situation occurred in the PR-04, thus these samples were not taken into account within the representative information.

The failure modes presented in the experimental tests are shown in Figure 16.

Fragile failure was induced by shearing in screws, mainly in specimens PR-03 and PR-05, as shown in Figure 16a. The maximum inelastic displacements were limited to less than 7.5 mm, which additionally induced small tearing around the perforation area.

Screw tilting and plate separation failure were characterized by loss of adhesion in the system, evidenced in PR-02 and PR-04 specimens, as presented in

Figure 16b. The main resistant force was given by contact locking of screws thread on plates. Total system displacements increased, reaching 9.0 mm.

Specimen PR-01 failed due to tension on the net section in the thinnest plate, through one of the joint perforations and a small tearing in the other (Figure 16c). As in PR-02 and PR-04 specimens, screws were not affected in this system. Final displacements reached 13.0 mm.

Figure 16. *Failure Modes Presented in the Screw Shear Test* a) *Failure due to Screw Shear* b) *Failure due to Screw Tilting and Plate Separation* c) *Failure due to Tension on the Net Section in Plate*

a) b) c)

Source: Authors.

Therefore, it is concluded that the self-drilling fastening system allows guaranteeing elements fixing. On plates with thicknesses greater than 2.0 mm, the predominant failure mode is screws shearing. In plates of smaller thicknesses, the bonding capacity is limited by plate bearing. In configurations with combined thickness, the final resistance is governed by tension on the net section in the thinnest plate.

In terms of maximum displacement, according to results presented in Figure 15, it can be concluded that the greatest ductility is presented in joints with a thickness of less than 2.0 mm, in both combined thickness systems, or with the same thickness.

Full-Scale Beam Test

Different arrangements were considered in the experimental bending test, involving the compressive strength of concrete and beam length (Table 3), in order to evaluate the fastening mechanism under real composite systems. The final condition of the specimens is shown in Figure 17, where the baseline is included to contrast the degree of deformation, showing large displacements and exceeding widely the elastic behavior of the systems (more than 2.5 times for 2 m-long beams and more than 1.7 times for 4 m-long beams).

Figure 17. *Final Condition of Specimens in Full-Scale Beam Test* a) *2 m-Long Beams* b) *4 m-Long Beams*

a)

b)

Source: Authors.

The 2 m-long beams showed elastic and maximum deflections between 250% and 400% in 21 MPa and 28 MPa strength concrete, respectively. Regarding 4 m-long beams, ratios were around 174%, showing lower inelastic capacity than the previous ones.

Table 5 summarizes the elastic and maximum deflections and loads of the tests.

Table 5. *Summary of the Representative Loads and Deflections in Full-Scale Beam Test*

Concrete strength	Beam length	Parameter	Elastic	Maximum	Ratio Max./Elas.
21 MPa	2 m	Load (kN)	206.01	251.43	1.22
		Deflection (mm)	10.11	25.26	2.50
	4 m	Load (kN)	127.53	164.32	1.29
		Deflection (mm)	32.32	56.33	1.74
28 MPa	2 m	Load (kN)	166.77	268.40	1.61
		Deflection (mm)	7.93	32.04	4.04
	4 m	Load (kN)	117.72	150.49	1.28
		Deflection (mm)	29.94	51.69	1.73

Source: Authors.

As shown in Figure 11, test instrumentation allowed to record vertical and longitudinal displacements. Then, deflection curves are presented in Figure 18. Lengths of the beams were normalized as a percentage of the total length. The figure includes displacements at midspan and thirds in length. Additionally, baselines of the service limit state were included, in order to compare the final condition of specimens. It can be observed that the behavior of the composite sections remains in the elastic range under the service conditions, regardless of the compressive strength of concrete, which becomes a relevant factor under subsequent load levels (Figures 18 and 19).

Figure 18. *Deflection Curves for Full-Scale Beam Test*

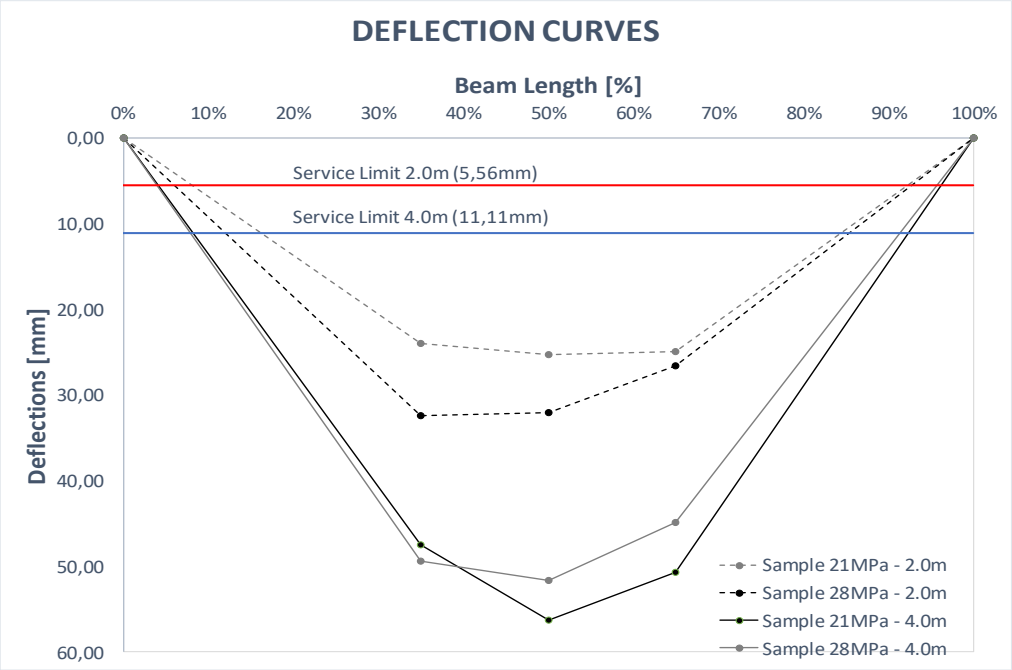

Source: Authors.

Based on the behavior of the curves (Figure 18), the maximum specimen deformations exceed around 5 times the limits for service condition in both lengths, as presented in Table 6.

Table 6. *Deflection Results for Full-Scale Beam Test*

No.	Maximum deflection in experimental test (Δmax.)	Allowable deflection under service condition L/360 (Δallow.)	Ratio
			Δmax /Δadm
	(mm)	(mm)	
21-2	25.26	5.56	4.54
21-4	56.33	11.11	5.07
28-2	32.04	5.56	5.76
28-4	51.69	11.11	4.65

Source: Authors.

Figure 19 shows Load-Deflection curves in 2 m-long beams and 4 m-long beams. Nominal elastic and plastic limits are included as the expected range of structural behavior, as well as service limits.

Figure 19. *Load-Deflection Curves for Experimental Full-Scale Beam Test*

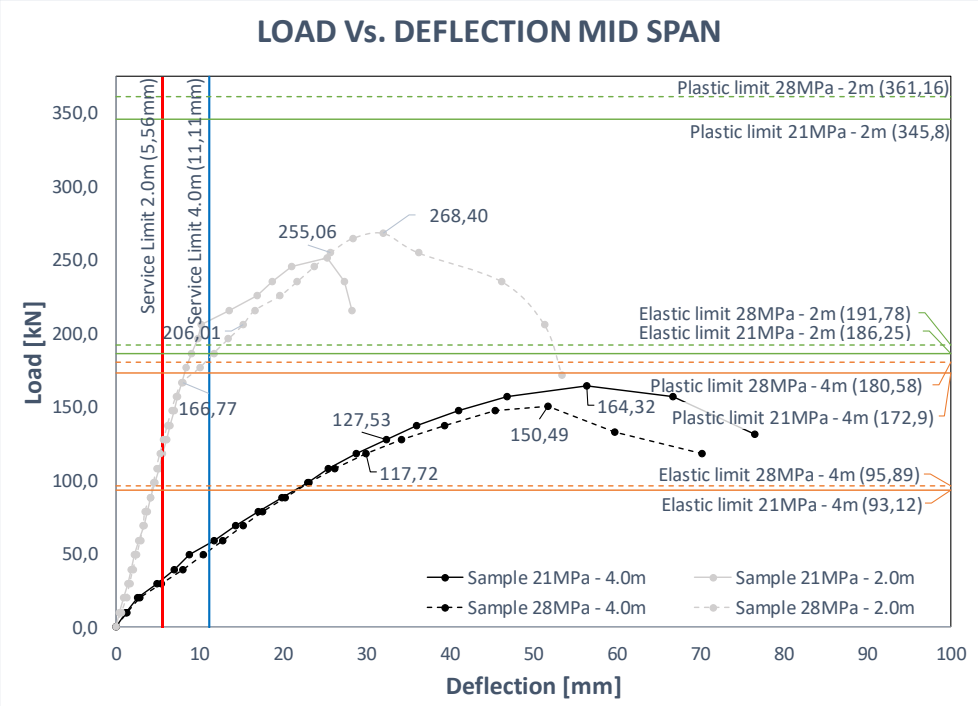

Source: Authors.

As shown in Figure 19, on the one hand, 4 m-long beams showed a behavior close to the nominal plastic load capacity of the composite section, 95% in 21 MPa concrete (black continuous line) and 83% in 28 MPa concrete (black dotted line). Furthermore, the elastic loads, included in Table 5, exceeded the nominal elastic limits, 1.37 times and 1.22 times in 21 MPa and 28 MPa, respectively. Deflections at the maximum loads evidenced 1.09 times greater values in 21 MPa concrete than in 28 MPa concrete.

On the other hand, the maximum loads of the 2 m-long beams present intermediate values between nominal plastic and elastic conditions (grey lines), reaching around 74% of the nominal plastic load. The elastic loads are around ±10% of the predicted nominal values. The deflection at the maximum loads was 1.25 greater in 28 MPa specimens than in the ones of 21 MPa.

The widest differences in elastic deflections were around 25.0 mm between specimens of the same length, found in 2 m-length beams (grey lines). In the longest specimens, the difference is lower than 3.0 mm.

Once elastic behavior is exceeded, cracking and fracture are induced in the concrete slab, mainly beneath the load application point, as shown in Figure 20. Due to asymmetry in the final condition of deflections (Figure 18), the cracks in the concrete slab presented different patterns.

Figure 20. *Concrete Slab Fracture in Full-Scale Beam Test* a) *General View* b) *Detailed View*

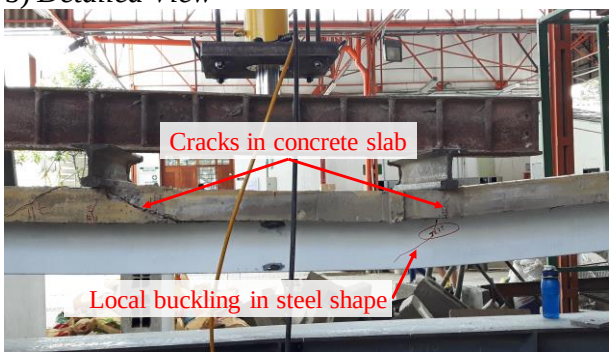

a)

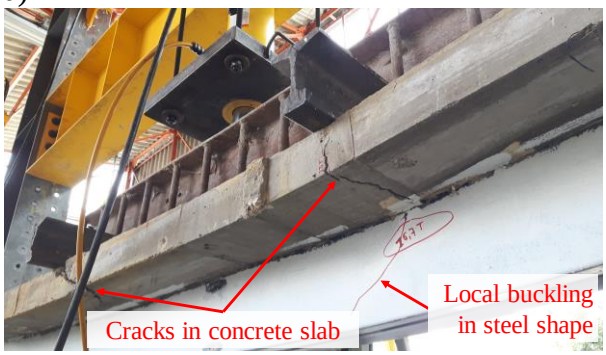

b)

Source: Authors.

Similarly, in the steel section, local buckling is generated due to an increase in the load. Displacements of the steel plates outside the load plane were produced, as shown in Figure 21.

Figure 21. *Local Buckling in Steel Shape in Full-Scale Beam Test* a) *General View* b) *Lateral Plate Detailing*

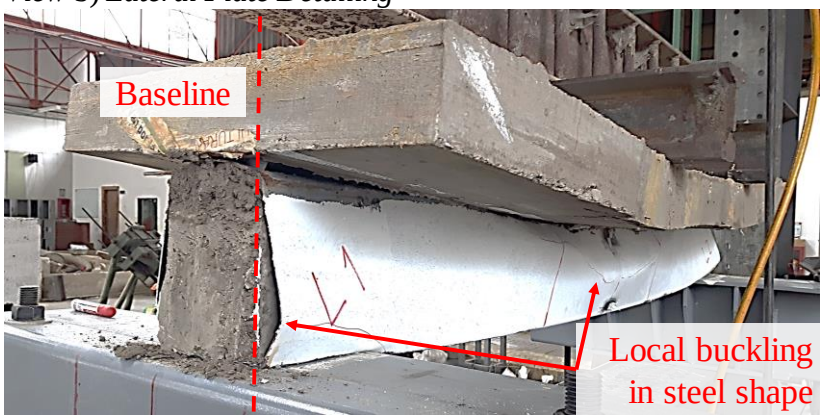

a)

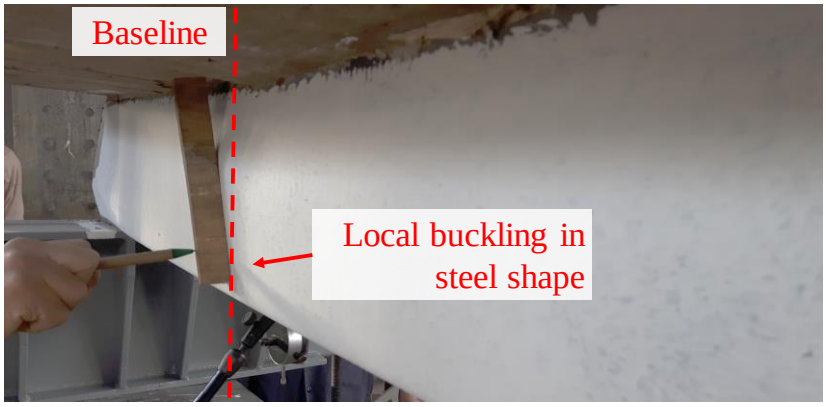

b)

Source: Authors.

Additionally, strains were recorded through strain gauges installed on vertical steel plates, located at 20 mm from each upper and lower border (Figure 11). The initial and final results are included in Figure 22, where the intersection with the Y-axis indicates the location of the neutral axis (marked as horizontal dotted lines), equivalent to zero strain. According to results, downward displacement of the neutral axis is perceived, through increases in load, predominantly in 4 m-long beams. Therefore, the performance of the composite system was progressively reduced, transferring work only to steel capacity, obtaining independent action of materials at the final state.

Figure 22. *Strain State in Composite Section Beams*

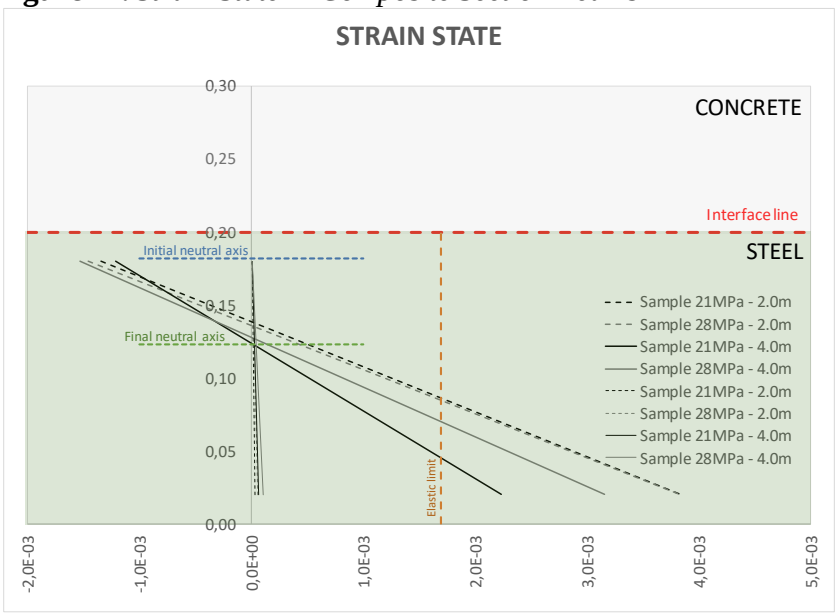

Source: Authors.

Once the experimental tests were completed, the concrete slab was removed, to know the final state of the shear connectors fastening system after working as elements of stress transference between materials (Figures 23 and 24).

Figure 23. *Final State of Self-Drilling Screws Fastening System*

Source: Authors.

Figure 24. *CFS Shapes Separation in the Assembled Box Section*

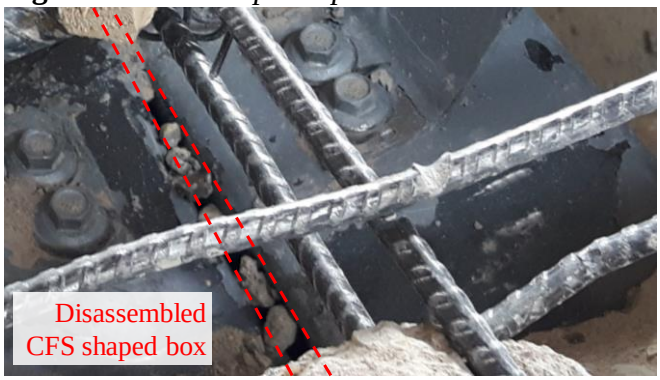

Source: Authors.

According to Figures 23 and 24, the self-drilling screw system kept integrity by itself. Shear connectors remained attached to the CFS shape, without evidence of damages by tearing in the area of the perforations, nor by shearing in screws. System deformation was governed mainly by local buckling in the steel section and, to a lesser extent, by cracking in the slab concrete. Thus, the CFS shape becomes the restrictive element in the capacity of the composite systems.

Likewise, the intermittently welded CFS shape box was disassembled, due to high displacements and deformations of the cross-section (Figure 24).

Based on the results evidenced in this study, it can be concluded that the self-drilling screws fastening mechanism of shear connectors provide a stable joint. It is capable to develop a high capacity of stress transfer in the interface between materials, allowing large deflections in the composite section, without local damages or detachment of the system.

Conclusions

In this research, the self-drilling screws were characterized as an alternative fastening mechanism. Its mechanical capacity during the transfer of stresses to composite systems was validated through experimental tests. Results prove them to be an alternative to welding, mainly in the CFS shapes.

The mechanism allowed composite sections to develop an inelastic capacity before presenting damages caused by local buckling in the CFS sections, without

becoming the weakest element of the system. In addition, recorded deflections exceeded the service limits widely without evidence of screws detachment and showing high ductility.

The ultimate capacities in the full-scale beam test were within the nominal range (elastic-plastic), approaching the plastic behavior in 95% and 74% in 4 m-long beams and 2 m-long beams, respectively. This allows establishing predictions of analytical capacity in both cases, which exceeded elastic capacity as suggested in design codes such as AISC 360 and Eurocode4, which are the main international references.

According to the experimental results of screw shear tests, the failure modes presented an adequate correlation compared to the design formulation loads, mainly in the failure of 2.0 mm thickness plates. In thinner plates, the nominal capacity load exceeded the experimental data.

Plates of more than 2.0 mm thickness presented failure mechanism caused by shear screws. In contrast, plates with lower thickness failed due to bearing plates or tension on the net section in the thinnest plate but showing greater ductility.

The CFS samples are particularly susceptible to be affected in their mechanical properties during the experimental tests, due to the limited thickness. Therefore, procedures must be highly controlled to avoid alterations in the data record.

The self-drilling system has a better structural performance as a fastening mechanism than the powder-actuated fastening system, due to its high mechanical strength and ease to be implemented in construction.

Acknowledgements

The authors thank the management and financial support of the Research and Extension Office of the Faculty of Engineering of Universidad Nacional de Colombia, for the project "Comportamiento de secciones compuestas acero-concreto con conectores de cortante tipo tornillo a partir de experimentación y simulación numérica" in the framework of the National Call for Strengthening, Creation and Innovation of the University 2016-2018.

References

Alhajri T, Tahir M, Azimi M, Mirza J, Lawan M, Alenezi K et al. (2016) Behavior of pre-cast u-shaped composite beam integrating cold-formed steel with ferro-cement slab. *Thin-Walled Structures* 102(May): 18-29.

American Institute of Steel Construction - AISC (2016) *Specification for structural steel buildings (AISC 360-16)*. USA.

American Iron and Steel Institute - AISI (2016) *North American specification for the design of cold-formed steel structural members (S-100)*. USA.

Associacao Brasileira de Normas Tecnicas - ABNT (2008) *Norma brasileira ABNT NBR 8800*. (Brazilian standard ABNT NBR 8800) Brazil.

Australian/New Zeland Standards - AS/NZ (2005) *Cold formed steel structures (AS/NZ 4600:2005)*. Australia.

Canadian Standards Association - CSA (2007) *North American specification for the design of cold formed steel structural members (S136-07)*. Canada.

Derlatka A, Lacki P, Nawrot J, Winoviecka J (2019) Numerical and experimental test of steel concrete composite beam with the connector made of top-hat profile. *Composite Structures* 211(Mar): 244-253.

Erazo L, Molina M (2017) *Comportamiento de conectores de cortante tipo tornillo en secciones compuestas con lámina colaborante*. (Behavior of screw type shear connectors in composite sections with collaborating sheet). Master Thesis. Colombia: Civil Engineering - E-structures, Universidad Nacional de Colombia.

European Committee Standardization - ECS (2004) *Eurocode 4: design of composite steel and concrete structures*.

Fontana M, Bärtschi R (2002) *New types of shear connectors with powder-actuated fasteners*. Zurich: ETH Zürich Research Collection. Institute of Structural Engineering - Swiss Federal Institute of Technology.

Hanaor A (2000) Tests of composite beams with cold-formed sections. *Journal of Constructional Steel Research* 54(2): 245-264.

Hancock G (2003) Cold-formed steel structures. *Journal of Constructional Steel Research* 59(4): 473-487.

Hossain A (2005) Designing thin-walled composite-filled beams. *Proceedings of the Institution of Civil Engineers. Structures & Buildings* 158(4): 267-278.

Irvwan J, Hanizah A (2009) Test of shear transfer enhancement in symmetric cold-formed steel concrete composite beams. *Journal of Constructional Steel Research* 65(12): 2087-2098.

Japan Society of Civil Engineers - JSCE (2007) *Standard specifications for steel and composite structures*. Japan.

Kyvelou P, Gardner L, Nethercot D (2017) Design of composite cold-formed steel flooring systems. *Structures* 12(Nov): 242-252.

Kyvelou P, Gardner L, Nethercot D (2018) Finite element modelling of composite cold-formed steel flooring systems. *Engineering Structures* 158(Mar): 28-42.

Lakkavalli B, Liu Y (2006) Experimental study of composite cold-formed steel c-section floor joist. *Journal of Constructional Steel Research* 62(10): 995-1006.

Lawan M, Tahir M, Ngian S, Sulaiman A (2015) Structural performance of cold-formed steel section in composite structures: A review. *Jurnal Teknologi* 74(4): 65-175.

Lawan M, Tahir M (2015) Strength capacity of bolted shear connectors with cold-formed steel section integrated as composite beam in self-compacting concrete. *Jurnal Teknologi* 77(16): 105-112.

Lawan M, Tahir M, Osman H (2015) Composite construction of cold-formed steel (CFS) section with high strength bolted shear connector. *Jurnal Teknologi* 77(16): 171-179.

Lawson R, Popo-Ola S, Varley D (2001) Innovative development of light steel composites in buildings. In *International Union of Laboratories and Experts in Construction Materials and Structures (RILEM). International Symposium on Connections between Steel and Concrete*.

Merryfield G, El-Ragaby A, Ghrib F (2016) New shear connector for open web steel joist with metal deck and concrete slab floor system. *Construction and Building Materials* 125(Oct): 1-11.

Queiroz G, Rodrigues F, Pereira S, Pfeil M, Oliveira C, Da Mata L (2010) Behavior of steel concrete beams with flexible shear connectors. In *International Colloquium on Stability and Ductility of Steel Structures* 2006. Volume 1: 863-870.

Tahir M, Saggaff A, Azimi M, Lawan M (2016a) Impact of bolted shear connector spacing in composite beam incorporating cold formed steel of channel lipped section. *IIOAB Journal* 7: 441-445.

Tahir M, Saggaff A, Azimi M, Lawan M (2016b) Influence of bolted shear connector size in push-out test for composite construction with cold formed steel section. *IIOAB Journal* 7: 521-526.

Valencia G (2010) *Diseño básico de estructuras de acero de acuerdo con NSR-10*. (Basic design of steel structures in accordance with NSR-10). 1st Edition. Bogotá, Colombia: Editorial Escuela Colombiana de Ingeniería.

Yu WW, LaBooube R (2010) *Cold formed steel design*. 4th Edition. New Jersey, USA: John Wiley & Sons Inc.